DETECTION OF ABNORMALITIES USING FUSION OF BRAIN CT AND MR IMAGES

A THESIS

Submitted in fulfillment of the requirements for the award of the degree of

Doctor of Philosophy

in

Electrical and Instrumentation Engineering

Submitted by

Sharma Dileepkumar Ramlal

Registration No: 951404005

Under the supervision of

Dr. Jainy Sachdeva

Associate Professor

Department of Electrical and Instrumentation Engineering

Thapar Institute of Engineering and Technology, Patiala

and

Dr. Chirag Kamal Ahuja

Associate Professor

Department of Radio-diagnosis and Imaging, PGIMER, Chandigarh

THAPAR INSTITUTE
OF ENGINEERING & TECHNOLOGY
(Deemed to be University)

Department of Electrical and Instrumentation Engineering

Thapar Institute of Engineering and Technology, Patiala, India-147004

January, 2021

CERTIFICATE

I hereby certify that the work presented in this thesis report entitled **"DETECTION OF ABNORMALITIES USING FUSION OF BRAIN CT AND MR IMAGES"** in fulfilment of the requirements for the award of the degree of Doctor of Philosophy and submitted in the Electrical and Instrumentation Engineering Department of the Thapar Institute of Engineering & Technology, Patiala, is an authentic record of my own research work carried out during a period from January 2015 to February 2020 under the supervision of Dr. Jainy Sachdeva, Associate Professor, Electrical and Instrumentation Engineering Department of Thapar Institute of Engineering & Technology, Patiala, India and Dr. Chirag Kamal Ahuja, Associate Professor, Department of Radio-diagnosis and Imaging, Postgraduate Institute of Medical Education and Research, Chandigarh, India.

The matter presented in this thesis has not been submitted by me for the award of any other degree of this or any other institute.

(SHARMA DILEEPKUMAR RAMLAL)
Registration No.951404005

This is to certify that the above statement made by the candidate is correct to the best of my knowledge and belief.

(Dr.Chirag Kamal Ahuja)
Supervisor

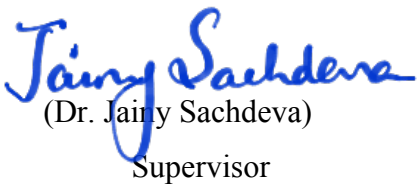

(Dr. Jainy Sachdeva)
Supervisor

ACKNOWLEDGEMENT

I express my gratitude to my supervisors Dr. Jainy Sachdeva, Department of Electrical and Instrumentation Engineering, Thapar Institute of Engineering and Technology, Patiala and Dr. Chirag Kamal Ahuja, Department of Radio-diagnosis and Imaging, Postgraduate Institute of Medical Education and Research, Chandigarh, India for their deep motivation, guidance and suggestions for the completion of this research. I shall ever remain indebted to them for their meticulous guidance, clear thinking, constant encouragement, moral support, and forbearance right from the beginning of the research to its completion. I am highly obliged to them for being there always whenever I needed them.

I express my sincere thanks to the members of my research committee Dr. Deepti Mittal, Associate Professor, Department of Electrical and Instrumentation Engineering, Dr. M.D. Singh, Associate Professor, Department of Electrical and Instrumentation Engineering, Thapar Institute of Engineering and Technology, Patiala and Dr. R. K. Sharma, Professor, Department of Computer Science and Engineering, Thapar Institute of Engineering and Technology, Patiala for their encouragement and support during my tenure of work.

I am thankful to the Chairman of the Doctoral Committee Dr. R.S. Kaler, Senior Professor and Head, Department of Electrical and Instrumentation Engineering for his support throughout the work. I am also thankful to Dr. Nisha Thakur, Dr. A.N. Yadav and Mr. S.L. Tripathi for their help and support. I also extend my thanks to all those whom I have missed mentioning. It is their blessings that helped me to reach this end.

I wish to acknowledge most sincerely Dr. N. Khandelwal, former Professor and Head Postgraduate Institute of Medical Education and Research, Chandigarh, for showing his keen interest and support in this research.

Above all, I would like to dedicate this work to my parents, kids, Anay and Ahan, my wife, my sister and brother in law who missed my presence and support to them during this work. In the end, I am thankful and grateful to the Almighty for bringing this day in my life.

Patiala

Sharma Dileepkumar Ramlal

The rapid technological development in instrumentation has resulted in many medical imaging techniques to capture and represent the visual information of different parts of the human body. The imaging modalities such as magnetic resonance imaging (MRI) and computed tomography (CT) represent structural details of tissues or organs. The radiologists often advise multimodal imaging to identify the diseased tissues of a particular organ as many a time a single modality is insufficient in conveying the complete information of a tissue or organ. The multimodal imaging may consist of a CT image which represents bone information precisely and MRI image which provides clear soft-tissue information. The intensity and texture information of different tissues represented by CT and MRI are fused to visualize hard and soft tissues clearly in a single image. The details of abnormalities such as edges and textures can be accurately demarcated from the surrounding tissues by the fusion image. The fused images can be clustered for the detection of abnormalities. The fusion can enhance the clustering results and classification accuracy. The existing fusion schemes fail to meet the real-time requirements of the radiologists such as the computational speed of the algorithm, contrast, clarity and edge information of the fused image. Hence, there is a need to develop new fusion methods that can meet the real-time requirements of the radiologists. Based on the above research gaps in this field, research objectives have been defined. The main aims are to design and develop faster fusion algorithms with better contrast, clarity, brightness and edges which can help in the detection of abnormalities. To achieve the goals multi-resolution transforms based fusion methods with different fusion rules are developed and clustering schemes are applied for the detection of abnormalities in the fusion images.

In order to validate the proposed methods image pairs are acquired from various sources. The real-time dataset consisting of 40 image pairs of five patients suffering from various diseases are acquired from Postgraduate Institute of Medical Education and Research (PGIMER), Chandigarh, India. Another standard dataset consisting of ten image pairs of ten patients suffering from different brain diseases are acquired from internet repositories. To evaluate the performance of the proposed fusion and clustering methods qualitative analysis is done by the author as well as by the expert radiologists to know their clinical application. To validate the visual results quantitative analysis is also done using fusion and clustering quality assessment parameters.

Three different fusion schemes are developed which are based on non-subsampled contourlet transform (NSCT), stationary wavelet transform (SWT) and non-subsampled shearlet transform (NSST). These three different techniques provide sufficient coverage of the applicability of the multi-resolution transformation domain in image fusion.

The first scheme is an NSST based scheme in which a novel fusion rule is proposed. It is based on the morphological gradient motivated pulse-coupled neural network. The scheme is found to be faster and better in terms of contrast, clarity, brightness and edge information as compared to state of the art schemes. The second developed scheme is a hybrid multi-resolution scheme which is a combination of NSCT and SWT. The SWT is used in the form of a novel LF sub-band fusion rule. This scheme carries better texture, contrast, clarity and edges in the fused image as compared to state-of-the-art NSST based fusion methods. The third scheme is also based on NSST and a novel fusion rule. This fusion rule is based on a human visual system motivated operator called the smallest uni-value segment assimilating nucleus. This scheme is also found to be a faster option when compared to state of the art schemes while preserving the structural details of CT and MR images. These schemes serve as an automatic tool to the radiologists while obtaining the diagnostic information during skull injury, to mark the disease orientation as regards to bone and also to decide the point and depth of insertion of surgical instruments during brain surgery. All these schemes are useful for the clinical applications according to the radiologists. The fourth scheme is a clustering scheme that segments the tissues of fusion images into different classes. Four different clustering schemes are applied to segment the fusion images in this method. The clustered fusion images are visually and quantitatively compared for the detection of diseases. A visual analysis of clustered fusion images is also done along with the clustered MR images to compare the information gained in the clustered fusion images. It is observed that the clustered fusion images show the edema and tumor as two separate classes whereas, clustered MR images show these tissues as a single class. The clustered fusion images show the intensity inhomogeneous regions of the same tissues as a single class whereas, the clustered MR images show these as separate classes. This proves that the fusion information aids in clustering for the detection and separation of abnormalities. The developed methods help the radiologists in precise localization, diagnosis, interpretation and treatment planning of brain diseases.

ADC	Apparent diffusion coefficient
ANN	Artificial neural network
ARKFCM	Adaptively regularized kernal based fuzzy c means
ASR	Adaptive sparse representation
BVF	Boundary vector flow
CC	Correlation coefficient
CF	Column frequency
CNT	Contourlet transform
C_p	Partition coefficient
CP	Contrast pyramid
CSF	Cerebrospinal fluid
CSR	Convolutional sparse representation
CT	Computed tomography
CVT	Curvelet transform
DFB	Directional filter bank
DTCWT	Dual tree complex wavelet transform
DWI	Diffusion weighted imaging
DWT	Discrete wavelet transform
EM	Expectation maximization
ENT	Entropy
FCC	Filtered correlation coefficient
FCM	Fuzzy C-means
FFT	Fast Fourier transform
FLAIR	Fluid attenuation inversion recovery

FLIR	Forward looking infrared
FT	Framelet transform
FVF	Fluid Vector Flow
GA	Genetic algorithm
GM	Gray matter
GP	Gradient pyramid
GVF	Gradient vector flow
HF	High-frequency
HPF	High pass filter
HSV	Hue, saturation and value
HVS	Human visual system
ICA	Iterative component analysis
ICM	Iterated conditional modes
IHS	Intensity, hue, saturation
IQI	Image quality index
JND	Just-noticeable difference
KL	Karhunen-Loeve
LF	Low-frequency
LLTV	Low light television
LP	Laplacian pyramid
LPF	Low pass filter
MAC	Magnetostatic active contour
MI	Mutual information
MIDT	Multiscale image decomposition transform
ML	Modified Laplacian
MRA	Magnetic resonance angiography

MRFCM	Morphological reconstruction based fuzzy c means
MRI	Magnetic resonance imaging
MSD	Multi-scale decomposition
NMI	Normalized mutual information
NSCT	Nonsubsampled contourlet transform
NSDFB	Non-subsampled directional filter banks
NSLP	Non-subsampled Laplacian pyramid
NSPFB	Non-subsampled pyramid filter banks
NSST	Nonsubsampled shearlet transform
OCE	Overall cross entropy
PCA	Principal component analysis
PCNN	Pulse coupled neural network
PD	Proton density
PET	Positron emission tomography
PGIMER	Postgraduate Institute of Medical Education and Research
PSNR	Peak signal to noise ratio
$Q^{AB/F}$	Edge information based quality metric
Q_W	Piella's structure similarity metric
RF	Row frequency
RMSE	Root mean square error
ROI	Region of interest
ROIs	Regions of interest
SD	Standard deviation
SF	Spatial frequency
ShF	Shearing filters
SPECT	Single photon emission computed tomography

SPSS	Statistical package for social sciences
SR	Sparse representation
SSIM	Structural similarity
ST	Shearlet transform
SUSAN	Smallest uni-value segment assimilating nucleus
SVM	Support vector machine
SWI	Susceptibility weighted imaging
SWT	Stationary wavelet transform
UIQI	Universal image quality index
USAN	Uni-value segment assimilating nucleus
WM	White matter
WSML	Weighted sum modified Laplacian

LIST OF TABLES

CHAPTER 1

INTRODUCTION

1.1 OVERVIEW

Medical imaging is defined as the technique of visual representation of human body parts. Medical imaging is done with the help of scanning modalities which are categorized broadly into functional and anatomical modalities. Functional modalities like positron emission tomography (PET) or single-photon emission computed tomography (SPECT) give physiologic information of organs or tissues such as oxygen utilization, blood volume and so on [1]. The anatomical modalities such as computed tomography (CT) and magnetic resonance imaging (MRI) represent the physical structure of tissues and organs of the human body [2-4]. CT imaging is done by passing X-ray beams through the patient body at different angles. Detectors on the exit side of the X-ray source record the beams that have passed through the patient body. Different tissues of the body absorb X rays by a different amount which results in different contrast of the tissues in an image. Dense tissues such as bone absorb a large number of X rays and hence they appear white on a CT image. Soft tissues appear in different shades of gray and air appears in black. Figure 1.1(a) shows a sample brain CT image. The contrast of different tissues of the CT image is given in Table 1.1. Figure 1.1(b) shows the hard and soft tissue information on the MRI image. In magnetic resonance imaging, the magnetic field is applied to the patient which aligns the spin of hydrogen atoms (protons) parallel to the direction of the field [5, 6]. The hydrogen atoms present in the body oscillate at a frequency proportional to the frequency of the applied magnetic field. When a radio frequency pulse resonating at the frequency of the external magnetic field is applied, the hydrogen atoms gain energy and tilt (transversely magnetized). As the radio pulse is removed, the excited atoms return to the equilibrium state. This is known as relaxation. In this process, these protons release the energy in the form of a radio frequency signal. This signal is measured by a receiving coil which is used to construct the image. The return of protons to the equilibrium state is not instantaneous but it takes a certain time and depends upon longitudinal relaxation (T1) and transverse relaxation (T2). The longitudinal relaxation process realigns the protons parallel to the main magnetic field. Transverse relaxation represents the decay of transversal magnetization with time. Different tissues possess different proton density (PD), T1 and T2 times and hence, have different contrast.

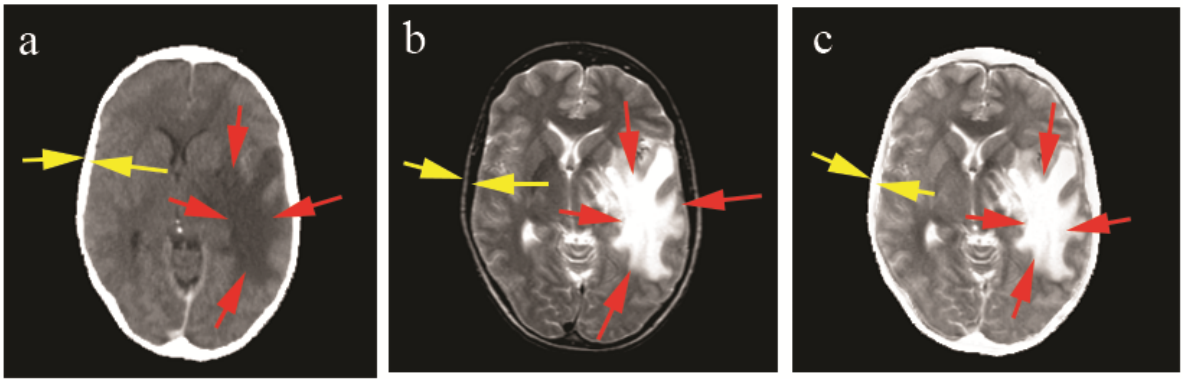

Figure 1.1 Brain CT, MR and fused image

(a) CT image- High-intensity bone information marked with yellow arrows, low intensity and texture tissue information marked by red arrows. The edema in the brain parenchyma is seen to reach uptil the brain surface close to the bone.
(b) MR image- Low-intensity bone information marked with yellow arrows, high-intensity texture tissue information marked by red arrows.
(c) Fused image- High-intensity bone and texture tissue information marked by yellow and red arrows, respectively. The regions highlighted in red arrows show better delineation of bone and brain parenchyma. The edema which on CT is seen to extend in the bone is actually limited by the cortex of the brain parenchyma on the fused image.

Table 1.1 Tissue Contrast of the CT Image

Tissue type	CT image contrast
Bone	Bright
Cerebrospinal fluid (CSF)	Dark
White matter	Dark grey
Grey matter	Light grey
Air	Dark
Water	Dark
Tumor	Dark
Calcification	Bright

The received signal can be made dependant on PD, T1 or T2 relaxation time by varying the radio frequency pulse duration, repetition rate, timing and amplitude. This provides a PD image, T1 weighted (T1-W) image or T2 weighted (T2-W) image which shows different contrast of different tissues. A sample T1-W and T2-W MR image are shown in Figure 1.2(a) and Figure 1.2(b), respectively. The tissue contrast of T1-W and T2-W MRI images is given in Table 1.2. CT images are rich in bone and calcification however, lack in soft tissue

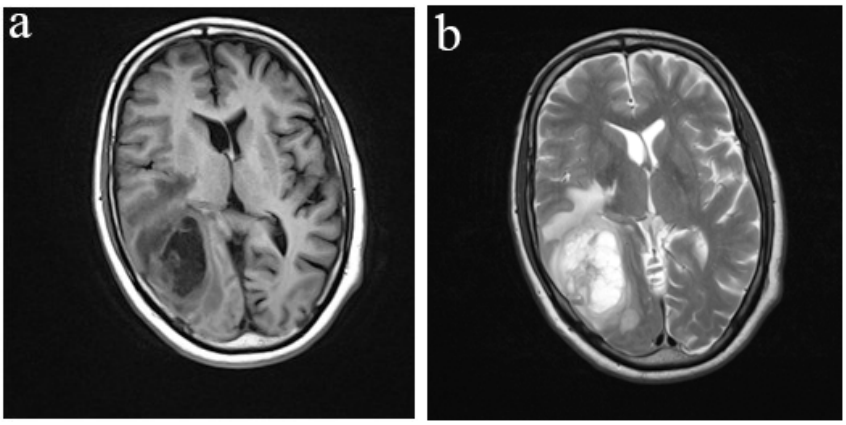

Figure 1.2 Brain MRI images

(a) T1-W MR image
(b) T2-W MR image

Table 1.2 Tissue Contrast of T1-W and T2-W MRI Images

Tissue type	T1-W MRI intensity	T2-W MRI intensity
Bone	Dark	Dark
CSF	Dark	Bright
White matter	Light	Dark gray
Air	Dark	Dark
Water	Dark	Bright
Tumor	Dark	Bright
Calcification	Dark	Dark
Cortex	Gray	Light gray
Inflammation	Dark	Bright

details whereas MR images are rich in soft tissues and poor in hard tissue details. CT and MR images can be combined to get hard tissue and soft tissue information in a single image. The process by which these two images are combined is called image fusion [7]. The aim is to obtain more information than that can be derived from individual images [8, 9]. CT and MR image fusion provides the exact location and orientation of tissues or lesions w.r.t. bone in the brain. Lesion (abnormal changes in tissues/ pathology) description for radiation therapy planning improves with fusion [10, 11]. The desired region of interest (ROI) i.e. organ's segmentation and classification accuracy increase with fusion. It improves the visual quality of the image by reducing the intensity inhomogeneity of the MR image caused by the magnetic field. It helps in choosing the site of biopsy and provides the minimum incision distance to the tumor. Fusion serves as a wonderful medium for teaching graduate and postgraduate students regarding brain anatomy. A fused image is shown in Figure

1.1(c) in which the high-intensity soft-tissue information and bone information is marked by the red arrows. The following section gives a detailed description of the image fusion process.

1.2 FRAMEWORK OF THE FUSION PROCESS

The fusion process is classified into pixel level, feature level and decision level [12-14]. In pixel-level fusion; the fused image is formed by a set of pixels in the input images [15, 16]. This method is computationally more efficient, easy to implement and contains directly measured quantities. Feature level fusion segments the source images into regions and features such as intensities, textures or edges are employed in the fusion process [17, 18].

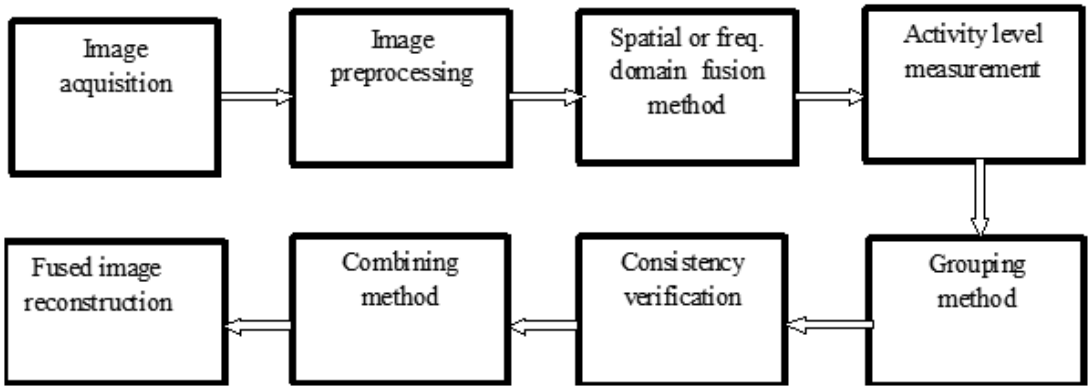

Figure 1.3 Block diagram of the pixel-level image fusion process

Decision level fusion is done with the help of statistics, prediction, fuzzy sets, minority voting, classifiers and heuristics, etc. [19]. Pixel level fusion methods are less complex whereas, feature and decision level fusion methods are more complex and are generally employed by the researchers in segmentation and classification problems. Figure 1.3 shows the block diagram of the pixel-level image fusion scheme. Pixel level fusion schemes involve various steps such as Image pre-processing, spatial or frequency domain image decomposition, activity level measurement, coefficient grouping, combining methods and consistency verification which are explained as follows:

1.2.1 Image Pre-Processing

Due to the two different modalities used in the acquisition of images, the patient posture and resolution of two images may vary [20, 21]. This results in the misalignment of two images during the fusion process. Therefore, image registration is an essential pre-processing requirement before image fusion. Registration of multimodal images minimizes or even eliminates the aforementioned drawbacks and improves fusion quality. Image registration

aligns CT and MR images into a common coordinate system so that the information from the same physical structures is fused together [22, 23]. A pixel by pixel or feature by feature comparison of the two images is done to correct any translational, rotational or magnification differences. Image registration techniques are grouped into two types as intensity-based and feature-based registration [23]. Intensity-based registration uses the correlation metrics to compare intensity patterns in the images [24]. Feature-based algorithms find characteristics such as points, lines, and curves in the images. These features are compared in the two multimodal images to be registered.

The registration algorithms contain three main components named spatial transformation, similarity measure and optimization algorithm. The types of spatial transformations are categorized as affine and nonaffine. Affine transformations are further categorized as rigid and nonrigid. Rigid transformations contain only translation and rotation but no scaling. Nonaffine transformation describes local deformations. It is categorized into three types as mesh-based, uniform grid-based and direct mapping. The similarity measure finds the similarities between the two images to be registered [25]. Examples of similarity measures are mutual information (MI), correlation coefficient (CC), etc [26-28]. The optimization algorithm searches for the optimization of the similarity measure. The various optimization algorithms are gradient descent, quasi-Newton and Powell's method [29, 30]. The images to be registered are called a source or reference image and the target image. Figure 1.4(a) shows a reference image. Figure 1.4(b) and Figure 1.4(c) shows an unregistered and registered target image, respectively. The image with better resolution or contrast is generally selected as a reference image.

1.2.2 Spatial Domain or Frequency Domain Transform Decomposition Methods

Pixel level fusion methods are classified into spatial domain and transform domain methods [31]. Spatial and frequency transform decomposition methods are employed after image preprocessing to obtain important information from the source images in the fusion. In spatial domain methods, source images are fused directly without converting them into the frequency domain. Brovey transform, principal component analysis, linear discriminant analysis are some examples of spatial domain fusion methods [2, 32]. These methods use simple arithmetic operations like addition, multiplication or division of the pixels in source images. The best method to perform image fusion is the multiscale decomposition transformation (MSD) which splits an image into different scales and frequency subband images. Hence fusion can be performed at different scales and orientations, independently. MSD provides a good mathematical model of the human visual system and details of

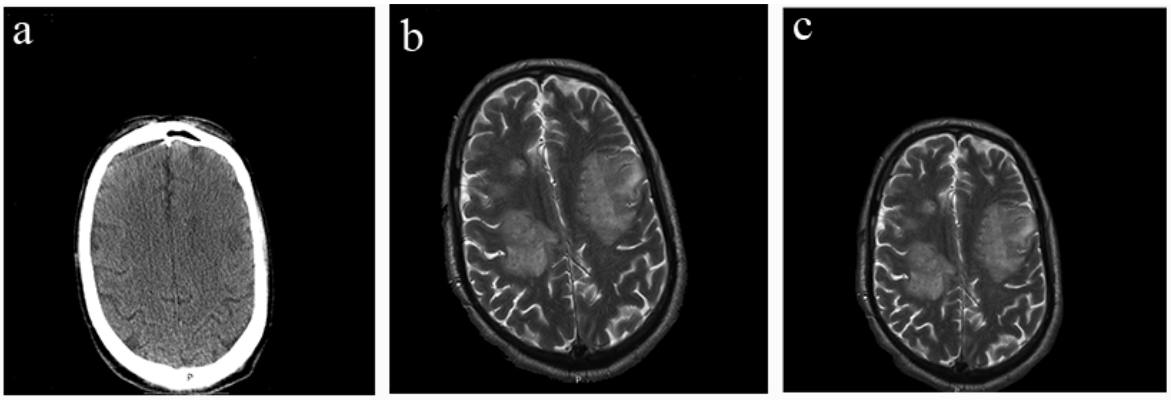

Figure 1.4 Registration of multimodal image

(a) Reference image
(b) Target image before registration
(c) Target image after registration

contrast variations [10]. There are various multi-scale transforms which can be employed for fusion such as discrete wavelet transform (DWT) [33], curvelet transform (CVT) [34], nonsubsampled contourlet transform (NSCT) [35], framelet transform (FT) [36] and nonsubsampled shearlet transform (NSST) [37].

Multiscale transforms as mentioned above split the image into low-frequency (LF) and high-frequency (HF) sub-bands at different scales and directions. A brief description of a few important multi-scale transforms is given below.

1.2.2.1 Discrete wavelet transform

The discrete wavelet transform (DWT) is constructed using a set of low pass and high pass filter banks. The output of the low pass filter is decomposed further into low frequency and high-frequency bands. The coefficients of DWT are called approximation and detail coefficients. This transform can resolve point singularities properly. However, It has a disadvantage of poor directional selectivity and thus it can not work with curved lines efficiently.

1.2.2.2 Curvelet transform

The curvelet transform (CVT) segments the image into small overlapping tiles to avoid edge effects. Segmentation is done to approximate curved lines by small straight lines. This transform gives better curve information, therefore fine fusion results are obtained than wavelet transform.

1.2.2.3 Contourlet transform

The contourlet transform (CNT) has two main building blocks: the Laplacian pyramid (LP) and the directional filter bank (DFB). The Laplacian pyramid captures point singularities that are linked into linear structures by directional filter banks. LP decomposes the image

into low and high-frequency images. The high-frequency subbands are converted into directional subbands by DFB.

1.2.2.4 Nonsubsampled contourlet transform

The nonsubsampled contourlet transform **(**NSCT) is proposed by [35]. It inherits the advantages of CNT and overcomes its shortcomings like pseudo-Gibbs phenomena. The NSCT improves directional selectivity and shift variance of CNT. It has two building blocks as non-subsampled pyramid filter banks (NSPFB) and non-subsampled directional filter banks (NSDFB). Non-subsampled pyramid filter banks ensure the multiscale performance of NSCT. The directional fan filters are added, downsamplers and upsamplers are eliminated from DFB to construct NSDFB. It provides NSCT multidirectional performance. NSCT based fusion reduces the effect of misregistration on the fused image.

1.2.2.5 Framelet transform

The framelet transform (FT) is similar to wavelet transform with some important differences. It has one scaling function and two wavelet functions whereas, there is only one scaling and one wavelet function in DWT [38]. Framelet transform is used in fusion as it removes limitations of wavelet and related transforms to a larger extent. This transform is nearly shift-invariant. It has negligible aliasing to the reconstructed image. It has lesser blocking artifacts and has perfect reconstruction conditions.

1.2.2.6 Nonsubsampled shearlet transform

The nonsubsampled shearlet transform (NSST) is formed by combining the non-subsampled Laplacian pyramids with different shearing filters in several numbers. It has less computational complexity as compared to NSCT. Its applications in medical image fusion are not broadly explored yet [39].

Multiscale transforms as mentioned above split the image into different frequency subbands. The important factor which affects the quality of fusion is the fusion rule. It is used to select and merge coefficients of different subbands to form the fused image [40]. Widely used fusion rule is the maximum selection rule which selects the largest absolute coefficient at each location from source images into the fused image [41]. There are some alternative procedures for fusion rules. These are activity level measurement, coefficient grouping, consistency verification and combining the coefficients.

1.2.3 Activity Level Measurement

The activity level of a multiscale transform coefficient represents the local energy belonging to that coefficient. It indicates the importance of a particular coefficient in fusion. The activity measure of a coefficient can be computed in three different ways. It is called a

coefficient based, window-based or region-based activity measure [42]. The coefficient based method considers each coefficient separately and its activity level is represented by the absolute value or square of the coefficient value. In windows based activity, a small window of size says 3×3 is placed at the center of the coefficient whose activity level is to be measured. A few examples of window-based activity measures are weighted average, spatial frequency (SF) method, the sum of local variations, gradient-based activity, visibility, local weighted energy, variance, mean and edge [3, 38, 40, 43, 44]. These represent texture associated with the current coefficient. Region-based activity is the same as a windows-based activity with odd shapes.

1.2.4 Grouping Method

After computing the suitable activity measure the next step is to group the coefficients of multiscale decomposition transform so that more information of source images can be fetched into the fusion image. Grouping can extract better features information from different subband images at different scales in the fused image. It requires a statistical model such as the hidden Markov tree to identify the relationships between subbands. A weight factor and the probability distribution function are computed which are applied to fuse the pixels in the fusion process. However, it increases the complexity and achievement of the desired results is uncertain. The various options under grouping are no grouping, single scale grouping and multi-scale grouping [40]. No grouping means there is no association or dependency between coefficients of different sub-bands and scales. Only a separate coefficient or a few neighbors of the present coefficient of a particular frequency sub-band is considered. Important dependent information that exists in the coefficients of the different subbands and the cross-scale is lost in this scheme. Most of the existing fusion schemes belong to this category. In single scale grouping, the respective coefficients of all the frequency sub-bands at a specific scale are used to provide a fusion decision. In multi-scale grouping, a specific coefficient at a frequency subband of a scale is associated with the corresponding coefficient of other subbands and other scales to make a fusion decision. This is the most restrictive case of coefficient grouping [168]. The multi-scale grouping schemes are particularly advantageous with some models such as Markov random fields.

1.2.5 Consistency Verification

This step can be performed after performing the activity level measurement and grouping. The choices under it are no verification and consistency verification. No verification means this step is not performed in the fusion process. Consistency verification is done to ensure that if the majority of coefficients in a window are from image A and the central coefficient

is from image B then the central pixel is also derived from image A. It reduces the effect of noise and makes the fused image more homogeneous [45]. Consistency verification can be implemented using a window-based majority filter or using morphological opening and closing operations.

1.2.6 Combining Method

This is the last step in the fusion process. After finding the activity levels of coefficients of each image, these can be utilized to find the relationship between coefficients at other scales and subbands using statistical models. This step is performed to extract better features of information from source images in the fused image. Thereafter, performing consistency verification, the coefficients can be combined using averaging of the corresponding coefficients from two images or these can be selected from either of the source images. Under selection, there are many possibilities like selecting coefficients with the maximum absolute value of the activity, fusing by energy comparison, background elimination and variance area-based scheme.

1.2.7 Fused Image Reconstruction

In multiscale frequency transformation fusion schemes, all the steps except the preprocessing are implemented in the frequency domain. In order to visualize the image by the human eye, the fused image is converted to the spatial domain. This is done by applying the inverse transformation of the fused image.

1.3 SEGMENTATION SCHEMES

The fusion is followed by segmentation and vice versa. Segmentation is defined as to subdivide an image into its constituent parts in order to extract information regarding region of interest (ROI) [46, 47]. In segmentation, ROIs such as gray matter (GM), white matter (WM), brain tumors, or CSF (generally known as edema when associated with the tumor) are segregated. The fusion followed by segmentation or vice versa allows surgical and treatment planning of the segmented ROI. Moreover, the complementary information such as bone, calcification or distance between the ROI and bones is obtained in a single fused image. Segmentation of a raw image into ROI such as GM, WM and CSF is shown in Figure 1.5. Brain tumor as ROI is shown in Figure 1.6.

Segmentation is done manually, semi-automatically or automatically. Manual segmentation is performed by an expert by locating the tumor on all adjoining slices on which the tumor is considered to exist. However, it is a time-consuming process and manual segmentation varies among different experts. Moreover, the same expert may perform different segmentation of the same image on different occasions [48-50]. On the other hand, semi-

automatic methods consist of interactive identification of seed points or regions and extraction of the organ boundary from the selected seed points or regions. Parametric active

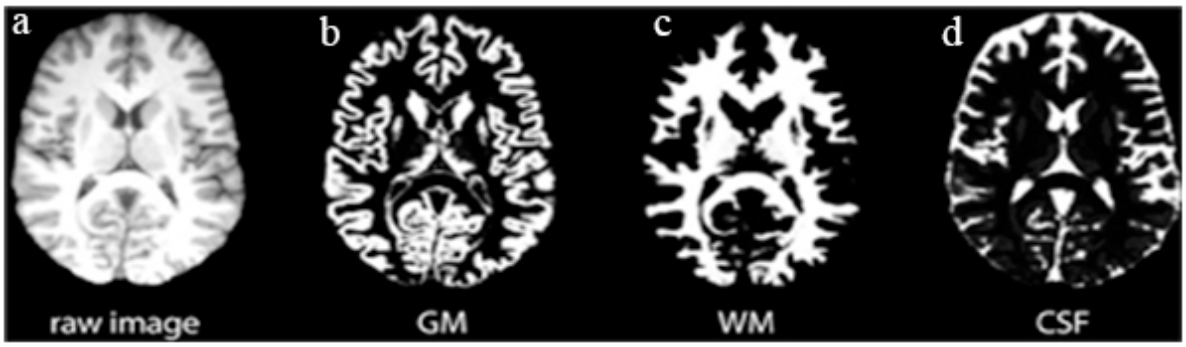

Figure 1.5 Segmentation of MRI image

(a) Raw MR image
(b) Segmentation of GM
(c) Segmentation of WM
(d) Segmentation of CSF

contour models are semi-automatic methods. However, these methods require manual labeling of the ROI [51]. Non-tumor brain structures such as blood vessels and soft tissues are often misidentified as tumors by manual labeling leading to many false positives [50]. Hence a major challenge is to reduce user intervention without compromising the segmentation result [48].

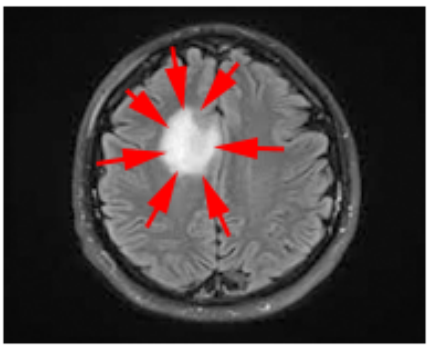

Figure 1.6 Brain tumor on MR image

(Tumor region marked with red arrows)

Automatic segmentation algorithms recognize the boundary of the organ or tissues using a morphological processing scheme or histogram analysis. Several automatic schemes exist for identification and segmentation of brain tumors such as k-means, fuzzy c-means clustering, atlas-based methods, neural network-based techniques and watershed method. A few image segmentation methods are briefly explained below:

1.3.1 Geodesic Active Contour

This model is proposed by Caselles et al. [52]. It uses an active contour based on the minimization of energy and level set method for segmentation. The active contours grow in time according to intrinsic geometrical parameters of the image. These growing contours split and merge naturally, permitting the concurrent identification of multiple objects along with both inner and outer boundaries.

1.3.2 K-Means Clustering

Madhukumar et al. [51] experimented on k-means clustering-based segmentation. From a set of data points, k-means clustering attempts to group all the observations into k clusters. Each observation belongs to the cluster with the nearest mean, serving as a prototype of the cluster. Fuzzy c-means clustering (FCM) is a soft version of k-means clustering, where each data point has a fuzzy degree of belonging to each cluster.

1.3.3 Watershed Segmentation

Watershed segmentation algorithm is proposed by Vincent and Soille [53]. This method considers the image as a topological surface and the intensity value as height. The regional minimal values in the image are viewed as catchment basins and the maximal values between every two neighboring catchment basins are interpreted as ridgelines. Watershed-based segmentation locates the ridgeline called watershed within the image. This algorithm is usually applied to a gradient image where the object corresponds to the catchment basins while the boundary to the watershed. This algorithm suffers from over-segmentation problem due to the noise and local irregularities of the gradient [54].

1.3.4 Region Growing Method

In the region growing scheme, firstly, a set of seeds are identified. Later, the neighboring pixels are grouped to these seed points using the predefined criteria of similar intensity, texture or color. The skill of the selection of seed points is very important for the region growing due to unavailability of prior information [54]. This method requires manual intervention for inserting one or more seeds in each region. Moreover, its sensitivity to noise leads to the generation of holes causing extracted regions to get disconnected [48].

1.3.5 Self-Organizing Map Artificial Neural Network

This algorithm is proposed by Kohonen [55]. It produces self-organizing feature maps similar to those which occur in the brain. This network has two layers. The first layer contains input nodes and the second layer contains output nodes. The output nodes are arranged in two-dimensional grids. Each input node is connected to each output node using

adjustable weights. The self-organizing feature map moves the weights towards the center of clusters by updating the weights on each input value.

1.3.6 Atlas-based Segmentation

The atlas-based segmentation algorithms depend on the existence of a reference image (atlas) in which ROIs have been carefully segmented, manually or using a semi-automatic segmentation method. These segmented ROIs are considered as binary masks. To segment a new image, a transformation that registers the atlas to that image is computed. This transformation is used to deform the binary masks from the atlas onto the patient image to segment it [56].

1.4 MOTIVATION

While discussions with the neuro-radiologists and neurosurgeons it was observed that they consider the CT image along with MR image for locating the site of biopsy or for identifying the suitable location of cut in the bone so that the associated disease such as tumor can be removed from the brain. MR images are generally considered by the radiologists to identify the diseases related to a soft tissue region of the brain. It is difficult to identify the exact location and size of skull bone and other hard tissues by analyzing an MR image and the guess made by the experts on MRI using CT image varies from person to person. The manual method of identifying the exact location and size of bone on the MR image is rather subjective and depends upon the experience of radiologists. A separate evaluation of CT and MRI for disease detection and surgical procedures is not rapid because of the time taken by the manual method of visualization. Hence, there is a need to combine the CT and MR images with the help of computer technology to help the radiologists in their decision making. The process of mixing MRI information with CT images is termed as fusion.

The challenges faced by the researchers during image fusion are (i) different sizes and resolutions of CT and MR images (ii) intensity in-homogeneities of MR images (iii) the computational complexity of the algorithm in fusing the useful source information (iv) noise in CT and MR images. Hence there is a necessity to develop a robust fusion scheme that can take care of these points.

Challenges are faced by the researchers in the segmentation of lesions due to (i) similar morphology, contrast and brightness of surrounding tissues (ii) possibility of missed information due to human error (iii) artifacts introduced during image acquisition such as intensity inhomogeneities in MR images (iv) misclassification of tissues due to blurred edges. Hence, there is a need to develop a scheme that can blend the fusion information in

the form of clustered images. It is also required to minimize or reduce these limitations so that the disease classification accuracy can be improved.

The accurate separation of edema from the tumor has been a challenging task for many segmentation techniques and researchers. The challenges faced in the accurate detection of brain abnormalities such as tumor and edema arise due to the similarity of diseased tissues with normal tissues. Accurate detection and separation of diseased regions from the surrounding tissues are necessary to reduce the damage to the normal parenchyma during surgery. Hence, radiologists need advanced automatic methods for proper surgical planning, delineation and diagnosis of the diseases.

State of the art literature also reveals that most of the fusion and clustering studies employ open-source internet repository datasets. Further, these datasets are collected from a single source (site). These open-source datasets are generally superior in quality. There are very few studies employing local real-time datasets. The real-time datasets are different from the internet repository datasets in terms of their quality. Hence, there is a need to test the performance of developed methods on real-time datasets to verify the robustness and clinical application of the developed algorithms.

There are many fusion and segmentation methods developed by the researchers throughout the world in the past. However, very few authors have tried the fusion images in the segmentation or clustering of abnormalities. Hence, the present work tries to fill the gap in this regard also.

Therefore, fusion and clustering schemes are developed to assist radiologists and medical students in identifying the region of interest (ROI) w.r.t. bone. This ensures the insertion of surgical instruments from a minimal distance directed towards the disease. Thus reducing the risk of expurgating the normal brain parenchyma. This is the utmost area of concern during pre and post-surgery. Thus the proposed methodology assists both the radiologists and surgeons during surgical procedures of neuro-diseases. Also, the findings by the proposed methodology and the techniques proposed have not been reported earlier as per the knowledge of the author.

1.5 OBJECTIVES OF THE PRESENT STUDY

Image fusion has emerged as an active area of research because of its vast applications in the medical field. Inspired by this fact the following objectives are set for the presented thesis.

1) Pre-processing of CT and MR images
2) Development of fusion algorithms for CT and MR images

3) Segmentation of regions of interest (ROIs) to detect abnormalities on MR and CT images

4) Detection of the abnormalities by objective and subjective evaluation of the proposed fusion algorithms

1.6 CONTRIBUTION OF THE THESIS

In this research, three different fusion schemes are developed which employ three different multi-scale decomposition transforms. The best fusion scheme is utilized in the detection of abnormalities in the fusion images. The first scheme is the NSST based fusion method in which morphological gradient is employed with a pulse coupled neural network in a novel way to construct the HF fusion rule. The second scheme is a hybrid fusion scheme that employs NSCT and stationary wavelet transform. In this scheme, the stationary wavelet transform is employed in a novel way to construct the LF fusion rule. The third scheme is the NSST based scheme in which the smallest uni-value segment assimilating nucleus based new fusion rule is employed. The visual and quantitative analysis and comparison of these schemes are done with a few state of the art schemes. The best fusion scheme out of these three methods is selected for the detection of abnormalities in the fusion image. The fusion images obtained from the hybrid fusion scheme are clustered using four different clustering schemes to detect the abnormalities in the fusion image.

1.7 ORGANIZATION OF THE THESIS

The contents of this thesis are organized into eight chapters. The present chapter is a general introduction of the topic and states the objectives of the thesis. The remaining chapters of the thesis are organized as follows:

Chapter 2 contains classification and discussion on the important points of some of the state of the art fusion and segmentation methods. The contributions of classical fusion and segmentation methods are also discussed.

Chapter 3 gives the research workflow, the detailed description of the datasets used in different fusion and clustering methods to detect the abnormalities, the criteria of visual and parametric analysis. The detailed description of the fusion and clustering quality assessment parameters is given in this chapter.

Chapter 4 provides a detailed description of the proposed non-subsampled shearlet transform and pulse-coupled neural-network-based novel fusion scheme using the morphological gradient as HF fusion rule. The research is compared with states of the art fusion schemes using two different datasets of CT and MRI.

Chapter 5 provides a hybrid fusion method based on stationary wavelet transform (SWT) and NSCT. The proposed fusion method is qualitatively and quantitatively compared with four recent NSST and one adaptive sparse representation (ASR) based fusion scheme. The CT and MRI datasets obtained from different sources are used for comparison with other fusion schemes.

Chapter 6 gives a description of multimodal medical image fusion using the non-subsampled shearlet transform, a sum of Gaussian weighted pixel intensities and the smallest uni-value segment assimilating nucleus (SUSAN). The proposed scheme is compared visually and quantitatively with five recent fusion schemes. Statistical comparison is done using Wilcoxon signed ranks test with five recent fusion schemes.

Chapter 7 gives a visual and qualitative comparison of four clustering schemes in the detection of abnormalities in the fused brain CT and MR images which are obtained from NSCT and SWT based hybrid fusion scheme. The visual comparison of the abnormality detection is also done using clustered MR images with clustered fusion images.

Chapter 8 provides an overall conclusion of the thesis and the future scope of the work presented in this thesis.

CHAPTER 2

LITERATURE REVIEW

2.1 INTRODUCTION

Presently, the multimodal image fusion schemes have become a typical class of fusion schemes due to their significant role in healthcare. CT and MRI are some of the important imaging modalities from which the fusion process can harvest their complementary information. These complementary details obtained through the fusion can be helpful in the segmentation process to identify the region of interest. This chapter focuses on existing schemes related to the fusion and segmentation of brain CT and MR images. While the fusion work has varied literature, the classical fusion methods can be broadly grouped into two types mentioned as follows:

(1) Spatial domain fusion methods

(2) Multiscale image decomposition transform (MIDT) domain fusion methods

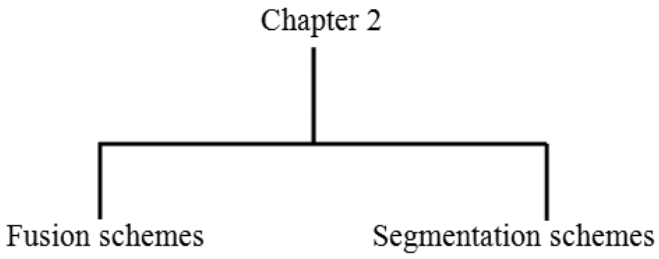

Figure 2.1 Classification of the literature survey of the thesis

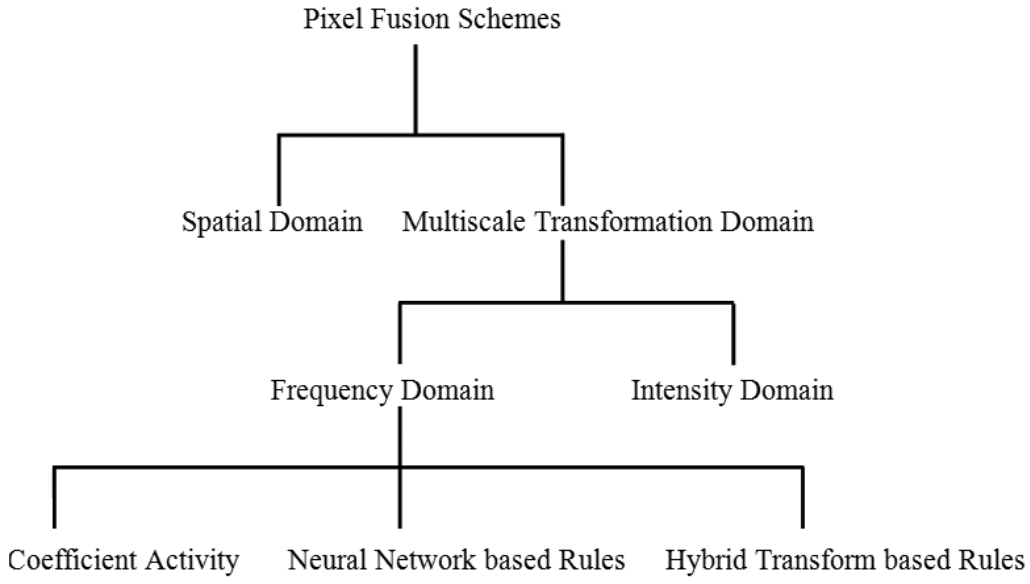

Figure 2.2 Classification of pixel level fusion schemes

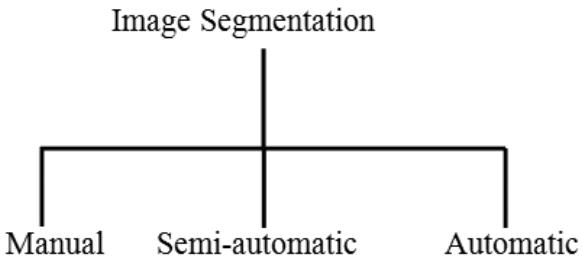

Figure 2.3 Classification of segmentation methods

Figure 2.1 shows the broad classification of the literature survey included in this thesis and figure 2.2 gives the classification of pixel-level fusion schemes. Pixel level fusion schemes are classified into spatial domain and transform domain fusion schemes. In spatial domain fusion methods, intensity or color information of source images are fused directly in a linear or nonlinear way. These methods are also called as single scale methods. The average scheme is the oldest and straightforward method of spatial domain fusion schemes. However, this method heavily degrades the fine details of the source images in its fusion outcome and introduces spatial distortion. An alternative to this scheme is block processing in which sharper blocks of source images are selected in image fusion. Li et al. [57] have proposed a block-based spatial domain fusion method in which spatial frequency is employed as an activity measure. The block-based schemes provide better results as compared to simple average method however, block effects are introduced in the fused image of these schemes. Small size blocks increase noise and larger size blocks blur the image and lose edge information. Another scheme is region-based processing in which image objects are segmented into regions. Local features such as regional gradient or local standard deviation are computed and employed in fusion rules. However, segmentation is a complex process and it is difficult to efficiently segment and fuse different objects. Vanmali et al. [58] proposed another scheme which is based upon the blending of intensities of source images in the fused image based upon a selection map. In principal component analysis (PCA) and iterative component analysis (ICA) based spatial schemes the source images are transformed into uncorrelated images and then fusion rules are applied to them. The authors in [59] have developed a fusion methodology that is based upon PCA. The pixels with sharp principal components are selected to construct the fusion image. The PCA and ICA based methods give a compact representation of the data into fewer bands however, they lack the spectral information of source images. A few authors applied neural networks in spatial domain fusion [60, 61]. Li et al. [60] have applied artificial neural

network (ANN) in fusion. In this scheme, the source image is divided into blocks and three features named SF, visibility and edges of these blocks are computed. These features are employed to train the ANN. Wang and Ma [61] proposed a multichannel pulse coupled neural network (PCNN) based scheme in which pixel intensity of source images is fed as an external input to PCNN. The spatial domain-based neural network schemes face the loss of information. Edge preserving adaptive manifold filter is employed in spatial domain recently in [62], however, the scheme also loses some spectral details and contrast in the fused image. Table 2.1 shows the spatial domain fusion schemes with their contributions and a few other important details.

The multiscale image decomposition transform (MIDT) based schemes gained special attention from researchers because of their ability to analyze an image at different scales. The response of these transforms matches the response of the human visual system to images whereas, spatial domain methods do not give importance to human vision effect. These schemes are preferred if an image contains small and large objects or low and high contrast tissues simultaneously. Multi-resolution processing can be done in the frequency domain or in the intensity domain. Accordingly, MIDT schemes are broadly classified as intensity domain MIDT and frequency domain MIDT.

In intensity domain transforms, images are analyzed at different resolutions using intensity pyramids. The Gaussian pyramid is an example of such pyramids in which the coarser-resolution pyramid is constructed by eliminating consecutive rows and columns from the fine resolution pyramid. The Gaussian pyramid is simple in design however, it gives blurred fusion results. Laplacian pyramid is derived from the Gaussian pyramid which gives good fusion results [63]. However, it is susceptible to unnecessary artifacts and noise. The ratio of low pass pyramid [64] is formed by the ratio of two successive layers which produces too much imprecise information. The morphological pyramid is constructed by the difference of initial image and its morphological filtered image [65] however, it produces many undesirable artifacts. Table 2.2 shows spatial (intensity) domain multiscale fusion schemes along with their contributions, various compared schemes and parameters used for comparison. All these intensity domain pyramidal transforms are effective in extracting the spatial information as compared to spatial domain methods, however, they lack in spectral information. This necessitates the use of pyramids in the frequency domain.

In frequency domain multiscale transforms, an image is split into the base layer and detail layers at different scales and directions. There are various frequency domain multi-scale transforms which can be employed in fusion such as discrete wavelet transform (DWT) [40,

66-69], curvelet transform (CVT) [70, 71], nonsubsampled contourlet transform (NSCT) [35], framelet transform (FT) [38], nonsubsampled shearlet transform (NSST) [2, 3, 39]. In the past several fusion algorithms using wavelet transform are implemented by many authors however, wavelet-based methods suffer from poor directional selectivity and cannot resolve curves. Moreover, these methods are not shift-invariant. The shift variance problem of DWT is removed by the stationary wavelet transform (SWT). SWT is better in extracting the image texture however, it also has limited directionality. Curvelet transform as proposed by Starck et al. [34] is capable of representing smooth curves. However, curvelet-based methods suffer from redundancy, complexity and are not suitable for noisy images. Moreover, curvelets cannot be constructed in a digital field directly. Further improvement in this series is provided by the contourlet transform proposed by Do and Vetterli [72]. However, this transform suffers from the Gibbs phenomenon and is the shift variant. These problems of contourlets are solved by nonsubsampled contourlet transform (NSCT). NSCT can resolve curves and contours finely though, it is unable to report point singularities. Non-subsampled shearlet transform (NSST) is a recently developed multi-scale geometric analysis model that is computationally more efficient than NSCT. NSST can extract the directional and geometrical properties of an image such as curved shapes, scales and oscillations [73]. It can reduce the effect of misregistration of source images on the fused image [44, 73].

Another important aspect that governs fusion quality is fusion rule. Fusion rule represents the method to combine the decomposed coefficients of a multiscale transform to obtain the fusion image. Fusion rules can be derived directly from the activity of coefficients, using neural networks or using hybrid fusion methods. Accordingly, these can be classified into three categories as coefficient activity governed fusion rules, neural network motivated fusion rules and hybrid transform based fusion rules.

Coefficient activity-based fusion rules are designed for LF and HF subbands separately keeping in view the fact that these subbands carry a different amount of image information. LF subband carries the smooth part of an image hence, the simplest rule that is used to merge the LF band coefficients is averaging. Even so, this rule degrades the quality of the fused image by reducing its contrast as compared to parent source images. The detail subbands carry the high-frequency edges and contours, hence the basic rule used to fuse detail subbands is to select the coefficients with absolute maximum value. This rule is simple to implement and is faster in computation. Nevertheless, it is prone to noise as the single pixel is used in deciding the fusion rule. In order to solve this problem, a few

neighbor pixels of the current pixel are involved in deciding the fusion rule. The energy of the current pixel is computed by applying different operations on these neighbors and the current pixel. The authors have applied different neighborhood operations to design various fusion rules. Yang et al. [74] fused one pair of CT and MR images using the discrete wavelet transform. In this scheme, the authors applied a visibility-based scheme and a variance-based method to fuse low and high-frequency bands, respectively. Vijayrajan and Muttan [75] applied the discrete wavelet transform to fuse two sets of CT and MRI obtained from internet websites. The authors utilized the average of principal components as weights for fusion rule. The experimental results were compared with SWT, NSCT, complex wavelets, etc. Singh and Khare [76] performed image fusion on two pairs of CT and MR images collected from the internet repository. In the developed methodology, the authors applied Daubechies complex wavelets and utilized maximum selection rule. The method outperformed the spatial domain and other wavelet domain methods visually and quantitatively. Bhattacharya et al. [77] fused T1 weighted, T2 weighted and proton density MR images using genetic algorithm (GA) and wavelet transform. The fusion process was implemented on segmented images of the brain. Segmentation was done using fuzzy c-means (FCM), iterated conditional modes (ICM) and Gibbs segmentation technique. The maximum selection and averaging schemes were applied to fuse HF and LF sub-bands, respectively. The maximization of HF subband coefficients was done through the genetic algorithm. The ICM and Gibbs based segmentation methods gave comparable fused images compared to FCM based images. Ellmauthaler et al. [78] applied the undecimated wavelet transform in fusion. In the developed methodology the authors applied averaging and maximum selection based rules along with interscale and intrascale grouping. Ali et al. [79] experimented on one pair of images using curvelet transform and applied maximum frequency as fusion rule. Xu et al. [71] applied a uniform discrete curvelet transform to fuse one pair of CT and MR images. The feature similarity index based fusion rule was used for low pass sub-band coefficients and a complex coefficients feature similarity index based rule for high pass sub-band coefficients. Yang et al. [80] fused 3 sets of CT and MR images based upon multiscale geometric analysis of contourlet transform. The local regional energy and local luminance contrast based fusion rules were developed. The authors in [81] applied shift-invariant shearlets in fusion. In their scheme, the authors applied interscale and intrascale dependencies with maximum selection rule. Das and Kundu [82] applied NSCT in the fusion of 2 pairs of CT and MR images. This scheme applied a neuro-fuzzy approach along with average energy and local information entropy-based fusion rules. Darwish [83]

did multilevel fuzzy contourlet based fusion on two datasets of CT and MRI obtained from internet repository. The feature based fuzzy fusion rule (visibility based scheme) was applied to low frequency approximation coefficients. The authors utilized pixel based fuzzy fusion rule (variance based method) to high frequency band coefficients of contourlet transform. Ganasala and Kumar [45] worked on nonsubsampled contourlet transform to fuse two datasets of CT and MR images obtained from internet repository. The authors proposed entropy of square of the coefficients within a local window as LF rule and maximum weighted sum-modified Laplacian as HF coefficient selection rule. Bhatnagar et al. [84] used NSCT with Shannon entropy-based LF fusion rule and directive contrast based HF rule to fuse two sets of CT and MR images. Gomathi and Kalaavathi [85] used nonsubsampled contourlet transform with mean based and variance-based fusion rules to fuse one pair of brain CT and MR image. Bhatnagar et al. [38] experimented on four sets of CT and MR images using the framelet transform. Low and high-frequency subband coefficients were fused using visibility measure based rule and texture information based rule, respectively. Miao et al. [86], Liu et al. [44] and Yin et al. [87] have done fusion of one set of CT and T1-weighted MR image using nonsubsampled shearlet transform. Miao et al. [86] applied averaging scheme to fuse LF components and absolute maximum within a 3×3 neighborhood as HF fusion rule. Liu et al. [44] applied regional energy as LF fusion rule and multiple regional features based HF fusion rule. Yin et al. [87] utilized adaptive weighted averaging and novel sum modified Laplacian based fusion rules. Ganasala and Kumar [2] fused 9 pairs of CT and MRI using NSST. Sum of variation in the squares of the coefficients, absolute maximum and the sum of absolute differences of successive rows and columns were the fusion rules applied. In a similar way Liu et al. [88] used morphological component analysis and sum modified Laplacian based rules with NSST. Table 2.3 shows a few state of the art fusion schemes which use coefficient activity governed fusion rules, along with compared schemes and various parameters used for comparison.

In neural network motivated fusion rules, artificial neural models are employed. One such model is the pulse coupled neural network (PCNN) which has found vast applications in medical image fusion. It simulates the activity of visual nerve cells and shows a remarkable relationship between neurons firing frequency and image contrast [89]. The pixels with higher firing instances show a higher activity level. This bio-inspired activity level in various forms can be used to construct the fusion rules of different multiscale transforms governed fusion schemes. PCNN was applied successfully with NSCT for the first time by Feng and Liu [90]. The activity level in the form of spatial frequency (SF) motivated PCNN

in NSCT has proposed in [90]. Xiang et al. [91] applied sum modified Laplacian and modified spatial frequency as motivation to PCNN with NSCT. The authors in [92] applied NSST and spatial frequency motivated PCNN. Cheng et al. [89] have used shearlets with PCNN and gradient feature and variance-based fusion rules. Kong et al. [43] have applied SF with PCNN and NSST. The activity level in the form of energy of the edge in pulse coupled neural network (PCNN) has used with NSCT in [93]. Ganasala and Kumar [3] applied a sum of directional gradients motivated PCNN in the NSST domain. Singh et al. [94] have applied regional energy as a saliency measure and normalized sum modified Laplacian with PCNN as fusion rule in NSST. The authors in [95-97] have also utilized NSST along with PCNN. The authors in [95] applied minimum firing times of different subbands neurons as activity measure, [96] used optical flow graph of simplified PCNN and [97] used maximum firing times of PCNN as its fusion rule. In the schemes [43, 95] normalized coefficients of NSST and in [98] normalized coefficients of NSCT were fed as an external stimulus to PCNN. Positive and negative coefficients in detail sub-bands of NSST represent the edges and contours details from various different angles [95]. Hence, it is not a good idea to normalize these coefficients. Moreover, most of the saliency measures used with PCNN based fusion rules increase the computational time of the fusion algorithms. These points are considered in the present research. Neural network-based fusion rules are discussed in detail in Table 2.4.

In hybrid transform based fusion rules, two different multiscale decomposition transforms are used. These transforms are combined to obtain their complementary characteristics such as edges, texture or contrast in the fused image. One of the transforms is used to decompose the source images whereas, the other transform is utilized to form the fusion rule for LF subband or HF subband or both subbands. Table 2.5 shows the fusion schemes which employ hybrid transform based fusion rules. Li and Yang [99] decomposed the images using the curvelet transform. All the decomposition subbands were fused using SWT where the absolute maximum rule was applied. Li and Yang [100] decomposed the images using NSCT and applied SWT along with average and absolute maximum selection fusion rule for LF and HF coefficients, respectively. Zhou [101] applied SWT for image decomposition. The LF components were fused using the curvelet transform based fusion method. The HF components were fused directly using absolute maximum value. Agrawal and Bedi [70] used the wavelet transform for image decomposition and curvelet transform in fusion rule. Yang et al. [102] used a fast discrete curvelet transform along with the spatial model where the sum modified Laplacian based neural network was applied. Jin et al. [103]

Table 2.1 Spatial Domain Fusion Schemes

Author	Year	Method	Dataset	Fusion Rules	Parameters	Comparison with	Contributions
Li et al. [57]	2001	A spatial domain scheme in which images are divided into blocks and SF of these blocks is computed. The pixels with high SF constitutes the fused image.	2 pairs of multi-focus images.	Maximum selection and averaging of SF	Root mean square error (RMSE)	Wavelet transform with different filters	A novel fusion scheme in which spatial frequency is employed as an activity measure in the spatial domain.
Li et al. [60]	2002	A block-based approach using artificial neural network (ANN).	4 pairs of multi-focus images.	SF, Visibility and edge features as activity measures	RMSE, mutual information (MI)	DWT, probabilistic neural network, radial basis function network	An ANN-based scheme in which 3 different features namely SF, visibility and edge features of source images are computed using a block-based approach. The difference in features of source images is used to train the ANN.
Wang and Ma [61]	2008	A multi-channel pulse coupled neural network-based scheme in which the source image intensity is applied directly as an external stimulus to PCNN.	2 pairs of CT and MRI, 1 pair of T1-W MR and T2-W MR, 1 pair of PET and T1-W MR	Firing times of the neurons	Mutual information	Contrast pyramid, gradient pyramid, Laplacian pyramid, ratio pyramid, morphological pyramid, DWT, pixel averaging, filter-subtract-decimate (FSD) pyramid	A novel medical image fusion scheme which introduces the multi-channel PCNN in the fusion field.

Vanmali et al. [58]	2013	The scheme blends the intensities of two images based upon a selection map.	16 pairs of multi-exposure images	Gaussian weighted selection map	Root mean square contrast, saturation, entropy, execution time	Luminance transformation, exposure fusion	The resultant fused images are unaffected by the ghosting artifacts and the fusion algorithm is computationally efficient.
Wan et al. [59]	2013	Principal component analysis	4 pairs of multi-focus image	Maximum selection and averaging with consistency verification	MI, edge information quality index ($Q^{AB/F}$), structural similarity index, run time	DWT, SF based spatial domain	The scheme presents the application of PCA in spatial domain fusion which employs the most significant features of a sparse matrix in the fusion process.
Geng et al. [62]	2015	A modified local contrast-based scheme in which LF subband is generated using an adaptive manifold filter and HF subband is produced using modified spatial frequency.	2 pairs of CT and MRI, 2 pairs of T1-W MRI and T2-W MRI, 1 pair of T1-W MRI and Gadolinium contrast MRI, 1 pair of T1-W MRI and MRA (magnetic resonance angiogram).	Modified local contrast	MI, $Q^{AB/F}$	Spatial domain guided filter method, PCA, dual-tree complex wavelet transform (DTCWT), Laplacian pyramid, gradient pyramid, NSCT	The scheme employs novel modified local contrast-based fusion rule and preserves better edge details and diffusion information in the fused image.

Table 2.2 Intensity-based Multi-Scale Transformation Domain Fusion Schemes

Author	Year	Transform	Dataset	Fusion Rules	Parameters	Comparison with	Contributions
Burt and Adelson [63]	1985	Laplacian pyramid	1 pair of Multi-focus images	Maximum absolute selection	The images are compared visually only. No fusion assessment parameters were used.	The composite image formed without multiresolution analysis	The scheme is based on pattern decomposition of images that employs a Laplacian pyramid. The scheme shows the superiority of multi-resolution analysis in image fusion.

Toet [64]	1989	The ratio of low pass pyramid	1 pair of synthetic images	Maximum absolute contrast	The images are compared visually. No fusion assessment parameters are used	Gaussian pyramid, the difference of Laplacian pyramid	A good fusion scheme demonstrating the application of contrast pyramids in image fusion. The visual fusion results were superior to Gaussian and Laplacian pyramid based schemes.
Toet et al. [104]	1989	The ratio of low pass pyramid (contrast pyramid)	2 pairs of thermal and visual images	Maximum absolute contrast	The images are compared visually only. No fusion assessment parameters are used.	Gaussian pyramid, the difference of Laplacian pyramid	The fusion scheme demonstrates the use of the ratio of low pass pyramids and absolute maximum contrast based rule in the fusion of thermal and visual images.
Mukhopadhyay and Chanda [65]	2001	Multi-scale morphology	1 pair of CT and MR image	Prominent bright and dark feature selection from individual images at different scales.	Error, similarity	Averaging, Karhunen–Loeve (K-L) transform, morphological pyramid	The scheme employs morphological towers to extract the features at different scales. The best bright and dark features are included in the fused image. The scheme is found to be better than other schemes visually and quantitatively.
He et al. [105]	2010	Intensity, hue, saturation (IHS) model and PCA	3 pairs of PET and MRI	Adaptive selection	MI	Brovey, PCA, DWT	The scheme preserved better spatial and functional information with minimum distortion.
Bai [106]	2013	Top hat transform	2 pairs of CT and MRI, 1 pair of multi-focus images, 1 pair of infrared and visible images	Maximum pixel value	Entropy, joint entropy, SF, mean gradient, universal image quality metrics, time	Average, PCA, wavelet pyramid, morphological pyramid, fast Fourier transform (FFT)	A very good fusion scheme which employs a morphology-based contrast operator to extract the bright and dark features of the images. The predominant features are employed to construct the fused image.

Table 2.3 Frequency-based Multiscale Transformation Domain Coefficient Activity Governed Fusion Rules

Author	Year	Transform	Dataset	Fusion Rules	Parameters	Comparison with	Contributions
Yang et al. [80]	2008	Contourlet transform	3 pairs of CT and MRI images	Local energy and regional contrast	Standard deviation (SD), entropy (ENT), SF, universal image quality index (UIQI), overall cross-entropy (OCE)	Averaging, PCA and DWT	A very good fusion scheme in which the concept of contourlet contrast measurement is applied. This feature gives better visual results comparable to the human visual system.
Ali et al. [79]	2010	Curvelet transform	2 pairs of CT and MRI images	Maximum frequency as LF and HF rule	Peak signal to noise ratio (PSNR), similarity	PCA, DWT	A very good curvelet based fusion scheme which performs well compared to PCA and DWT.
Yang et al. [74]	2010	Discrete wavelet transform	1 pair of CT and MRI images, 1 pair of multi-focus images, 1 pair of remote sensing images	Visibility-based scheme and a variance-based method	Average gradient, OCE, ENT	pixel averaging and DWT	The method is effective for fusion, quantitative values are corresponding to visual effects.
Miao et al. [86]	2011	Shearlet transform	1 pair of CT and MRI, 1 pair of remote sensing image, 1 pair of multi-focus image	Averaging and absolute maximum	ENT, SD, SF, Structural similarity index	Laplacian pyramid, PCA and wavelet	A shearlet based fusion scheme which is better in reducing structural distortion in the fused image and good in improving detail information.
Bhatnagar et al. [38]	2013	Framelet transform	Four pairs of CT and MRI, 3 pairs of CT and PET	Visibility measure and texture information	Mean, SD, ENT, SF, MI, structural similarity (SSIM), $Q^{AB/F}$,	PCA, contrast pyramid, gradient pyramid, wavelet transform and contourlet transform	The scheme preserves and improves spatial details. Simple sampling & smoother scaling produces good results.

Bhattachary a et al. [77]	2012	Discrete wavelet transform and segmentation	1 pair of T1-W and T2-W MR, 1 pair of PD-MR and T1-W MR images	Genetic algorithm with averaging and max. selection	MI, computation time	FCM based fusion, iterated conditional mode based fusion, Gibbs based fusion	A very good fusion scheme based on the segmentation of the source images.
Ellmauthal-er et al. [78]	2013	Undecimated wavelet transform	5 pairs of CT and MRI, 10 pairs of infrared and visible images, 5 pairs of multi-focus images	Averaging and maximum selection with interscale and intrascale grouping	$Q^{AB/F}$, MI, Piella metric	DTCWT, NSCT	Parameters were superior for the method. Spectral factorization improved fusion results.
Das and Kundu [82]	2013	Nonsubsampled contourlet transform	1 pair of CT and MRI, 1 pair of T1-MR and magnetic resonance angiography (MRA) images, 1 pair of fluid attenuation inversion recovery (FLAIR) and DWI MR, 1 pair of PET and MR, 1 pair of PET and CT images	Neuro-fuzzy approach, local average energy and local information entropy	SF, ENT, SD, MI, $Q^{AB/F}$	Contourlet, curvelet, wavelet, PCNN, NSCT-PCNN	The proposed scheme gives a good contrast image and better fusion parameters.
Xu et al. [71]	2013	Uniform discrete curvelet transform	1 pair of CT and MR image, 1 pair of remote sensing image, 1 pair of multi-focus images, 1 pair of low light television (LLTV) sensor and thermal imaging forward-looking infrared (FLIR) sensor image	Feature similarity index	MI, ENT, $Q^{AB/F}$	DWT, contourlet transform (CNT), NSCT, shiftable complex directional pyramid transform,	This scheme preserved the source texture and improved the spatial details of source images in fusion outcome.

Darwish [83]	2013	Contourlet transform	2 pairs of CT and MRI	Visibility based fuzzy rule, variance-based fuzzy rule	ENT, MI, image quality index (IQI)	Fuzzy k means, fuzzy contourlet, hybrid fusion-based wavelet transform	The proposed system removes fusion artifacts and improves visual outcomes by considering the physical aspects of transform coefficients.
Wang et al. [81]	2014	Shift invariant shearlet transform	1 pair of MRI and SPECT, 2 pairs of MRI and PET images	Interscale and intrascale dependencies with maximum selection	ENT, MI, SD, $Q^{AB/F}$, PSNR, structural similarity index	IHS, DWT, contourlet transform, NSCT, shearlet transform (ST)	The scheme uses shearlets and Markov random fields to obtain improved visual details and to reduce color distortion. The scheme uses the concept of interscale and intrascale dependencies in the shearlet domain.
Singh and Khare [76]	2014	Discrete wavelet transform	2 sets of CT and MRI, 1 set of MRA and T1-W MRI	Maximum selection	ENT, SD, $Q^{AB/F}$, MI, SF, average gradient, blind SSIM	Gradient pyramid, ratio pyramid, contrast pyramid, PCA and wavelet domain methods	Visual and quantitative results are improved, better average information in the fused image.
Ganasala and Kumar [45]	2014	Nonsubsampled contourlet transform	10 pairs of CT and MR images	The entropy of square of the coefficients and maximum weighted sum-modified Laplacian	MI, ENT, $Q^{AB/F}$, SF, special frequency error, correlation coefficient (CC), OCE, universal image quality metrics	Pixel average, DWT, CNT, NSCT	Fusion rules give the best results. Qualitative and quantitative analysis shows the superiority of the proposed method.
Yin et al. [87]	2014	Nonsubsampled shearlet transform	1pair of CT and MRI, 4 pairs of multi-focus images	Singular value decomposition local structural descriptor based adaptive weighted averaging and novel sum modified Laplacian	MI, $Q^{AB/F}$	Gradient pyramid (GP), DWT, contourlet, shearlet, NSST	The scheme proposes novel fusion rules based on singular value decomposition and sum modified Laplacian which prove to be superior to other fusion schemes.

Ganasala and Kumar [2]	2014	Nonsubsampled shearlet transform	9 pairs of CT and MRI, 9 pairs of MRI and SPECT images	Sum of variation in the squares of the coefficients, absolute maximum and the sum of absolute differences of successive rows and columns	Mutual information, standard deviation, universal image quality index based metrics, SF, $Q^{AB/F}$, CC, bias, normalized mutual information (NMI), filtered correlation coefficient (FCC), computation time	NSCT, NSST	Parameters were higher compared to other methods. The proposed rules work better compared to regional average and contrast based rules.
Liu et al. [44]	2014	Nonsubsampled shearlet transform	1 pair of CT and MRI, 9 pairs of multi-focus images	Regional energy, regional average gradient, regional spatial frequency, regional variance	ENT, SD, SF, average gradient, the difference of entropy, PSNR, mean square error, SSIM	Laplacian pyramid (LP), average, wavelet, contourlet and shearlet transform	A very good fusion scheme demonstrating the construction of hybrid fusion rules using regional energy-based parameters.
Bhatnagar et al. [84]	2015	Nonsubsampled contourlet transform	2 pairs of CT and MRI, 2 pairs of T1-W and T2-W MR images	Shannon entropy and directive contrast	MI, SSIM based metric	PCA, gradient pyramid, DWT, contourlet, NSCT	An NSCT based scheme employs entropy and directive contrast of LF and HF sub-bands, respectively to enhance the clarity and texture in the fused image.
Vijayrajan and Muttan [75]	2015	Discrete wavelet transform	2 pairs of CT and MRI images, 3 pairs of PD-MR and T2-W MR images	Average of principal components as weights	Average MI, average PSNR, UIQI	SWT, DWT, NSCT, complex wavelets, PCA, local principle component averaging, FCM-PCA averaging	The parameters values obtained were higher compared to other rules. The visual and quantitative analysis was better than other methods.

Gomathi and Kalaavathi [85]	2016	Nonsubsampled contourlet transform	6 pairs of CT and MRI	Mean and variance	ENT, STD, Mean, $Q^{AB/F}$	Pixel averaging, DWT, NSCT	A novel NSCT based fusion scheme which employs mean and variance-based fusion rule.
Liu et al. [88]	2016	Nonsubsampled shearlet transform	1 pair of CT and MRI, 1 pair of multi-focus images, 1 pair of infrared and visible images	Morphological component analysis selection and sum modified Laplacian	ENT, $Q^{AB/F}$, universal image quality index, weighted fusion quality index, computation time	GP, DWT, NSCT, NSST, morphological component analysis	An NSST based scheme in which LF subband is fused using morphological component analysis and HF subband using sum modified Laplacian based fusion rule.

Table 2.4 Neural Network-based Fusion Rules

Author	Year	Transform	Dataset	Fusion Rules	Parameters	Comparison with	Contributions
Xiao et al. [90]	2008	Nonsubsampled contourlet transform	3 pairs of multi-focus, 3 pairs of infrared and visible images.	SF – PCNN	MI, $Q^{AB/F}$	Wavelet, contourlet, PCNN, contourlet-PCNN	A very good fusion scheme demonstrating the fusion of NSCT with PCNN which is motivated by spatial frequency feature.
Das and Kundu [92]	2012	Nonsubsampled shearlet transform	5 pairs of CT and MRI images	Maximum selection and modified spatial frequency motivated PCNN	SD, ENT, SF	NSCT-SF-PCNN, multi-wavelet basis, DWT, contourlet transform	A novel NSCT-PCNN scheme in which modified spatial frequency is used to motivate the PCNN. This feature well captures the differences and details of source images in the resultant image.
Cheng et al. [89]	2013	Nonsubsampled shearlet transform	1 pair of optical and SAR images, 1 pair of remote sensing, 1 pair of hyperspectralimages	Gradient motivated PCNN	ENT, SD, $Q^{AB/F}$, average gradient, OCE	Average, LP, GP, contrast pyramid (CP), contourlet-PCNN, wavelet-PCNN	The novelty of this scheme exists in the use of shear matrix for multi-direction decomposition. Thereafter, DWT is employed to decompose the image on different scales. The directional gradient of coefficients is fed as input to PCNN.

Kong et al. [43]	2014	Nonsubsampled shearlet transform	2 pairs of visible and infrared images	SF - PCNN	SF, MI, ENT	NSST-PCNN, improved traditional NSCT-PCNN, ST, NSCT, NSST-improved ICM	This scheme proposes an improved PCNN model which is motivated by the spatial frequency of the transform coefficients.
Wang et al. [107]	2015	Nonsubsampled contourlet transform	3 pairs of multi-focus images	The energy of edge motivated PCNN	MI, $Q^{AB/F}$	Sum modified Laplacian-CNT, NSCT-PCNN, NSCT-SF-PCNN	This scheme proposes a novel fusion rule for LF and HF subbands in the NSCT domain which is based on the edge energy of the sub-bands.
Ganasala and Kumar [3]	2015	Nonsubsampled shearlet transform	9 Pairs CT and MRI, 5 pairs SPECT and MRI images	Sum of variation in squares of coefficients and sum of directional gradients - PCNN	MI, STD, $Q^{AB/F}$, SF, Piella metrics, bias, the filtered correlation coefficient	NSST-SF-PCNN, NSCT-improved dual-channel PCNN, NSST with energy and contrast, NSST and improved intersecting cortical model	Visual and quantitative analysis is better than other methods. Parameters obtained are higher compared to other rules.
Singh et al. [94]	2015	Nonsubsampled shearlet transform	10 pairs of CT and MRI images	Regional energy and normalized sum modified Laplacian - PCNN	ENT, MI, STD, SF, IQI, $Q^{AB/F}$	Wavelet, NSCT, NSST-PCNN	The main contribution of this method is in the use of new fusion rules with NSST. The scheme is better than DWT, NSCT and NSST based fusion schemes.
Kong et al. [95]	2015	Nonsubsampled shearlet transform	6 pairs of visible and infrared images	Minimum firing times of LF and HF subband neurons of the spiking cortical model.	SF, MI, ENT	NSCT, NSST	This scheme proposes a novel spiking cortical model with NSST which is found to be superior to NSCT and NSST based fusion methods.
Xiang et al. [91]	2015	Nonsubsampled contourlet transform	2 pairs of visible and infrared	Sum modified Laplacian, modified spatial frequency motivated PCNN	ENT, MI, SD, $Q^{AB/F}$	DWT, NSCT, NSCT-PCNN	This method suggests an adaptive PCNN model whose results are found to be suitable for fusion and superior to DWT, NSCT and NSCT-PCNN based fusion schemes.

Jin et al. [96]	2016	Nonsubsampled shearlet transform	6 pairs of multi-focus images	Maximum selection, average and average optical flow graph of simplified PCNN	Average gradient, SF, ENT, SD, MI, $Q^{AB/F}$, mean,	The weighted average, PCA, PCNN, DWT-PCNN, LP-PCNN and different color spaces	This scheme proposes a hue, saturation and value (HSV) color model with PCNN in fusion which proves to be superior to other schemes in comparison.
Yin et al. [97]	2019	Nonsubsampled shearlet transform	10 pairs CT and MRI, 13 pairs T1-W MRI and T2-W MRI, 30 pairs of MRI and SPECT, 30 pairs of MRI and PET images	The energy of modified Laplacian and maximum firing times of PCNN	SD, ENT, localized MI, Piella metric, visual information fidelity fusion	NSCT-SF-PCNN, guided filtering, LP-sparse representation (SR)	A novel fusion scheme in which energy of modified Laplacian is fed to PCNN to obtain the edge and texture information of source images.

Table 2.5 Hybrid Fusion Rules-based Schemes

Author	Year	Transform	Dataset	Fusion Rules	Parameters	Comparison with	Contributions
Li and Yang [99]	2008	Wavelet and curvelet transform	4 pairs of multi-focus images	Wavelet with absolute maximum selection	ENT, SF	DWT, curvelet transform	The hybrid scheme outperforms the wavelet and curvelet based scheme in relation to visual and parametric results.
Li and Yang [100]	2010	SWT and non-subsampled contourlet transform	1 pair of CT and MRI, 14 pairs of multi-focus and 1 pair of infrared and visible images	SWT with weighted averaging, maximum energy	RMSE, $Q^{AB/F}$, Piella metric, computation time	Complex wavelets, CVT, SWT, NSCT	Serial SWT aiding NSCT gives improved parameters and outperforms visually and quantitatively.
Zhou [101]	2012	Stationary wavelet and curvelet transform	3 pairs of infrared and visible images	Curvelets averaging and absolute maximum selection	ENT, SF, $Q^{AB/F}$, non-overlapping MI	SWT, DWT, curvelets	The hybrid combination of wavelets with second-generation curvelet transform extracts better spectral details of the source images in the fusion image.

Agarwal and Bedi [70]	2015	Wavelet and curvelet transform	1 pair of CT and MRI images	Curvelet transform with hybrid filter	ENT, RMSE, PSNR, CC, MI, $Q^{AB/F}$	Laplace transform, wavelet transform, curvelet transform, select maximum/ minimum, average	This hybrid scheme removes the ringing effect and produces smooth corners and edges in the fused image. All parameters except CC are better compared to other methods.
Yang et al. [102]	2017	Fast discrete curvelet and spatial model	05 pairs of multi-focus images, 01 pair of artificial images.	Hybrid spatial modal, sum modified Laplacian based neural network	RMSE, MI, $Q^{AB/F}$	PCA, gradient pyramid, DWT, fast discrete curvelet transform, NSCT, bilateral gradient-based sharpness criterion	A computationally faster hybrid scheme with improved fusion performance as compared to the various spatial domain and transform domain fusion schemes.
Jin et al. [103]	2018	Wavelet and discrete cosine transform	5 pairs of infrared and visible images	Discrete cosine transform with local spatial frequency	ENT, SF, SD, MI, $Q^{AB/F}$, mean value	Morphological difference pyramid, ratio pyramid, contrast pyramid, DWT, DT-CWT, NSCT, NSST	The hybrid combination of SWT with the discrete cosine transform outperforms different compared schemes in terms of visual and quantitative analysis.

have applied the discrete stationary wavelet transform to decompose the source images into base and detail layers. These layers were further decomposed by discrete cosine transform into LF and HF sub-layers where the local spatial frequency was applied as activity measure. It is seen from the literature that there are very few studies related to hybrid transforms based fusion rules. Hence this point is noted and a hybrid fusion scheme is proposed in the presented thesis.

Fusion schemes can be used along with segmentation methods in both ways i.e. fusion can be done after the segmentation process. Alternatively, segmentation of the fused image can also be done for the detection of abnormalities in the fused image. Figure 2.3 shows the categorization of segmentation algorithms. Segmentation schemes are broadly classified into three main types as manual segmentation, semiautomatic segmentation and fully automatic segmentation methods. Manual segmentation is done by manually marking the ROI. Tiwari et al. [108] performed manual segmentation of ROI to classify the tumors into various classes. However, the accuracy of segmentation varies among different experts and is easily susceptible to human errors. Moreover, manual segmentation is a very time-consuming process.

In order to reduce human intervention in manual segmentation semiautomatic methods are proposed by many authors [48, 52, 109-113]. Semiautomatic methods are partially manual and partially automatic. These methods require manual interaction to select the seed points and thereafter segmentation algorithm automatically segregates the object boundaries. These schemes have better accuracy, however, they require manual setting of the seed points. Wang et al. [109] experimented on fluid vector flow (FVF) and its applications in brain tumor segmentation to address problems of insufficient capture range and poor convergence for concavities. With the ability to capture a large range and extract concave shapes, FVF demonstrated improvements over techniques like gradient vector flow, boundary vector flow, and magnetostatic active contour on synthetic images, pediatric head MRI images and brain tumor MRI images. The geodesic active contour model was proposed by Caselles et al. [52]. It uses an active contour based on the minimization of energy and level set method for segmentation. The active contours grow in time according to intrinsic geometrical parameters of the image. These growing contours split and merge naturally, permitting the concurrent identification of multiple objects and both inner and outer boundaries. Sachdeva et al. [110] experimented on a content-based active contour model for brain tumor segmentation using MR images. Xie et al. [111] segmented brain tumor and edema using a hybrid level set method. The authors in [112] applied gradient

vector flow in segmentation. The authors in [113] proposed magnetostatic active contour model for the segmentation of brain MR images. Banerjee et al. [48] performed multilevel thresholding for the segmentation of 160 MRI slices of 25 patients. The scheme employs discrete curve evolution in thresholding. The ROI is segmented using a single seed selection.

In order to eliminate the drawbacks of semi-automatic methods, automatic segmentation methods are proposed. These methods use automatic algorithms to detect the boundaries of the objects. Clustering techniques, neural networks, atlas-based schemes and multiresolution analysis methods are a few examples of such algorithms. Vijayakumar et al. [114] performed segmentation and grading of brain tumors on apparent diffusion coefficient images (ADC). Their method used a mixture of unsupervised artificial neural networks and multiresolution wavelets. Zhang et al. [115] applied the support vector machine and region growing for tumor segmentation. Torabati et al. [116] did segmentation of a CT image, 10 MRI images of the brain and 30 ultrasound images of the breast. In this scheme, the wavelet transform was applied to obtain the image features. These features were given as inputs to the moving average self-organizing map neural network. This scheme successfully segmented WM, GM and CSF from MR images. The scheme was also suitable for CT and ultrasound images. Nabizadeh and Kubat [49] experimented on Brain tumors detection and segmentation of T1 weighted and fluid-attenuated inversion recovery (FLAIR) MR images using Gabor wavelet and statistical features. Gabor wavelets were used for feature extraction. Statistical features extraction method used gray level co-occurrence matrix, gray level run length matrix, a histogram of oriented gradient and linear binary pattern for extraction of features. Abdullah et al. [117] segmented CSF from brain MR images using the spatial fuzzy clustering method with evolutionary expectation maximization (EM) that was improved using the genetic algorithm. Peng and Varshney [46] experimented on the human visual system (HVS) driven image segmentation algorithm to segment the WM, GM and CSF. HVS properties from region-based and boundary-based methods were encoded by the energy function. To measure the difference between the image contents just-noticeable difference (JND) model was used. Shantakumar and Ganeshkumar [50] segmented two images of MRI using a neuro-fuzzy inference system classifier in which an automatic seed point selection method was employed. This scheme was found to be faster with improved accuracy as compared to other schemes. Madhukumar et al. [51] experimented on fuzzy c-means (FCM) and k-means segmentation algorithms with histogram guided initialization to segment GM, WM and CSF from T1 contrast axial plane MR images of tumor edema

Table 2.6 State of the Art Segmentation Schemes

Author	Year	Methodology	Dataset	Automatic/semi-automatic	Parameters	Comparison with	Contributions
Xie et al. [111]	2005	Hybrid level set method driven by region and boundary information	246 MRI slices of 10 patients.	Semi-automatic	Measurement error, true positives, false positives, false negatives, true negatives, percent matching, correspondence ratio	Manually segmented images	The novel segmentation method is based on a hybrid level set method employing region and boundary information.
Vijaykumar et al. [114]	2007	Wavelet filtered images, FLAIR and T2-W MRI images are fed as features to unsupervised neural networks for segmentation of tumor, edema, CSF, necrosis and normal tissues	10 Apparent diffusion coefficient (ADC) images.	Automatic	Sensitivity and specificity	Manually segmented images	A novel segmentation scheme that employs a mixture of self-organizing map neural network and multi-resolution analysis for segmentation of ADC images. The proposed scheme well segments tumor, edema, CSF and necrosis from ADC images.
Wang et al. [109]	2009	Tumor segmentation using fluid vector flow (FVF)	11 MRI Images, 3 synthetic images of different shapes	Semi-automatic	Tanimoto metric, mean, median, standard-deviation of Tanimoto metric, p value	Gradient vector flow (GVF), boundary vector flow (BVF), magnetostatic active contour (MAC)	This research presents a novel fluid vector flow in image segmentation. The scheme shows improvements in segmentation results compared to GVF, BVF and MAC. FVF captures a large range and extracts concave shapes also.
Zhang et al. [115]	2011	Fusion and classification of multispectral images using support vector machine and region growing for brain tumor segmentation	11 MR images	Automatic	True positive, false positive, true negative, false negative, total error	Support vector machine (SVM), improved level set, neural network.	This scheme proposes a novel feature selection method and region growing to improve the segmentation accuracy and reduce the computation time.

AlZubi et al. [118]	2011	Wavelet, ridgelet and curvelet transform based segmentation	1 CT image, 1 phantom image	Automatic	Accuracy, mean square error, peak signal to noise ratio	K means clustering, iterative thresholding, Markov random field model, wavelet segmentation, curvelet segmentation, ridgelet segmentation	The main contribution is a multi-resolution analysis using wavelet, curvelet and ridgelets along with thresholding as a pre-processing and post-processing step to segment the region of interest. Curvelet based segmentation outperforms the other schemes. Curvelets improve the classification of abnormal tissues and reduce the surrounding noise.
Sachdeva et al. [110]	2012	Content-based active contour model in which intensity and texture information is used to overcome the over-segmentation problem	600 MR images, 5 synthetic images	Semi-automatic	Hausdorff distance, Tanimoto metric	GVF, MAC, FVF, content-based active contour	A novel active contour-based model which well segments homogeneous tumors with a different and similar background. The model is also suitable for the segmentation of complex and irregular shapes.
Torbati et al. [116]	2014	Moving average self-organizing map neural network-based segmentation in which discrete wavelet transform provides features as inputs to the neural network	1 CT image, 10 MRI images of the brain, 30 breast ultrasound images	Automatic	Jaccard index, Tanimoto metric	An incremental supervised neural network, self-organizing map	A modified self-organizing map model that is suitable for the segmentation of WM, GM and CSF from MR images. The scheme is well suited for the segmentation of CT and ultrasound images and is robust to noise.
Shanta Kumar & Ganeshkumar [50]	2015	A neuro-fuzzy inference system that is based on automatic seed point selection is employed in the segmentation of brain tumors	120 MR images for training, 80 images for testing the classifier. Two images are used in segmentati-on.	Automatic	Similarity index, overlap fraction, extra fraction, positive predictive value	Multivariate Bayesian segmentation, Fuzzy connectedness segmentation, the fuzzy classifier with morphological operation based segmentation	The algorithm improves the accuracy rate of segmentation and reduces the segmentation time.

Madhukumar and Santhiya-kumari [51]	2015	K-means and fuzzy c means segmentation using histogram guided initialization	3 MR images	Automatic	Only qualitative analysis is done.	K-means, FCM	In this scheme, a qualitative comparison of k-means and FCM segmentation method is done. K-means identifies six tissue classes whereas fuzzy c means identifies 3 classes.
Nabizadeh and Kubat [49]	2015	Gabor wavelet and statistical features brain tumor detection and segmentation	25 real and simulated MR and FLAIR brain images	Automatic	Sensitivity, specificity, accuracy	SVM-linear, SVM-radial basis function, k-nearest neighbor, nearest subspace classifier -general, nearest subspace classifier - Gaussian, SR, k-means-Euclidean, k-means-city	Gabor wavelet and statistical features are tested using different classifiers. The statistical feature extraction method is superior to Gabor wavelets. No atlas registration, bias correction or prior anatomical knowledge is required.
Maksoud et al. [119]	2015	Integration of k means and Fuzzy c means clustering followed by thresholding and level set segmentation	285 MR images	Automatic	Precision, sensitivity, true positive, true negative	K means, expectation-maximization, fuzzy c means clustering, mean shift clustering	A computationally efficient scheme which improves the segmentation quality and accuracy. The scheme is suitable for removing the noise and other artifacts of images.
Peng and Varshney [46]	2015	Region and boundary-based methods in which HVS properties are encoded as an energy function	1 MRI image, 1 mamogram image, 90 natural images	Automatic	Recall, precision, F-measure	Otsu thresholding, Markov random fields, Markov random fields-radial basis, region-based active contour, level set, active segmentation with fixation, dynamic clustering	The scheme applies just a noticeable difference model to compute the contrast of different objects in a novel way. The region and boundary energy function used in this scheme reduces the risk of being biased while segmenting the objects.

Banerjee et al. [48]	2016	Segmentation using multilevel thresholding. The ROI is segmented using a single seed selection and connected component analysis	160 MRI slices of 25 patients	Semi-automatic	Jac and dice coefficient, accuracy, run time	Manual segmentation, multilevel Otsu, grow cut segmentation.	A very good segmentation scheme which employs discrete curve evolution in multilevel thresholding in a novel manner. In this scheme, a single seed pixel position does not affect final segmentation. The segmented ROI is found to be better than other schemes and the scheme is computationally efficient.
Chitra and Deepa [169]	2019	Di-phase midway convolution and de-convolution network	MRI slices of 80 patients	Automatic	Dice similarity coefficient, sensitivity	K-means, decision forest, FCM, hierarchical classification, latest atlas, generative model.	The proposed scheme obtains higher dice score value as compared to the other schemes
Zhou el al. [170]	2020	Segmentation using deep learning and attention fusion	MRI slices of 285 patients	Automatic	Dice coefficient, Hausdorff distance	V Net, convolutional network, sementic segmentation, 3-D fully connected network .	The scheme is better in terms of segmentation pararmeters. Amount of memory required is less to train the deep network.
Bai et al. [171]	2021	Deep learning based segmentation using ResNeXt-50 U-net	CT scans of 60 patients	Automatic	Dice similarity coefficient	V Net, 3 D UNet, proposed method with 3-D UNet, proposed method with UNet	The proposed scheme outperforms in terms of dice similarity coefficient.

complex. Maksoud et al. [119] merged the k-means clustering algorithm and fuzzy c means technique followed by thresholding and segmentation. Tumors were segmented using level sets theory. Romero et al. [120] experimented on the non-local automatic brain hemisphere segmentation of MR images. The proposed method used a library of pre-labeled brain images in a stereotactic space in combination with a non-local label fusion scheme for segmentation. They used a multi-label block-wise label fusion strategy. AlZubi et al. [118] did segmentation of medical images using wavelet, ridgelet and curvelet transform. Ledig et al. [121] proposed an atlas-based framework for the segmentation of MR brain images. The approach was based on a robust registration, joint label fusion and intensity-based label refinement using expectation maximization (EM). Many authors [169-171] have recently proposed deep learning-based segmentation methods. Chitra and Deepa [169] employed three layers of di-phase midway convolution and de-convolution network to segment MRI slices of 285 patients. The scheme achieves a higher value of dice similarity coefficient as compared to other schemes. Zhou et al. [170] have performed segmentation of MRI images of 285 patients using deep learning and attention fusion. Multi-sequence images are fused using attention mechanism to obtain the higher value of dice coefficient and Hausdorff distance and the proposed method requires less memory to train the deep network. Bai et al. [171] have done deep learning-based segmentation of CT images using ResNeXt-50 U-net. The proposed scheme outperforms in terms of dice similarity coefficient. The deep learning-based methods can achieve higher segmentation accuracy, however, these schemes require higher processing time.

Table 2.6 represents a few states of the art segmentation schemes along with their contributions, compared schemes along with parameters, etc.

2.2 CONCLUSIONS

The schemes utilizing different multi-scale decomposition (MSD) transforms discussed above are compared and the building blocks for the present work are identified. It is observed from the previous researches that the improvement in visual accuracy in the form of better edges, contrast, texture and computational speed is needed to have better clinical investigations. From the literature reported so far it is seen that most of the CT and MR fusion studies are not validated by radiologists. As most of the authors have used a variety of transforms in the past, the presented thesis focuses on three different types of transforms so as to provide readers with a sufficient amount of knowledge. It will be shown in the later chapters of this thesis that the presented work obtains improved visual results and fusion quality assessment parameters such as mutual information, edge information, SF, standard

deviation and mean as compared to many of the aforementioned schemes in the later chapters. The NSCT based hybrid fusion scheme and NSST based fusion schemes presented in later chapters of this thesis are specifically designed to address these gaps in the field of medical image fusion. From the reported literature for the segmentation of brain CT and MRI images it is seen that there are very few trials in the study of segmentation of fused CT and MRI images. Hence, the present thesis attempts to fill the gap in this area.

CHAPTER 3

METHODOLOGY

3.1 INTRODUCTION

The research methodology is defined to meet the research objectives defined in Chapter 1 which focuses mainly on pre-processing, fusion and clustering of the CT and MRI images. Though MR images provide sufficient details of soft tissues of the brain, however, these images lack in bone and calcification information. Other imaging alternatives such as CT scans give bone, calcification and air details which the MR images lack in. The present methodology deals with the development of fusion schemes which generate a composite image carrying all the aforementioned details in a single image. The composite image so obtained is used to find a solution to the clustering of intensity inhomogeneity of MRI into two different classes. Further, the capability of the fused information in aiding the clustering schemes in the separation of tumor from edema is also demonstrated. This research focuses on assisting the neuro-radiologists and surgeons in the decision-making process using an automatic system for the identification of disease orientation with respect to the bone. The block diagram of the designed methodology is shown in Figure 3.1. The stepwise description of the methodology is explained in the following sections.

3.2 ACQUISITION OF DATA

The very initial phase of this research work is the collection of the required image dataset. The acquisition of data from the Postgraduate Institute of Medical Education and Research (PGIMER) is obtained as a memorandum of understanding between PGIMER and Thapar Institute of Engineering and Technology. The radiologist's co-operation and time involvement helped in the design of research objectives, data collection and results verification. Special attention is given to maintain the level of dignity and confidence in the patient's personal information. To achieve this objective the patient's details are anonymized and the consent of the patients is taken before the data acquisition.

3.2.1 CT and MRI Image Acquisition and Evaluation Criteria for PGIMER Dataset

Subjects are the patients who had undergone medical scanning at the Department of Radio-diagnosis and Imaging, PGIMER, Chandigarh, India during the period from July 2015 to July 2018. The consent of the patients for using their images for research purposes was taken prior to image scanning as a general protocol of the institute. The collected images are either normal or diseased tissues. The diseases on these images were assessed by the expert

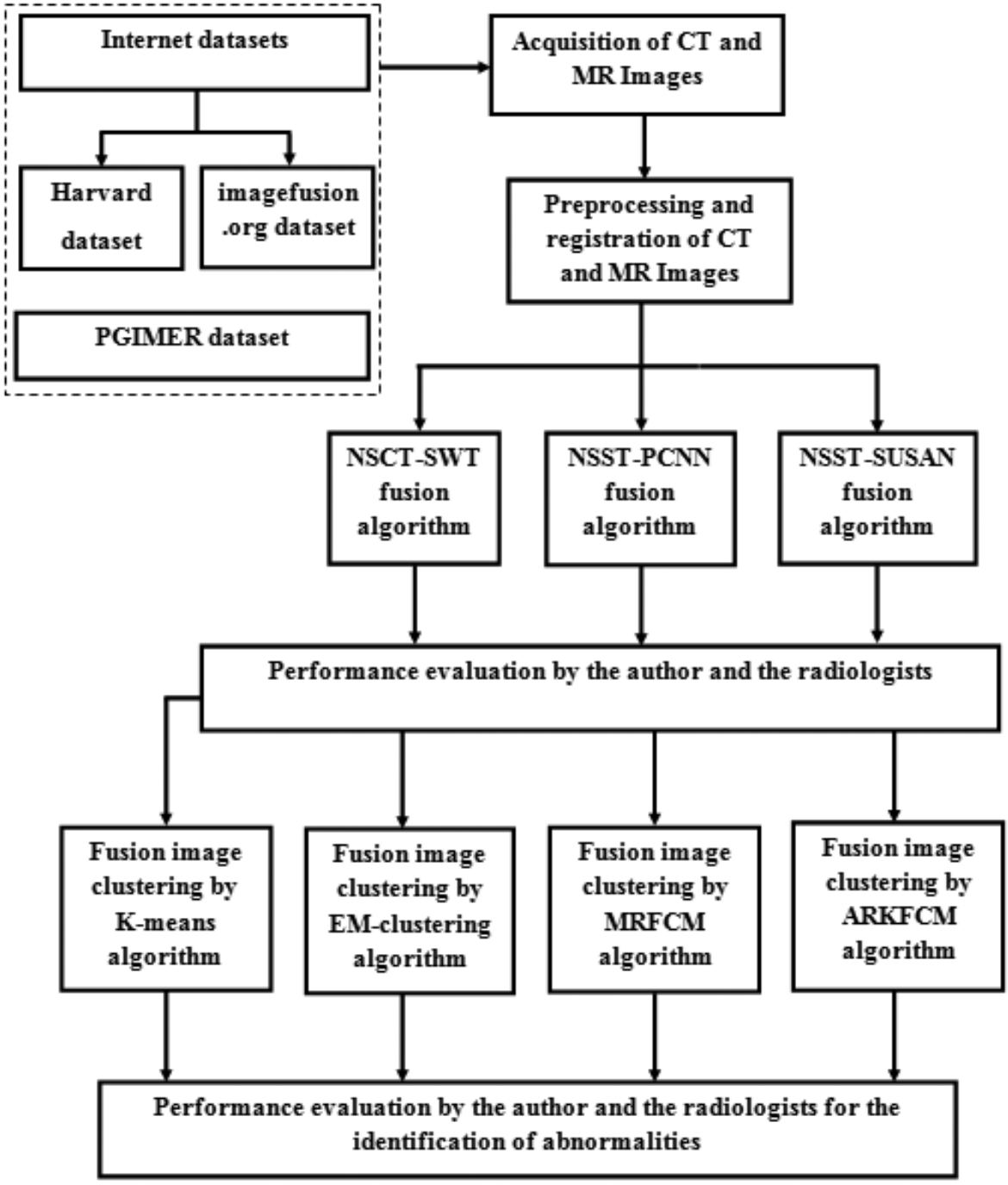

Figure 3.1 Research methodology used in the detection of abnormalities using CT and MR images

neuro-radiologists. The criteria followed by the experts in the assessment of abnormality is mentioned as follows:

(i) The abnormalities are assessed by visual interpretation of the expert neuro-radiologists based on their knowledge and experience in this field.

(ii) The diseases are assessed by the clinical history, follow up and other related observations.

(iii) Histopathology evaluation and correlation is done by experts wherever available.

(iv) The abnormalities are advocated by biopsy/pathology/CT/MRI evaluations.

3.2.2 Dataset Sources and Details

The images used in the proposed methodology are acquired from two different sources. These datasets are used for the validation and testing of the developed methods. The details of different datasets are given as follows:

1) Postgraduate Institute of Medical Education and Research (PGIMER) dataset

A real-time dataset consisting of 40 image pairs of five different patients is collected from PGIMER, Chandigarh, India. This dataset contains 32 image pairs of CT and T2-W MRI, 07 image pairs of CT and T1-W MRI, 01 image pair of CT and Gadolinium-enhanced T1-W MR images. PGIMER dataset acquisition protocol and details of CT and MR images are shown in Table 3.1.

Table 3.1 PGIMER Dataset Acquisition Protocol and Details of CT and MR Images

MRI acquisition protocol: Orientation: Axial Resolution: 512×512 Slice Thickness: 5 mm Slice Gap: 1.5 mm		**CT acquisition protocol:** Orientation: Axial Resolution: 512×512 Slice Thickness: 5 mm Slice Gap: 0 mm		
Disease type		Tumor	Stroke	Fungal infection
Number of patients (2-13 slices per patient)		3	1	1
Details of abnormality	Calcified tumor (2 slices of T2-W MRI, 2 slices of T1-W MRI, 5 slices of CT)	1		
	Glioma (different grade) (2 slices of T2-W MRI, 4 slices of T1-W MRI, 5 slices of CT)	1		
	Postoperative tumor (1 slice of T2-W MRI, 1 slice of T1-W MRI, 1 slice of Gadolinium-enhanced T1-W MRI, 3 slices of CT)	1		
	Stroke (10 slices of T2-W MRI, 10 slices of CT)		1	
	Fungal infection (11 slices of T2-W MRI, 11 slices of CT)			1
	Normal slices (6 slices of T2-W MRI, 6 slices of CT)			

2) Internet datasets

The benchmark dataset consisting of 09 image pairs of CT and T2-W MRI is collected from Harvard medical school website [122]. Table 3.2 shows the Harvard medical school dataset acquisition protocol and details of CT and MR images. Another benchmark CT and T1-W MRI pair is collected from the www.imagefusion.org website.

Table 3.2 Harvard Medical School Dataset Acquisition Protocol and Details of CT and MR Images

MRI acquisition protocol: Orientation: Axial Resolution: 256×256 Slice Thickness: 5 mm			**CT acquisition protocol:** Orientation: Axial Resolution: 256×256 Slice Thickness: 5 mm		
Disease type		Stroke	Tumor	Infectious disease	Hypertensive disease
Number of patients (a T2-W MRI and a CT slice per patient)		4	3	1	1
Details of abnormality	Acute stroke: writes but cannot read	1			
	Acute stroke: speech arrest	1			
	Metastatic bronchogenic carcinoma		1		
	Sarcoma		1		
	Hypertensive encephalopathy				1
	Meningioma		1		
	Multiple embolic infarctions	1			
	Fatal stroke	1			
	Cerebral toxoplasmosis			1	

The role and importance of fusion in the context of diseases considered here is mentioned as follows:

In cases of tumor patients fusion helps in separating the boundary between tumor and edema. The relationship of tumor/edema w.r.t. bone can also be identified.

In stroke patients, the distinction between hemorrhage and surrounding tissues can be better identified.

In hypertensive diseases, the subcortical white matter lesions relationship with the overlying bones can be identified.

In infectious diseases, the fused image demonstrates the lesion, its affect on the surrounding brain parenchyma and the overlying bony details.

3.3 PREPROCESSING OF THE DATASETS

Spatial misalignments were existing between the CT and MRI images hence, registration was required before fusion. An affine transformation based registration algorithm was employed which is an intensity-based multimodal image registration method. Details of this

method are given in section 4.2.1 of Chapter 4. All three datasets were registered using the toolkit of MATLAB and image processing software [167].

3.4 DATASETS USED IN THE DEVELOPED METHODS

To meet the research objectives four different studies are done. The first study is an NSST based scheme that employs a pulse coupled neural network motivated by the morphological gradient of HF sub-bands based fusion rule. This study employs 9 image pairs of CT and T2-W MRI of the Harvard dataset and 8 pairs of CT and T2-W MRI of the PGIMER dataset.

In the second study, an NSCT-SWT based hybrid fusion scheme is developed. In this study 9 image pairs of CT and T2-W MRI obtained from the Harvard school website and a pair of CT and T1-W MRI obtained from www.imagefusion.org, are utilized. The primary (PGIMER) dataset of this study contains 20 image pairs of CT and T2-W MRI and 8 pairs of CT and T1-W MRI.

The third study is an NSST based fusion scheme that employs a human visual system motivated operator called smallest uni-value segment assimilating nucleus (SUSAN). This study employs 09 image pairs of Harvard school dataset and 15 pairs of CT and T2-W MR images of PGIMER dataset.

The fused images of all these schemes are analyzed and NSCT-SWT based fusion images are found to be more suitable for clustering.

The fourth study employs 4 clustering schemes named k-means, expectation-maximization (EM) clustering, morphological reconstruction based FCM (MRFCM) clustering and adaptively regularized kernel-based FCM (ARKFCM) clustering in the detection of abnormalities. This study employs 09 fused images of the Harvard dataset and 07 fused images of the PGIMER dataset.

The performance of the developed methods is evaluated by the author and the radiologists. The two types of criterion are selected for the evaluation of the developed methods (i) visual analysis (ii) parametric analysis

3.5 EVALUATION CRITERIA

The proposed algorithms are evaluated by qualitative and parametric means explained as follows:

3.5.1 Qualitative Analysis - Visual Interpretation

Visual quality analysis of the fused images is done by the author and two expert radiologists. Visual evaluation of the fused image is done by considering the ability of the fused image to keep the bone and parenchymal information of CT and MR image,

respectively. The ability of the fused image to retain the local structural information, contrast, brightness, texture and edge details of different image features of source images is observed. The images are shown to two expert radiologists independently to validate the visual performance of the proposed algorithms. Visual evaluation of clustered fusion images is done in terms of their ability to retain the contrast, brightness, overall shape and boundary of the abnormality as well as surrounding tissues. Visual evaluation of clustered fusion images is also done by comparing these with clustered MR images.

3.5.2 Quantitative Analysis - Parametric Evaluation

The experiments are qualitatively evaluated using the following parameters

Mutual Information (MI): It computes the amount of source images information in the fused image [38]. MI between input images A, B and fusion image F is computed as:

$$MI(F,A) = \sum_{x=1}^{L}\sum_{y=1}^{L} h_{x,y}^{F,A} \log_2 \frac{h_{x,y}^{F,A}}{h_{x,y}^{F} h_{x,y}^{A}} \tag{3.1}$$

where, $MI(F,A)$ and $h_{x,y}^{F,A}$ are the MI and normalized joint grey level histogram of image A and F at location x, y, respectively [123]. $h_{x,y}^{A}$ and $h_{x,y}^{F}$ are the gray-level histograms of image A and F, respectively. L stands for the number of intensity levels. Similarly, the mutual information $MI(F,B)$ between image B and fusion outcome F is computed as:

$$MI(F,B) = \sum_{x=1}^{L}\sum_{y=1}^{L} h_{x,y}^{F,B} \log_2 \frac{h_{x,y}^{F,B}}{h_{x,y}^{F} h_{x,y}^{B}} \tag{3.2}$$

Using eqn.3.1 and eqn.3.2 the MI metric is expressed as

$$MI(F,A,B) = MI(F,A) + MI(F,B) \tag{3.3}$$

A larger MI indicates better source texture in the fusion image.

Standard Deviation (SD): The standard deviation represents the amount of contrast present in an image [94, 103]. A higher contrast image gives a higher standard deviation. Mathematically it is defined as:

$$SD = \sqrt{\sum_{x=1}^{p}\sum_{y=1}^{q} \frac{\left(I(x,y) - \frac{1}{p\times q}\sum_{x=1}^{p}\sum_{y=1}^{q} I(x,y) \right)^2}{p\times q}} \tag{3.4}$$

Edge information-based quality metric ($Q^{AB/F}$): This parameter indicates the edge information transportation from original images to the fused image [124]. It uses a Sobel edge operator to compute the strength and orientation details of each pixel in the input

images A, B and the fused image F. Initially the output responses of the Sobel edge template for a pixel at the location (x,y) are computed in the horizontal and vertical direction. Thereafter, these responses are convolved with the grey value of that pixel to generate the convolved output $S_A^H(x,y)$ and $S_A^V(x,y)$, respectively in the horizontal and vertical direction. The edge strength $G_A(x,y)$ and edge direction $\alpha_A(x,y)$ for image A at that location are computed as follows:

$$G_A(x,y)=\sqrt{S_A^H(x,y)^2+S_A^V(x,y)^2} \tag{3.5}$$

$$\alpha_A(x,y)=\tan^{-1}\left(\frac{S_A^V(x,y)}{S_A^H(x,y)}\right) \tag{3.6}$$

The relative edge strength $G_{AF}(x,y)$ and relative direction $\alpha_{AF}(x,y)$ between image A and fused image F are computed as:

$$G_{AF}(x,y)=\begin{cases}\dfrac{G_F(x,y)}{G_A(x,y)}, & \text{if} \quad G_A(x,y)>G_F(x,y)\\ \dfrac{G_A(x,y)}{G_F(x,y)}, & \text{otherwise}\end{cases} \tag{3.7}$$

$$\alpha_{AF}(x,y)=\frac{\left|\left|\alpha_A(x,y)-\alpha_F(x,y)\right|-\dfrac{\pi}{2}\right|}{\pi/2} \tag{3.8}$$

The preservation values $P_{AF}^g(x,y)$ and $P_{AF}^\alpha(x,y)$ are computed from $G_{AF}(x,y)$ and $\alpha_{AF}(x,y)$ as follows:

$$P_{AF}^g(x,y)=\frac{\Gamma_g}{1+e^{k_g(G_{AF}(x,y)-\sigma_g)}} \tag{3.9}$$

$$P_{AF}^\alpha(x,y)=\frac{\Gamma_\alpha}{1+e^{k_\alpha(\alpha_{AF}(x,y)-\sigma_\alpha)}} \tag{3.10}$$

The constants Γ, k and σ in eqn.3.9 and eqn.3.10 are related to the exact shape of sigmoid signals used to compute the preservation values [124].

The edge strength preservation is computed as:

$$Q^{AF}(x,y)=P_{AF}^g(x,y)P_{AF}^\alpha(x,y) \tag{3.11}$$

In a similar way, $Q^{BF}(x,y)$ is also computed.

The mathematical expression for $Q^{AB/F}$ is given as:

$$Q^{AB/F} = \frac{\sum_{x=1}^{p}\sum_{y=1}^{q} Q^{AF}(x,y)w^{A}(x,y) + Q^{BF}(x,y)w^{B}(x,y)}{\sum_{x=1}^{p}\sum_{y=1}^{q}[w^{A}(x,y) + w^{B}(x,y)]} \quad (3.12)$$

where, w is the weight. The value of $Q^{AB/F}$ close to 1 indicates good fusion quality [45].

Spatial Frequency (SF): It is responsible for the overall activity level and clarity in the image. Larger spatial frequency value indicates better fusion quality [45, 103]. Mathematically SF for an image A can be expressed as:

$$SF = \sqrt{RF^2 + CF^2} \quad (3.13)$$

where, RF stands for row frequency and CF indicates column frequency of an image I of size p×q.

$$RF = \sqrt{\frac{1}{p \times q}\sum_{x=1}^{p}\sum_{y=2}^{q}[I(x,y) - I(x,y-1)]^2} \quad (3.14)$$

$$CF = \sqrt{\frac{1}{p \times q}\sum_{x=2}^{p}\sum_{y=1}^{q}[I(x,y) - I(x-1,y)]^2} \quad (3.15)$$

Mean: It signifies the amount of mean brightness present in an image. The mean of an image of size p×q is given as:

$$Mean = \frac{1}{p \times q}\sum_{x=1}^{p}\sum_{y=1}^{q} I(x,y) \quad (3.16)$$

where, I(x,y) denotes the intensity value of an image at coordinates x and y.

Parametric analysis of the clustering schemes is done using the partition coefficient as a performance parameter. The details of this parameter are explained briefly as follows:

The partition coefficient (C_p) is a measure of extent of overlapping between different clusters [125]. A higher value of this coefficient indicates a small overlapping among the clusters [126]. Its value ranges between 0 and 1. The value equal to 0 indicates no clustering structure in the data and a value equal to 1 indicates good clustering. It is expressed as:

$$C_p = \frac{\sum_{m=1}^{C}\sum_{n=1}^{N} Z_{mn}^2}{N} \quad (3.17)$$

where, Z_{mn} indicates membership of data element n in cluster m, c represents the total number of clusters and N represents the total number of data points in the image.

3.6 CONCLUSIONS

This chapter described the methodology followed to accomplish the research objectives of this thesis. The detailed description of the datasets used in different experiments has been

discussed. The method of visual and parametric evaluation of fusion as well as clustering schemes have been discussed. All the design steps of the proposed fusion and clustering methods used in the detection of abnormalities are presented in detail in the subsequent chapters.

CHAPTER 4

FUSION SCHEME USING NSST AND PCNN INCORPORATED WITH MORPHOLOGICAL GRADIENT

4.1 INTRODUCTION

Rapid technological development in imaging technology has helped humans in representing visual information of different parts of the human body [77]. Presently, radiologists are advising multimodal imaging to identify the diseased tissues of a particular organ as none of the single modality is sufficient in conveying the complete information of a tissue or organ [77, 94]. The researchers in the past have worked on fusion rules based on approaches such as saliency measures with various transforms, neural network and fuzzy logic [2, 31, 83]. DWT based fusion schemes with average, maximum selection and PCA based fusion rules are already discussed in section 2.1 [40, 75]. However, these schemes suffer from poor edge details, clarity and limited directionality. NSST and PCNN based fusion schemes with various activity measures such as region energy, normalized sum modified Laplacian, gradient, variance and modified SF are employed in existing researches [94, 96, 127]. Normalized coefficients of NSCT and normalized coefficients of NSST are fed as an external stimulus to PCNN in [43, 95, 98]. Positive and negative coefficients in detail sub-bands of NSST represent the edges and contours details from different angles [95]. Hence, normalizing these coefficients degrades the quality of fusion. Moreover, most of the saliency measures used with PCNN based fusion rules increase the computational time of the fusion algorithms. These points are considered in the present research. The present research proposes a new fusion scheme using NSST and PCNN. In the proposed methodology, the low-frequency sub-bands are fused using regional energy (RE)-based activity and high-frequency coefficients are fused using a novel morphological gradient-based PCNN fusion rule. The proposed morphological gradient-based method is compared with five state-of-the-art fusion schemes. It is observed that the present fusion method improves the fusion outcome and is faster than other PCNN-based fusion schemes.

4.2 METHODOLOGY

This section contains a step-wise description of the proposed methodology. It includes image pre-processing (registration) as shown in Figure 4.1, NSST decomposition process as shown in Figure 4.2, approximation sub-band fusion, high frequency (HF) sub-band fusion

and image reconstruction. The block diagram of the proposed fusion methodology is shown in Figure 4.4.

4.2.1 Image Pre-Processing

The main issue in image registration is to find the parameters of a spatial transform to co-align the two images. In the present research, CT and MR images are aligned into a common coordinate system so that information from the same physical structures is fused together [40]. Image registration is an important pre-processing step before fusing two images to obtain their integrated output. The registration of real-time PGIMER dataset and internet dataset of CT and MRI images is done using an automatic alignment technique of MATLAB and the Image Processing Toolbox [167]. The toolbox is composed of an intensity-based multimodal image registration in which three number of Gaussian pyramid levels are selected. The affine transformation is utilized which is expressed as follows:

$$x' = a_1 x + b_1 y + c_1 \quad (4.1)$$

$$y' = a_2 x + b_2 y + c_2 \quad (4.2)$$

In matrix form, it is expressed as:

$$\begin{bmatrix} x' \\ y' \\ 1 \end{bmatrix} = \begin{bmatrix} a_1 & b_1 & c_1 \\ a_2 & b_2 & c_2 \\ 0 & 0 & 1 \end{bmatrix} \begin{bmatrix} x \\ y \\ 1 \end{bmatrix} \quad (4.3)$$

where, x, y is input pixel coordinates and x', y' are the transformed pixel co-ordinates. a, b, c represents the affine transformation parameters [128]. Initially, the multistage decomposition of images to be registered is done using the Gaussian pyramid and the control points in the reference and target image are specified. These points are then fine-tuned using one plus one evolutionary optimizer to avoid the possibility of any local maxima [130]. Mutual information is used as a similarity criterion of optimization of these points. The affine transform parameters are computed after the optimization of control points. The B-spline function is used as an interpolation method to find the new coordinates of the image to be registered and hence, the points of the target image are mapped onto the reference image [129]. The registration output of MATLAB and the Image Processing Toolbox for three pairs of PGIMER images is shown in Figure 4.1.

4.2.2 Non-Subsampled Shearlet Transform Decomposition

Non-subsampled shearlet transform (NSST) belongs to the family of affine transforms which preserves lines and parallelism. However, these can also be used to preserve the distances and angles. Using affine transform translation, scaling and shearing operations can

be performed on images and these transforms have six degrees of freedom. NSST utilizes the non-subsampled Laplacian pyramid (NSLP) to decompose the source image into different scales [131]. The low pass-band image at a scale (d = 1) is applied to NSLP to produce the next scale (d = 2) as shown in Figure 4.2. The shearing filters (ShF) are used to decompose the high pass-band image at a particular scale into different directional sub-bands [132]. Mathematically, the two-dimensional affine system of shearlets can be represented as follows:

$$F_{AS}(\psi) = \{\psi_{j,d,k}(x) = |detA|^{j/2}\, \psi(S^d A^j x - k) : d, j \in Z, k \in Z^2\} \quad (4.4)$$

where, A symbolizes the anisotropic matrix, S indicates the shear matrix and j, d, k are scale, direction and shift parameters, respectively. The anisotropic dilation matrix A can be written as given below in eqn.4.5 or eqn.4.6 as follows:

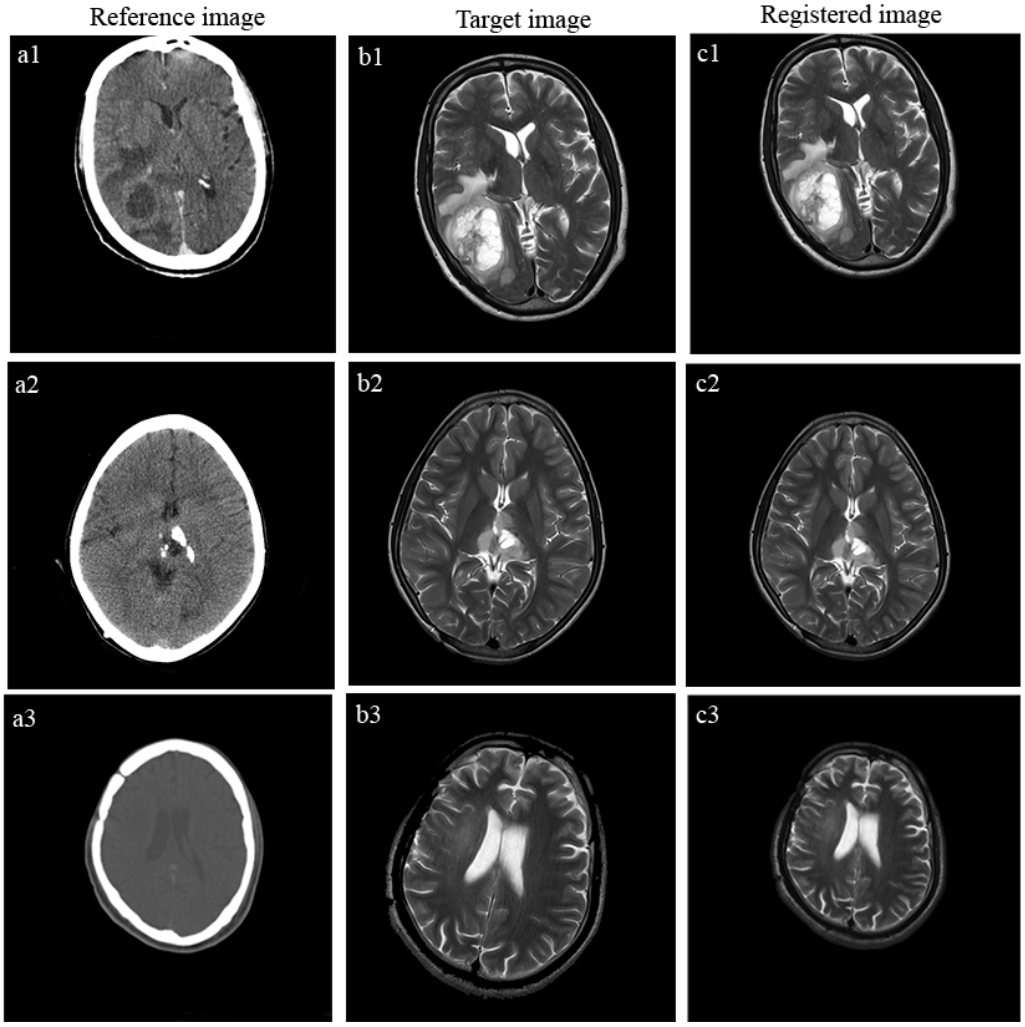

Figure 4.1 Registration of three pairs of PGIMER dataset

(a1, a2, a3) Reference image (CT image)
(b1, b2, b3) Target image (MR image)
(c1, c2, c3) Registered image

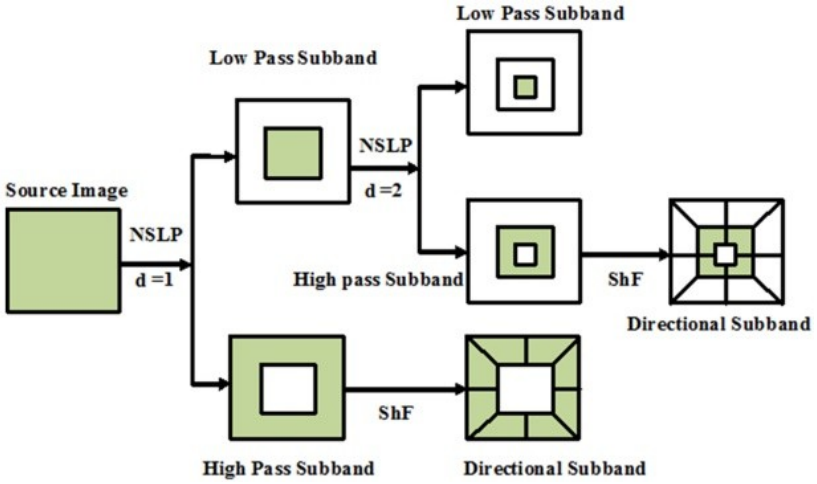

Figure 4.2 Two-level decomposition process of the non-subsampled shearlet transform

$$A = \begin{bmatrix} a & 0 \\ 0 & \sqrt{a} \end{bmatrix} \tag{4.5}$$

$$A = \begin{bmatrix} \sqrt{a} & 0 \\ 0 & a \end{bmatrix} \tag{4.6}$$

where, $a > 0$ controls the scale of shearlets. The role of the anisotropic matrix is to provide parabolic scaling (resolution) operations on the shearlet. Anisotropic property of this matrix enhances the texture quality of the regions which are far away and at steep angle w.r.t. the point of view of the imaging sensor.

The shear matrix S can be represented either by eqn.4.7 or eqn.4.8 as below:

$$S = \begin{bmatrix} 1 & s \\ 0 & 1 \end{bmatrix} \tag{4.7}$$

$$S = \begin{bmatrix} 1 & 0 \\ s & 1 \end{bmatrix} \tag{4.8}$$

Shear matrix controls the orientation of shearlets which provides the various tilting operations by varying the parameter s, (s=1,2,3,4,5,6,7,8 as so on). The shearlet function is expressed as follows:

$$\psi^{(0)}_{j,d,k}(x) = 2^{j3/2}\, \psi^{(0)}(S^d_0\, A^j_0\, x - m)$$
$$\text{where, } j \geq 0,\ -2^j \leq d \leq 2^j - 1,\ m \in Z^2 \tag{4.9}$$

Each shearlet element has a trapezoid shape enclosed in a box of size $2^{2j} \times 2^j$ (approximately) which are situated along lines of slope $m2^{-j}$, where m is an integer [34] and is shown in Figure 4.3.

The source images A and B are decomposed using NSST into one approximation sub-band A_{Low} , B_{Low}, respectively and a sequence of detailed sub-bands $A_{High}^{d,k}$, $B_{High}^{d,k}$, respectively. The images are decomposed up to scale d = 3 and directions k = 4, 8, 8 from coarser to finer scale using repeated experiments.

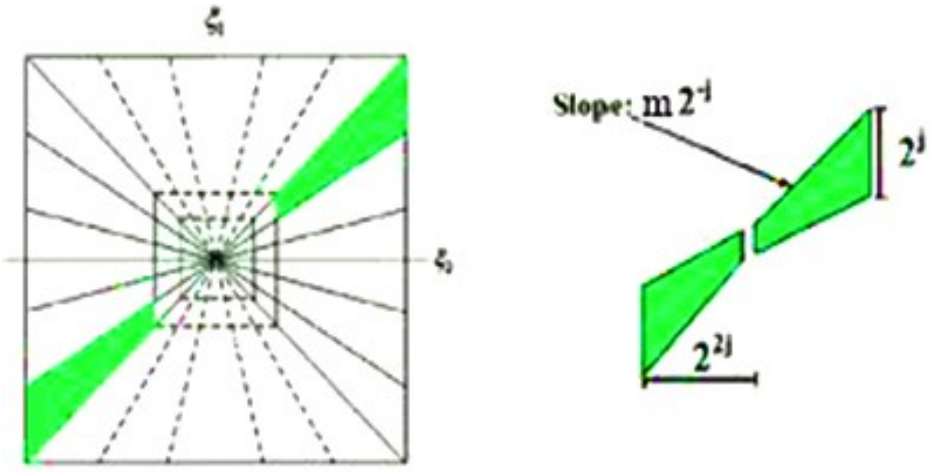

(a) (b)

Figure 4.3 Frequency tiling and support size of shearlets

(a) Frequency tiling

(b) Frequency support size

4.2.3 Approximation Sub-Band Fusion

The low frequency (LF) sub-band contains most of the signal energy [88] and overall envelop (outline) of the image, hence regional energy is selected as an activity measure to fuse LF sub-band. It is observed experimentally that the shape of the Gaussian mask used with the RE improves the attributes such as contrast and local structural details of the fused image. The RE feature is defined as:

$$RE[Z_{Low}(m,n)] = \sum_{i=-1}^{1}\sum_{j=-1}^{1} W \times |Z_{Low}(m+i,n+j)|^2 \tag{4.10}$$

where Z_{Low} represents either A_{Low} or B_{Low}. The weight matrix W [94] performs Gaussian smoothing and is given as follows:

$$W = \begin{bmatrix} 1/15 & 2/15 & 1/15 \\ 2/15 & 3/15 & 2/15 \\ 1/15 & 2/15 & 1/15 \end{bmatrix} \tag{4.11}$$

The Gaussian mask W used with the RE based rule is responsible for improving the contrast. The RE is used to compute the initial fusion decision map according to the following equation:

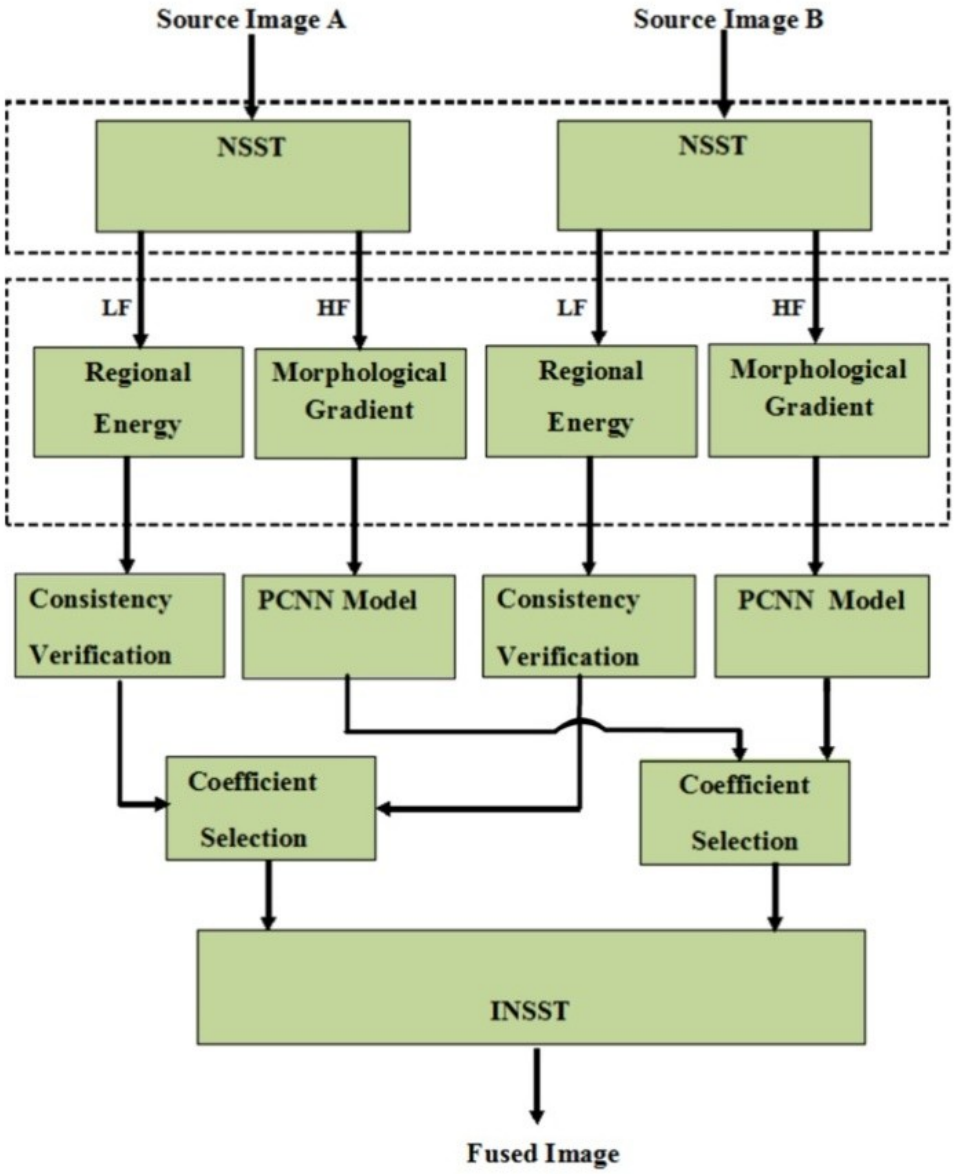

Figure 4.4 Block diagram representation of the proposed methodology

$$map_i(m,n)=\begin{cases}1, & \text{if} \quad RE[A_{Low}(m,n)] \geq RE[B_{Low}(m,n)] \\ 0, & \text{if} \quad RE[A_{Low}(m,n)] < RE[B_{Low}(m,n)]\end{cases} \tag{4.12}$$

Hence, if the RE of a LF coefficient of image A is more than RE of LF coefficient of image B then coefficient A contributes in the fusion and vice versa. This step ensures that the coefficient with high regional energy contributes in the fusion. This operation is followed by consistency verification using a majority filter of window (W) size 3×3. The majority

filter replaces the current coefficient of $map_i(m,n)$ by 1 if no. of one's in the 3×3 size window are greater than or equal to 5 [133]. This means if the majority of coefficients in this window are from image A and the central coefficient is from B then the central pixel is also derived from A. This operation reduces the effect of noise and makes the fused image more homogeneous [45]. The fusion decision map obtained after consistency verification is expressed as follows:

$$map_f(m,n)=\begin{cases} 1, & \text{if } \sum_w[map_i(m,n),W] \geq 5 \\ 0, & \text{Otherwise} \end{cases} \tag{4.13}$$

The fused LF sub-band coefficients are obtained from this decision map as follows:

$$F_{Low}(m,n)=\begin{cases} A_{Low}(m,n), & \text{if } map_f(m,n)=1 \\ B_{Low}(m,n), & \text{if } map_f(m,n)=0 \end{cases} \tag{4.14}$$

4.2.4 HF Sub-Band Fusion

The HF sub-bands contain detailed edge information of the source images hence morphological gradient-based activity measure is proposed in the present paper to fuse these sub-bands of NSST decomposition. The authors in [134] have mentioned the use of morphological gradient as an edge extraction tool however, to the author's best knowledge the suitability of morphological gradient with NSST and PCNN in image fusion is underexplored. Morphological gradient tends to depend less on edge directionality. For example, if the Sobel operator is used, the intensity gradient is computed in horizontal, vertical and other directions separately. As per the knowledge of the author, the standard intensity gradient using NSST has been already implemented in the past. Therefore, in this thesis morphological gradient with NSST has been tested and implemented as it provided better results. Morphological gradient uses two basic morphological operators called greyscale dilation and erosion. Mathematically the morphological gradient (MG) of detail sub-bands $A_{High}^{d,k}$ and $B_{High}^{d,k}$ of source images A and B is expressed as follows:

$$MG\left(Z_{High}^{d,k}\right)=\left(Z_{High}^{d,k}\oplus B_s\right)-\left(Z_{High}^{d,k}\ominus B_s\right) \tag{4.15}$$

where, $Z_{High}^{d,k}$ indicates $A_{High}^{d,k}$ or $B_{High}^{d,k}$ i.e. detailed sub-bands of image A and image B, respectively and B_s is the structuring element matrix as given below:

$$B_s=\begin{bmatrix} 1 & 1 & 1 & 1 & 1 \\ 1 & 1 & 1 & 1 & 1 \\ 1 & 1 & 1 & 1 & 1 \\ 1 & 1 & 1 & 1 & 1 \\ 1 & 1 & 1 & 1 & 1 \end{bmatrix} \tag{4.16}$$

This 5×5 square structuring element extracts the lines, edges and corners in the high-frequency sub-bands in a better way as compared to 3×3 or 7×7 matrix. The morphological gradient value along the edge regions of an image is large and its value along smooth regions is small. Therefore, the morphological gradient is applied as a feeding input to the PCNN. The details of the PCNN model used in the present research are explained as follows:

4.2.5 Pulse Coupled Neural Network

Pulse coupled neural network (PCNN) is a biologically inspired neural network model based on the visual cortical model of small mammals. It is a single layer, a two-dimensional feedback network in which each neuron corresponds to a pixel of an image [94]. Each neuron in the PCNN model is composed of three fields: receptive field, modulation field and pulse generator as shown in Figure 4.5 [89]. The receptive field receives its excitation either from an external source or from the neighboring neurons and is categorized into two subfields: feeding ($F_{i,j}$) field and linking ($L_{i,j}$) field [89]. The input $F_{i,j}$ consists of a field made of surrounding neurons whereas, the secondary field $L_{i,j}$ consists of lateral connections of surrounding neurons. The difference between $F_{i,j}$ and $L_{i,j}$ is that $F_{i,j}$ has slower time decay constant [92]. These subfields are described by eqn.4.17 and eqn.4.18.

$$F_{i,j}[n] = S_{i,j} + e^{-\alpha_F} F_{i,j}[n-1] + V_F \sum_{k=-1}^{1} \sum_{l=-1}^{1} M_{i,j,k,l} Y_{ijkl}[n-1] \tag{4.17}$$

$$L_{i,j}[n] = e^{-\alpha_L} L_{i,j}[n-1] + V_L \sum_{k=-1}^{1} \sum_{l=-1}^{1} W_{i,j,k,l} Y_{ijkl}[n-1] \tag{4.18}$$

where, $S_{i,j}$ is the external input to the neuron and $Y_{ijkl}[n-1]$ is the output from surrounding neurons which is fed to the center neuron. α_F, α_L are the time decay constants and V_F, V_L are magnifying constants associated with feeding and linking inputs, respectively. M and W are synaptic weight matrices [95] expressed by eqn.4.19. These matrices perform like a bridge to transfer the output of the surrounding neurons into the central neuron.

$$M_{i,j,k,l} = W_{i,j,k,l} = \begin{bmatrix} 0.707 & 1.000 & 0.707 \\ 1.000 & 0 & 1.000 \\ 0.707 & 1.000 & 0.707 \end{bmatrix} \tag{4.19}$$

The output of the modulation field ($U_{i,j}$) is described by eqn.4.20 as follows:

$$U_{i,j}[n] = F_{i,j}[n]\left(1 + \beta L_{i,j}[n]\right) \tag{4.20}$$

where, β is the linking strength. The pulse generator compares the output of the modulation field with the internal threshold $\theta_{i,j}[n]$ of the neuron and outputs a pulse $Y_{i,j}[n]$ when $U_{i,j}[n]$

is greater than or equal to $\theta_{i,j}[n]$ otherwise, it goes off. Eqn.4.21 represents the internal threshold of a neuron.

$$\theta_{i,j}[n] = e^{-\alpha_\theta}\theta_{i,j}[n-1] + V_\theta Y_{i,j}[n-1] \tag{4.21}$$

where, α_θ is the threshold decay constant and V_θ is the threshold magnifying constant. The output pulse criterion is represented by eqn.4.22 as follows:

$$Y_{i,j}[n] = \begin{cases} 1 & \text{if} \quad U_{i,j}[n] \geq \theta_{i,j}[n] \\ 0, & \text{Otherwise} \end{cases} \tag{4.22}$$

The time matrix which holds the number of firing instances (pulses) of each neuron is expressed by eqn.4.23. The present work uses this information as the output of PCNN.

$$T_{i,j}[n] = T_{i,j}[n-1] + Y_{i,j}[n] \tag{4.23}$$

The subscripts i, j in the above expressions indicate the position of neuron and n represents the current iteration. The value of n varies from 1 to 200 as is done in [90, 93, 94]. The value of parameters of PCNN is set heuristically as $\alpha_L = 0.3, \alpha_\theta = 0.06, \beta = 0.3, V_L = 1, V_\theta = 20$ using repeated experiments.

In the proposed fusion method, the feeding input contains only the image gray values computed using the morphological gradient and has no dependency on neighbor pixels and exponential decay characteristics. This is done to decrease the complexity of the PCNN network and to increase the computing speed. The morphological gradient of each detail sub-band is fed as an external stimulus to PCNN. This is expressed in eqn.4.24 as follows:

$$F_{i,j}^{Z}[n] = MG\left(Z_{High}^{d,k}\right) \tag{4.24}$$

where, MG stands for the morphological gradient of the image. The linking field, modulation field and internal threshold are computed according to eqn.4.18, eqn.4.20 and eqn.4.21, respectively. The pulse of neurons is generated according to eqn.4.22. The switch on (firing) time of each neuron in n iterations is evaluated using eqn.4.23. The iteration stops on reaching the maximum iteration count. Fused HF sub-image of d^{th} scale and k^{th} direction is obtained according to the maximum coefficient selection rule expressed by eqn.4.25 as follows:

$$F_{High}^{d,k}(m,n) = \begin{cases} A_{High}^{d,k}(m,n), & \text{if } TA(m,n) \geq TB(m,n) \\ B_{High}^{d,k}(m,n), & \text{if } TA(m,n) < TB(m,n) \end{cases} \tag{4.25}$$

where, TA and TB are the number of firing times of neurons of image A and image B, respectively. According to this rule the pixel which fires its associated neuron more number of times contributes in the fused image. Finally, inverse NSST is performed on the fused

low pass and high pass sub-band images to reconstruct the final fused image. This is expressed in eqn.4.26 as follows:

$$F = \mathrm{NSST}^{-1}\left(F_{\mathrm{Low}}, F_{\mathrm{High}}^{d,k}\right) \quad (4.26)$$

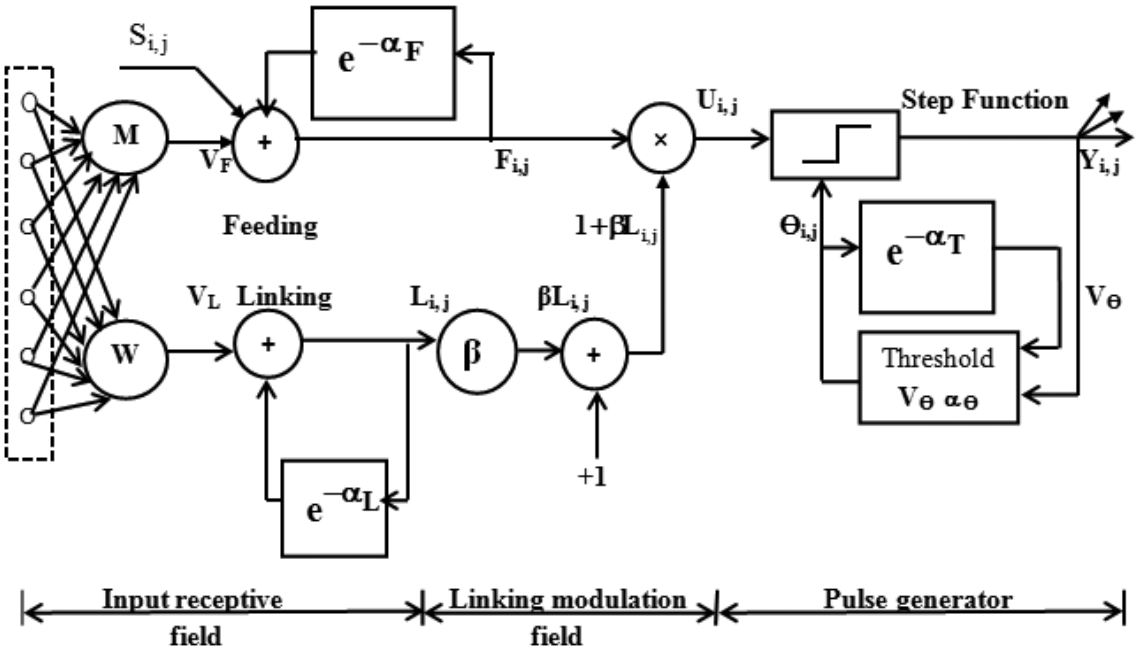

Figure 4.5 Pulse coupled neural network model

4.3 EXPERIMENTAL SETUP

The proposed method is implemented in Matlab R2015a, using Intel core i5 computer having 8 GB RAM. The proposed methodology is compared with five states of the art fusion schemes as follows: DWT based scheme with one level of decomposition employing bior4.4 filter and avg./max. fusion rules as proposed in [135], SWT based scheme with one decomposition level employing rbio1.3 filter as proposed in [135], NSST (NSST-Avg.-Max.) based scheme with one decomposition level and averaging fusion rule for LF sub-band and maximum selection rule for detail sub-bands as proposed in [136], NSCT-SF-PCNN based scheme as proposed in [90] with five decomposition levels and 1, 2, 8, 16, 16 directions from coarser to finer scales. NSST-SF-PCNN based scheme as proposed in [43] with three decomposition levels and 8, 16, 16 directions from coarser to the finer scale. Three sets of experiments are performed to test the performance of the NSST-Morphological gradient-PCNN based method with the aforementioned schemes. The details of the experiments are given as follows:

Experiment 1: Visual comparison of the proposed methodology- NSST-Morphological gradient-PCNN based fusion algorithm with five states of the art methods using primary (PGIMER) and secondary (Harvard medical school) datasets.

Experiment 2: Average parametric comparison of the proposed method with five states of the art methods using CT and T2-weighted MR images acquired from PGIMER and Harvard medical school website.

Experiment 3: Comparison of average (CPU) computation speed (time in seconds) of the proposed fusion algorithm with respect to five classical fusion schemes.

4.3.1 Evaluation Criteria

The proposed methodology has been evaluated using qualitative and quantitative means which are explained below:

4.3.1.1 Qualitative analysis

The visual evaluation of the fused image is done by considering the ability of the fused image to keep the bone and parenchymal information of CT and MR images, respectively. The ability of the fused image to retain the local structural information, contrast, brightness, texture and edge details of different image features of source images is observed. The images are shown to two expert radiologists independently to validate the visual performance of the proposed algorithm. Histopathology evaluation and correlation is done by experts wherever available.

4.3.1.2 Quantitative analysis- parametric evaluation

In order to statistically evaluate the fused image of the proposed scheme, five assessment metrics named SD, MI, SF, $Q^{AB/F}$ and mean are considered in this research.

4.4 RESULTS AND DISCUSSIONS

4.4.1 Visual Analysis

The visual comparison of fusion images of the proposed methodology with different classical fusion schemes has been done and is shown in Figure 4.6, Figure 4.7 and Figure 4.8. This is explained as follows:

Experiment 1: Figure 4.6 and Figure 4.8 show the fusion results of different methods for 2 pairs of PGIMER dataset. Figure 4.6(a), CT image shows the presence of a focal lesion in the right occipital lobe with central hypodensity (necrosis) and peripheral enhancement. The hypodensity surrounding the lesion is parenchymal edema. The Corresponding T2 weighted MR image in Figure 4.6(b) shows the lesion definition better and adjoining perilesional edema very well. Figure 4.6(c, d, e) shows fused image of DWT [135], SWT [135] and NSST [136] based schemes. The contrast and clarity of lesion, parenchymal edema, CSF

and bone can be appreciated in a single fused image, though the quality is not as good as expected in either of these methods. Looking at Figure 4.6(f), NSCT [90] based scheme the parenchymal details appear inhomogeneous at places, though at other places within the image they appear better and bone information is also distorted. To better differentiate this method with the proposed method the zoomed region of this scheme and the proposed scheme are shown in Figure 4.7. As seen in the magnified images on the right-hand side of this figure, improved details of CT and MRI are obtained in the proposed scheme as compared to the other scheme. Bone information is better retained in Figure 4.6(g) in NSST [43] based scheme however, lesion and parenchymal information are distorted. Looking at Figure 4.6(h), it is easy to see better bone, lesion and parenchymal details as per the clinical format required for disease evaluation by the radiologists. Figure 4.8(a) shows another CT image that demonstrates a calcified bi-thalamic lesion with no apparent adjoining parenchymal changes. The parenchymal changes (non-calcified lesion) are well demonstrated on the MR image which is marked with the yellow arrow in Figure 4.8(b). The fused image of the proposed NSST-Morphological Gradient-PCNN based scheme shows the parenchymal change of MR image in a better manner as marked by the yellow arrow in Figure 4.8(h). This parenchymal change is not visible in the fused image of other schemes as shown in Figure 4.8(c, d, e, f, g) with yellow arrows.

Figure 4.9 shows the fusion results of different methods for 1 pair of Harvard medical school dataset. The CT image of Figure 4.9(a) shows edema in the left parieto-occipital lobe whose boundary is not clearly defined. The corresponding MR image presented in Figure 4.9(b) shows the edema boundary clearly. The edema extension into normal parenchyma is not well defined in the fused image of DWT, SWT, NSST-Avg.-Max., NSCT-SF-PCNN and NSST-SF-PCNN based schemes whereas, it is better visible in the fusion result of the the proposed algorithm as shown in Figure 4.9(c, d, e, f, g, h), respectively.

Each fused image of the proposed scheme is rated independently by two radiologists on a scale of 1 to 4; 1 representing low, 2: moderate, 3: high, 4: very high level of consent. The evaluation criteria were resolution of morphological details in the fused images, adequacy of demonstration of the pathology and ease of information extraction in the fused images vis-a-vis individual CT and MR images. The average score was 3.2 by radiologist 1 and 3.4 by radiologist 2. As per their view, the fusion images derived from the proposed scheme are superior to other fusion schemes.

4.4.2 Quantitative Analysis

Five fusion performance parameters as mentioned in subsection 4.3.1.2 are computed for all the fused images and their average values are recorded in Table 4.1 and Table 4.2.

Experiment 2: Table 4.1 shows the average parametric comparison of 08 image pairs of the primary-PGIMER dataset. It is observed from this table that the value of all the performance parameters is highest for the proposed method except the $Q^{AB/F}$. This parameter is second highest for the proposed scheme and is lesser than NSCT-SF-PCNN based scheme. The number of decomposition levels set for the NSCT-SF-PCNN based scheme is five with

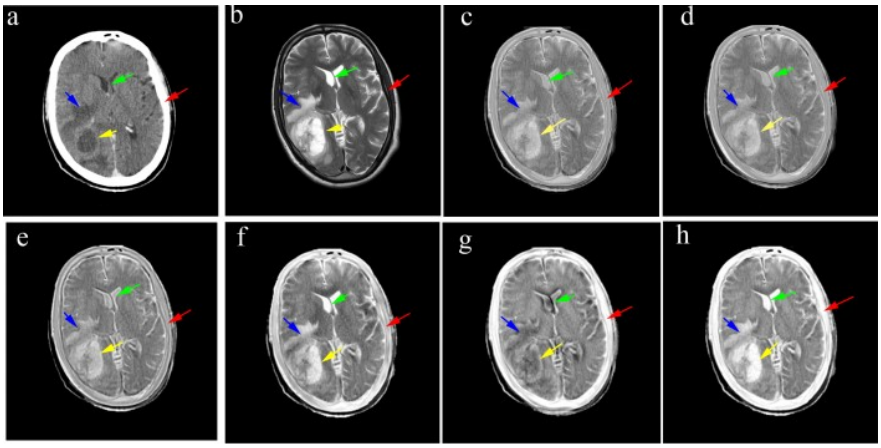

Figure 4.6 Various transforms fusion results of diseased - tumor

Red arrow – bone, green arrow - CSF, blue arrow- edema, yellow arrow – lesion
(a) CT image
(b) MR image
(c) Discrete wavelet transform
(d) Stationary wavelet transform
(e) Non-subsampled shearlet transform and avg.-max. fusion rule
(f) Non-subsampled contourlet transform and SF as fusion rule
(g) Non-subsampled shearlet transform and SF as fusion rule
(h) Proposed non-subsampled shearlet transform and morphological gradient-based fusion scheme

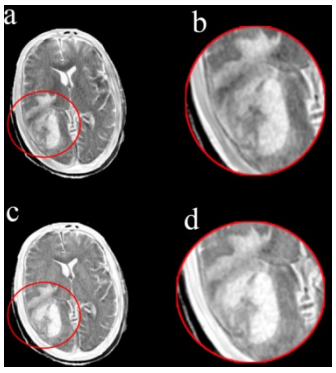

Figure 4.7 Zoomed regions of Figure 4.6 (f, h)

(a) Non-subsampled contourlet transform and SF as fusion rule
(b) Zoomed image of circled region of Figure 4.7 (a)
(c) Proposed non-subsampled shearlet transform and morphological gradient-based fusion scheme
(d) Zoomed image of circled region of Figure 4.7 (c)

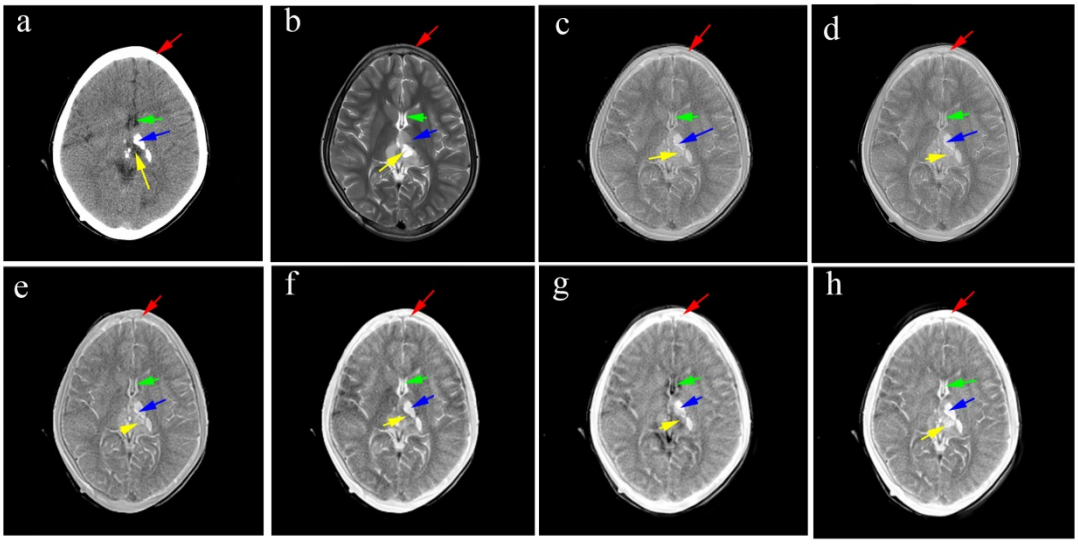

Figure 4.8 Various transforms fusion results of diseased - calcified bi-thalamic lesion

Red arrow – bone, green arrow - CSF, blue- calcified lesion, yellow arrow – non-calcified lesion
(a) CT image
(b) MR image
(c) Discrete wavelet transform
(d) Stationary wavelet transform
(e) Non-subsampled shearlet transform and avg.-max. fusion rule
(f) Non-subsampled contourlet transform and SF as fusion rule
(g) Non-subsampled shearlet transform and SF as fusion rule
(h) Proposed non-subsampled shearlet transform and morphological gradient-based fusion scheme

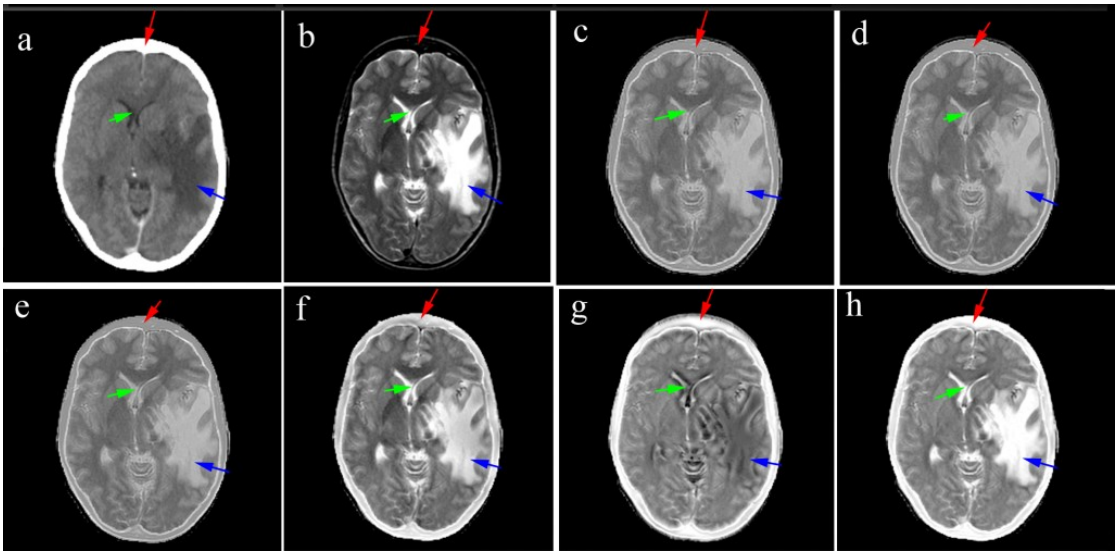

Figure.4.9 Various transforms fusion results of diseased - metastatic bronchogenic carcinoma

Red arrow – bone, green arrow - CSF, blue arrow –edema
(a) CT image
(b) MR image
(c) Discrete wavelet transform
(d) Stationary wavelet transform
(e) Non-subsampled shearlet transform and avg.-max. fusion rule
(f) Non-subsampled contourlet transform and SF as fusion rule
(g) Non-subsampled shearlet transform and SF as fusion rule
(h) Proposed non-subsampled shearlet transform and morphological gradient-based fusion scheme

directions as 1, 2, 8, 16, 16 from coarse to fine-scale whereas for the proposed scheme only three decomposition levels with 4, 8, 8 directions from coarse to fine-scale are employed. This may be the reason for the reduction of this parameter by a difference of 0.01 for the proposed scheme compared to the NSCT-SF-PCNN based algorithm. Table 4.2 shows

Table 4.1 Averaged Parametric Comparison of 08 Pairs (CT and T2-Weighted MR Images) of Primary (PGIMER) Dataset

Method	MI	$Q^{AB/F}$	SF	SD	Mean
CT image	--	--	19.0275	75.1675	46.9536
MR image	--	--	19.2829	48.3619	33.3476
DWT [135]	2.8376	0.4227	19.7977	57.7954	38.5113
SWT [135]	2.6701	0.4806	15.5183	58.4420	38.5318
NSST [136]	2.8631	0.4647	18.0581	57.8345	38.5015
NSCT [90]	2.7682	**0.5908**	23.4375	68.7876	43.9797
NSST [43]	2.7753	0.4885	21.8376	74.1612	47.4956
Proposed scheme	**2.8997**	0.5754	**23.8672**	**77.6422**	**49.7269**

Table 4.2 Averaged Parametric Comparison of 09 Pairs (CT and T2-Weighted MR Images) of Public (Harvard Medical School) Dataset

Method	MI	$Q^{AB/F}$	SF	SD	Mean
CT image	--	--	28.7732	75.2336	44.7729
MR image	--	--	19.0816	45.7445	30.7185
DWT [135]	2.7938	0.3790	24.3920	62.3313	51.4659
SWT [135]	2.8748	0.4197	23.2533	62.4088	51.4395
NSST [136]	2.8573	0.4041	23.1759	62.2978	51.4432
NSCT [90]	2.6906	**0.5116**	28.4693	74.7100	57.3408
NSST [43]	2.8645	0.4273	27.4014	81.3628	59.3426
Proposed scheme	**2.9251**	0.5050	**29.1112**	**86.4337**	**68.0380**

the average parametric comparison of 09 pairs of CT and T2-weighted MR images of the secondary-Harvard medical school dataset. Similar parametric performance is seen for this dataset also i.e. all the statistical parameters are highest for the NSST-Morphological gradient-PCNN based scheme except the $Q^{AB/F}$.

Experiment 3: The computational time taken by the various fusion algorithms for the datasets of PGIMER and Harvard medical school were recorded by repeating the

experiment ten times for each dataset and average values were computed which are shown in Table 4.3. It is observed that the computational time of the proposed fusion scheme is quite smaller than other PCNN based schemes for both the datasets, though the minimum computational time is consumed by the NSST-Avg.-Max fusion scheme. This is due to the faster computation of the simple formula of the morphological gradient using 5x5 structuring element as the MG does not depend upon the edge directionality to a large extent.

In view of this discussion, it can be concluded from Experiment 1 that the proposed NSST based method is effective and better in carrying the bone, lesion, CSF and edema details in the clinical format required for disease evaluation by the neuro-radiologists as compared to

Table 4.3 Average Computational Speed (Time in Seconds) Comparison

Dataset	DWT	SWT	NSST	NSCT	NSST	Proposed
PGIMER	1.1976	1.2442	0.3017	93.1101	62.4644	12.9710
Harvard	1.2117	1.4315	0.3177	90.4061	61.8989	13.4894

the conventional methods which include DWT, SWT, NSST-avg.-max., NSCT-SF-PCNN and NSST-SF-PCNN based schemes. The results of the visual inspection are also advocated by the results of Experiment 2 in relation to better outcomes of MI, $Q^{AB/F}$, SD, SF and mean parameters. This demonstrates better texture, contrast, local structural details, edge information and brightness in the fusion image of the proposed methodology and supports the visual analysis of the proposed methodology. From Experiment 3 it is evident that the proposed scheme is computationally faster than other PCNN based schemes.

4.5 CONCLUSIONS

In order to reduce the computational complexity of PCNN based fusion algorithms, a novel morphological gradient motivated simplified PCNN model is proposed in this research. The regional energy-based saliency as an activity measure is utilized to fuse the LF sub-band and novel morphological gradient motivated PCNN to fuse detail sub-bands of NSST, respectively. The ability of the proposed algorithm to retain features of brain source images such as bones, CSF, soft tissues and edema is evaluated by visual inspection and fusion performance parameters. The presented fusion scheme is compared with five states of the art fusion methods visually and using five fusion quality assessment parameters. From visual inspection of fused images, it is concluded that the novel morphological gradient motivated NSST-PCNN fusion scheme is superior in retaining the features like bone and parenchyma of source images in a better manner. Evaluation of the fusion quality

assessment parameters with five different fusion schemes confirms the superiority of the proposed scheme in retaining texture, contrast, clarity, edge information and brightness of the source images. The fusion outcome of the proposed methodology is utilized by radiologists for monitoring, diagnosis and surgical procedures of various diseased conditions. The composite fusion image can be used by the medical society to study brain anatomy.

CHAPTER 5

HYBRID FUSION SCHEME USING NSCT AND SWT

5.1 INTRODUCTION

The Pixel level hybrid fusion scheme is discussed in this chapter which is based on non-subsampled contourlet transform and stationary wavelet transform. It is observed from the literature that stationary wavelet transform (SWT) is better in representing small features like textures and point discontinuities whereas, NSCT gives better edge information. However, NSCT is unable to resolve small features in a well-defined manner [81, 100]. To capture the curved information, SWT needs many fine square-shaped dots whereas, NSCT uses elongated shapes and in different directions along the black curve as shown in Figure 5.1 [81]. The different colors in this figure correspond to multi-resolution square boxes and elongated shapes.

The complementary properties of SWT and NSCT are explained in the following section. Suppose there is a portion of an image that represents the edges in the curved areas and texture as shown in Figure 5.2(a). It is obtained by fusing a CT and MR image using SWT. Figure 5.2(b) shows a similar image obtained by fusing the same dataset using NSCT. A careful inspection of these images shows that the edge information in the fused image of NSCT based scheme is better than SWT based scheme as indicated by red arrows in Figure 5.2(a) and Figure 5.2(b). The minute details of tumor morphology (texture information of edema) are better in the area marked by blue arrows in Figure 5.2(a) than Figure 5.2(b) where the region seems to be more textured but noisy. It specifies that the two transforms are complementary in nature i.e. NSCT carries better edge details whereas SWT carries better texture information. The above features are employed in the best possible way in the proposed scheme and hence, NSCT is used to decompose the source images into LF and detail layers. In the next step, the LF sub-band of NSCT is processed and fused through SWT decomposition. To the best knowledge of the author the use of SWT with entropy and weighted sum-modified Laplacian (WSML) based fusion rules for the fusion of low passband of NSCT, is unexplored yet. Therefore, these rules are employed with SWT as LF and HF subband fusion rules. In the next step, HF sub-bands of NSCT are fused using the maximum weighted sum of the square of the coefficients within a 3×3 window-based activity measure. This is followed by the consistency verification of these coefficients. These steps are explained in more detail in section 5.3 of this chapter.

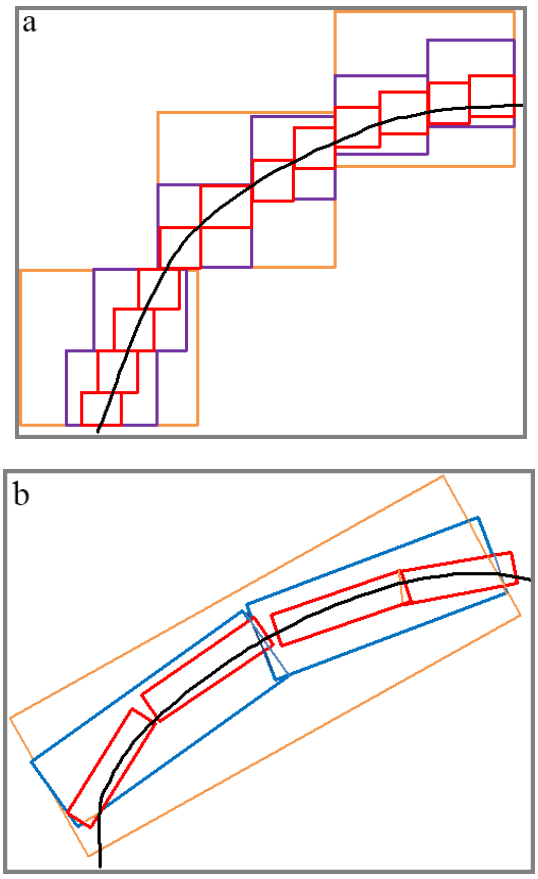

Figure 5.1 Multi-resolution analysis

(a) Stationary wavelet transform of curve
(b) Non-subsampled contourlet transform of curve

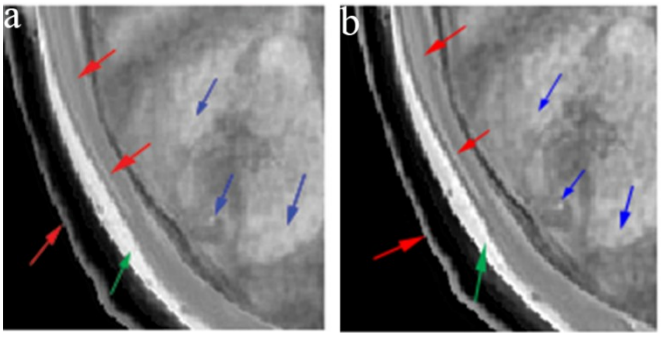

Figure 5.2 Comparison of SWT and NSCT based fusion image

(a) SWT extraction curved information
(b) NSCT extraction curved information

5.2 METHODOLOGY

The proposed methodology is described in this section. The block diagram of the proposed methodology is represented in Figure 5.3. The various stages of the block diagram are explained in the following subsections. Initially, the source images are registered using the intensity-based registration scheme discussed in section 4.2.1 of Chapter 4. The images

after the registration process are converted from RGB color space to greyscale. This step is followed by the 1st level of image decomposition using NSCT.

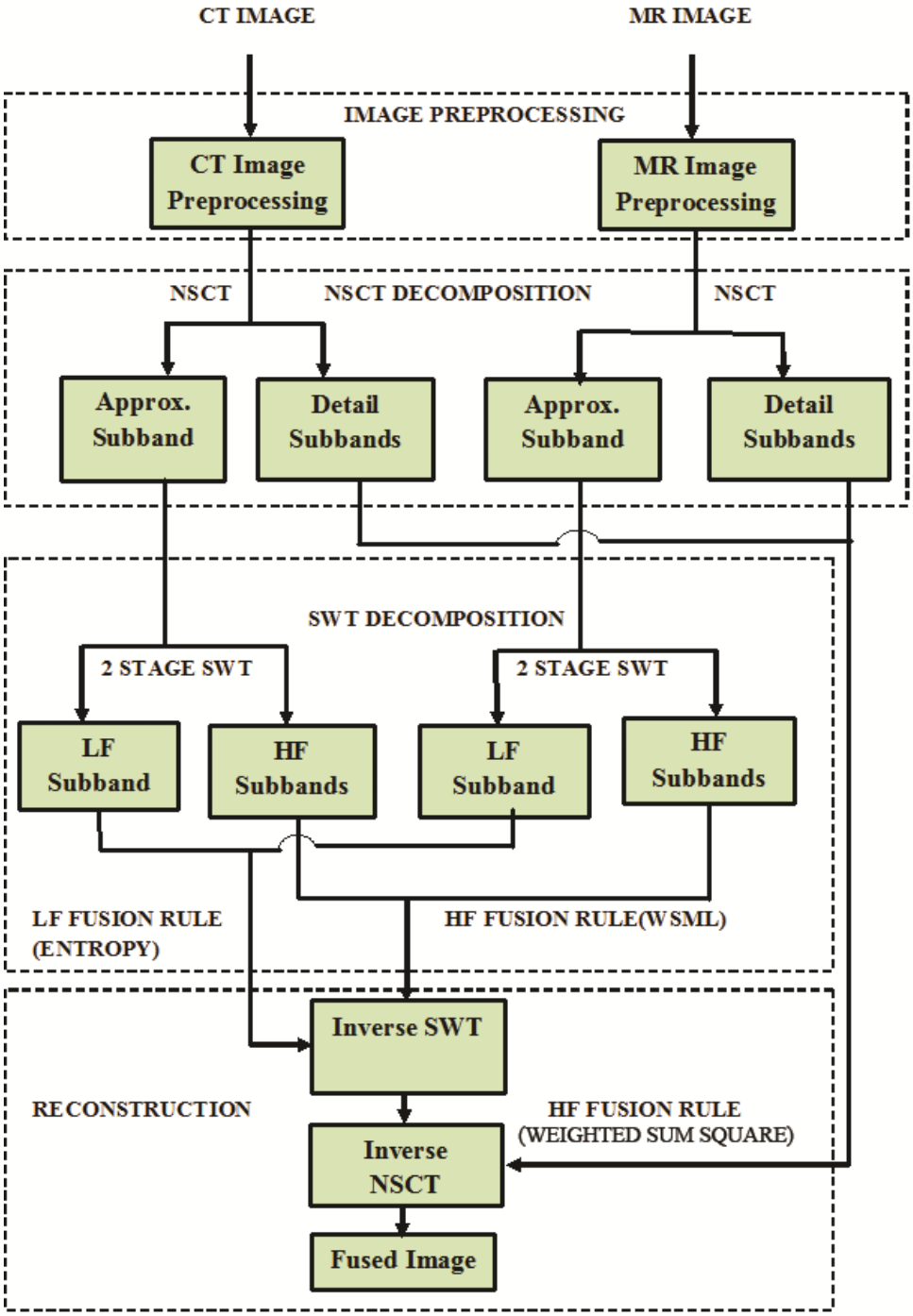

Figure 5.3 Block diagram of the proposed methodology

5.2.1 Non-Subsampled Contourlet Transform (NSCT) Decomposition

NSCT is derived from contourlet transform by removing the downsamplers which ensures the shift-invariant property of this transform [82, 91] because the change of sample by one value in the input provides same change in the output. Due to shift variance of contourlet

transform, a small change in the input image creates unpredictable changes in the energy distribution of detail subbands coefficients which result in blocking artifacts in the resultant image. The multiscale and multidirectional property of NSCT makes it suitable to extract edges, curves and contours from images and is very convenient for image fusion as compared to contourlet transform. Shift invariance property also makes is less prone to misregistration errors. The basic building blocks of NSCT are (i) Non-subsampled pyramid filter bank (NPFB) (ii) Non-subsampled directional filter bank (NSDFB).

The NSCT decomposes the image into different scales using NPFB. The NPFB decomposes the original image into a low pass (approximation) subband image and another high pass subband image [137, 138]. The output of one-stage of NPFB is similar to nonsubsampled Laplacian pyramid filter bank which is employed in the contourlet transform. A two-channel nonsubsampled filter bank is shown in Figure 5.4(a), where $H_0(Z)$ and $H_1(Z)$ are the low pass and high pass analysis filters and $G_0(Z)$ and $G_1(Z)$ are the respective synthesis filters. The synthesis filters are required to remove the aliasing effect for perfect reconstruction and to make the filter design less complex. $H_1(Z)$ is derived as $H_1(Z) = 1-H_0(Z)$ and $G_0(Z) = G_1(Z) =1$. The condition for perfect reconstruction is $H_0(Z)\ G_0(Z) + H_1(Z)\ G_1(Z) = 1$. The NPFB is applied to the LF subband image to produce the next (second) stage decomposition forming a pyramid-like structure of different resolution images.

Non-subsampled directional filter bank (NSDFB) uses a two-channel fan filter bank that splits the two-dimensional frequency spectrum into horizontal and vertical directions. The fan filters are constructed from diamond shape filters using suitable frequency mapping i.e. modulating one of the frequency variables by suitable mapping function which is the quincunx matrix as expressed by eqn. 5.1. The next stage is constructed by upsampling fan filter banks output using a quincunx matrix Q as expressed by eqn.5.1 which has a checkerboard frequency pattern in the second stage as shown in Figure 5.4(b) [45, 139]. This figure shows a four-channel NSDFB generated using 2 channel fan filter banks. The analysis filters of the first stage are represented by $U_0(Z)$ and $U_1(Z)$ in Figure 5.4(b).

$$Q = \begin{bmatrix} 1 & 1 \\ 1 & -1 \end{bmatrix} \tag{5.1}$$

The second stage synthesis filters are represented by $U_0(Z^Q)$ and $U_1(Z^Q)$. The outputs Y_0, Y_1, Y_2 and Y_3 of the second stage of NSDFB contain four wedge-shaped directional subbands as shown in Figure 5.4(c). The shape of the filters decides the type of directional

subband obtained. For example, the diamond shape filter having checkerboard pattern divides the frequency plane into four directional subbands as shown in Figure 5.4 (c). The subbands numbered 0 and 1 in this figure are almost horizontal in direction and the subbands 2 and 3 are mostly vertical. In general, an L level NSDFB produces 2^L directional subbands. When NSLP and NSDFB are combined together the resultant structure is called the nonsubsampled contourlet transform which is shown in Figure 5.4(d). The first stage LPF and second stage LPF are represented by $H_0(Z)$ and $H_0(Z^2)$, respectively in this figure. The first stage HPF and second stage HPF are represented by $H_1(Z)$ and $H_1(Z^2)$, respectively in Figure 5.4(d). A three-level decomposition process of NSCT is employed in this research and is shown in Figure 5.5. Based upon the above analysis, it is concluded that NSCT is nonsubsampled version of contourlet transform which is derived from it by removing downsamplers and upsamplers. This makes this transform shift-invariant. Another difference is in the design of the pyramid filter bank structure, NSCT employs nonsubsampled filter bank structure whereas, CT employs a subsampled Laplacian pyramid structure. The pyramid filter banks of NSCT are designed using a ladder or lifting structure to simplify the computations. The nonsubsampled pyramid structure captures point discontinuities which are passed to directional filter banks to link point discontinuities into linear structures and hence, edges and contours are detected. The source image to be decomposed through NSCT is fed to a non-subsampled pyramid filter bank (NPFB) at decomposition stage 1 (d =1). The NPFB decomposes the source image into an LF sub-band and an HF sub-band image [92]. HF sub-band image at a stage is fed to a non-subsampled directional filter bank (NDFB) to produce directional sub-bands. In the presented scheme CT and MR images are decomposed through NSCT up to three scales represented by d = 1, 2, 3 in the figure with directions k = 8, 8, 4, respectively. The directional sub-band images of different stages and approximation sub-band image at scale 3 of a real MR image are shown in Figure 5.5.

5.2.2 Stationary Wavelet Transform (SWT) Decomposition

In the present research, the low pass-band of NSCT decomposition is processed using SWT. The SWT is described below.

Let f(t) be any function in one dimension. Its continuous wavelet transform is obtained by applying this function with a wavelet function. The wavelet function is expressed as follow:

$$\psi_{a,b}(t) = \frac{1}{\sqrt{a}}\psi\left(\frac{t-b}{a}\right) \tag{5.2}$$

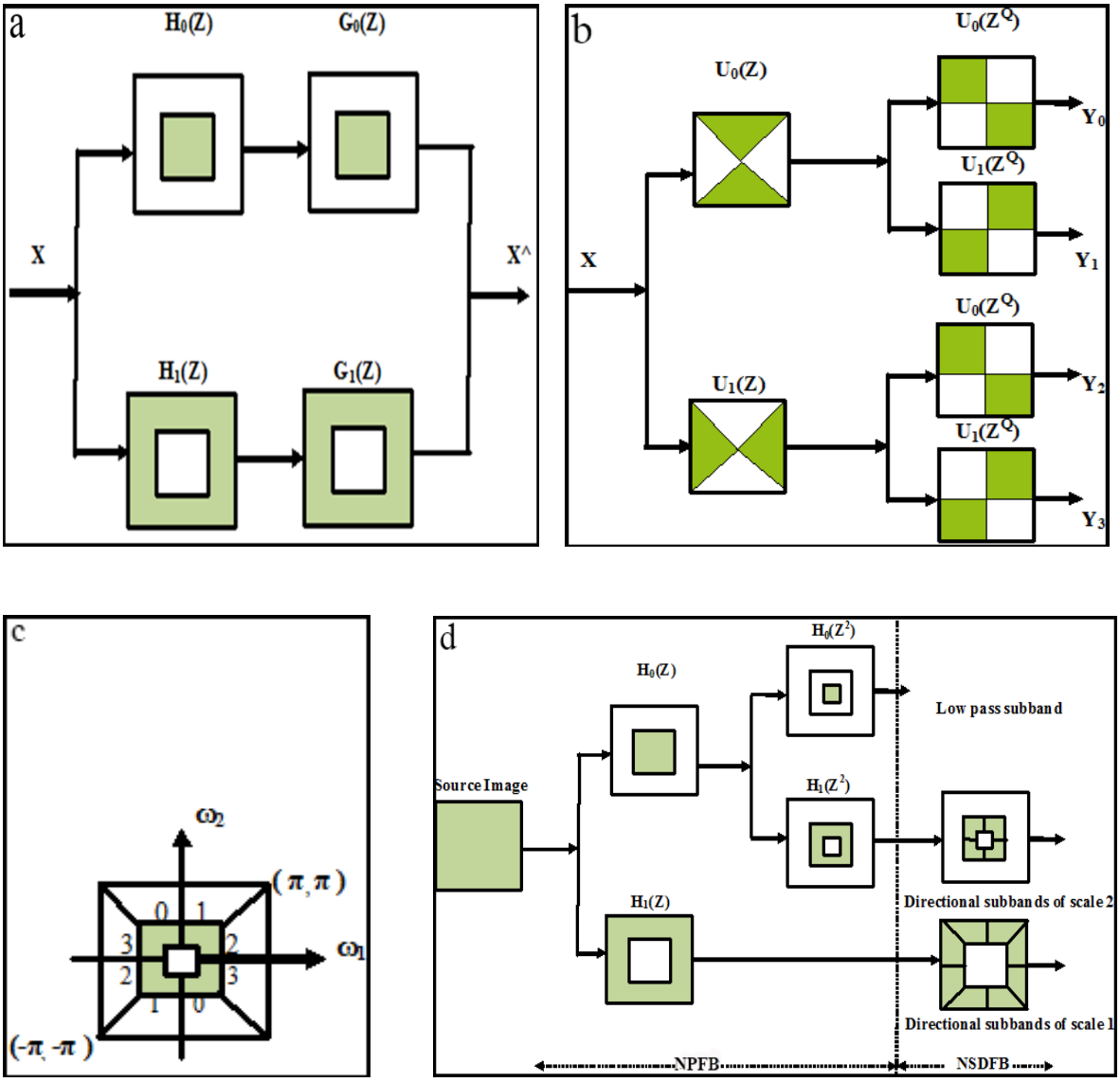

Figure 5.4 Image decomposition process of nonsubsampled contourlet transform

(a) Nonsubsampled pyramid filter bank
(b) Four-channel nonsubsampled directional filter bank
(c) Four wedge-shaped directional subbands (frequency partitioning).
(d) Nonsubsampled contourlet transform.

The wavelet transform of the function f (t) can be represented as:

$$W(a,b) = \int_R f(t)\psi^*_{a,b}(t)dt \qquad (5.3)$$

where, a and b are scale and translation parameters, respectively. '*' represents complex conjugation [140]. In the case of standard discrete wavelet transform (DWT) $a = 2^j$ and $b = m2^j$ $(j, m \in z)$. SWT is constructed from DWT by eliminating down samplers from it. Instead, upsamplers are used to insert zeros between the low pass and high pass filter

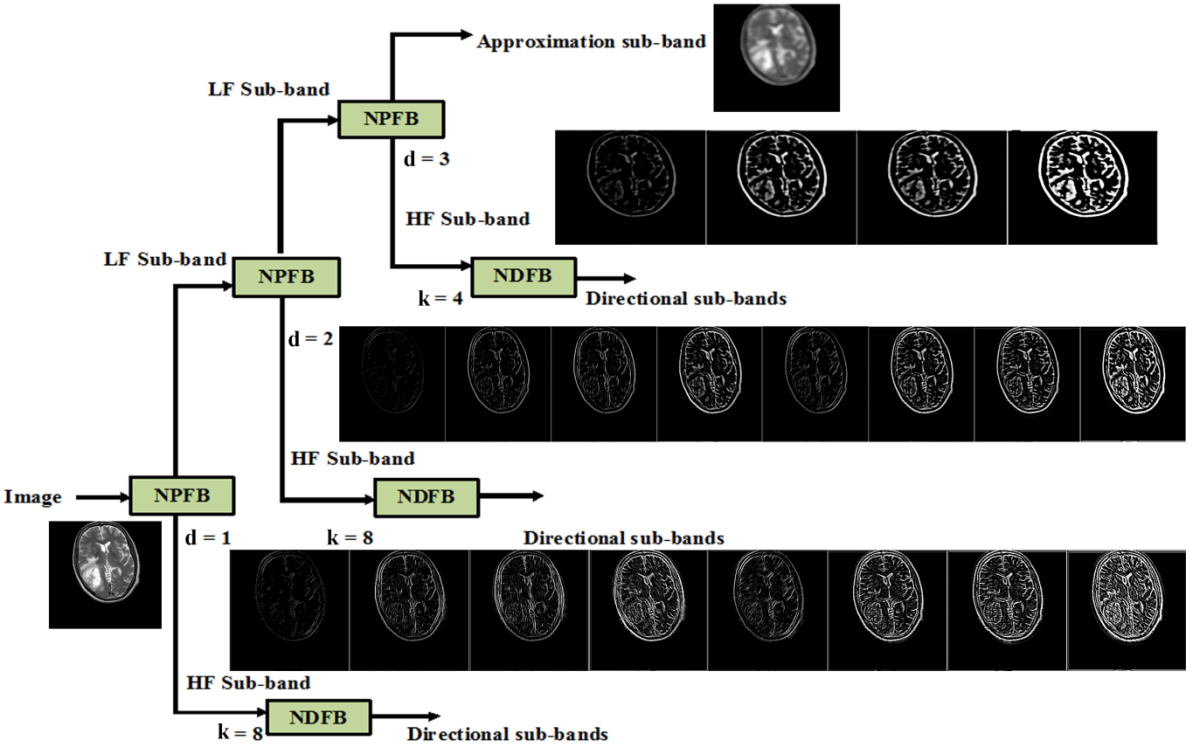

Figure 5.5 Three-level image decomposition process of the NSCT

coefficients [103]. The SWT decomposition using a bank of LF and HF filters is shown in Figure 5.6. An N Level decomposition results in 3N+1 frequency subbands. The N+1th level coefficients are computed from level N using the following equations:

$$A_{x,n+1}(m,n)=\sum_i\sum_j g_i^n g_j^n A_{x,n}(m+i,n+j) \tag{5.4}$$

$$D^v_{x,n+1}(m,n)=\sum_i\sum_j h_i^n g_j^n A_{x,n}(m+i,n+j) \tag{5.5}$$

$$D^h_{x,n+1}(m,n)=\sum_i\sum_j g_i^n h_j^n A_{x,n}(m+i,n+j) \tag{5.6}$$

$$D^d_{x,n+1}(m,n)=\sum_i\sum_j h_i^n h_j^n A_{x,n}(m+i,n+j) \tag{5.7}$$

where, (m,n) represents the current pixel location, $A_{x,n}$ represents the approximation coefficient at nth scale. The symbols g and h represent the LPF and HPF, respectively. The rows and columns of an image are filtered separately by the SWT. At a specific scale, one approximation image ($A_{x,n}$) and three detail images containing horizontal details ($D^h_{x,n}$),

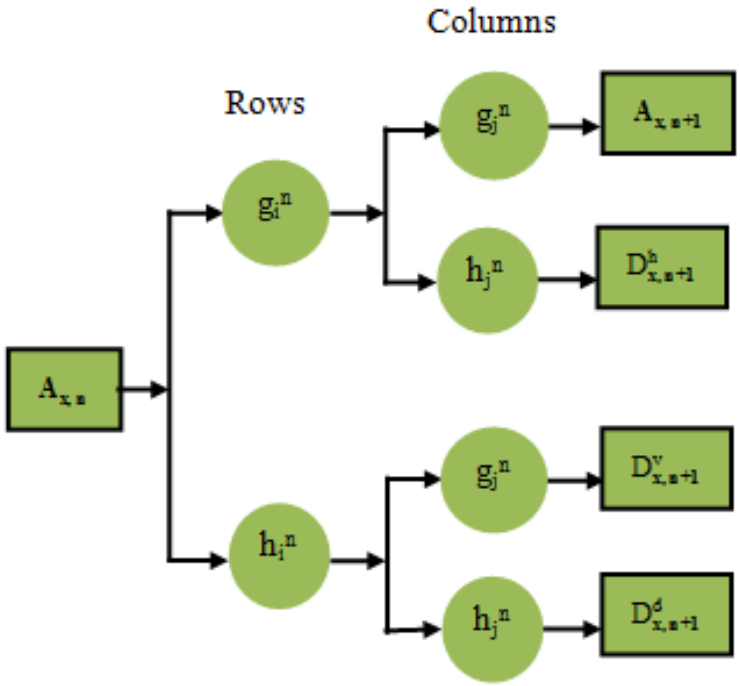

Figure.5.6 Decomposition process of SWT

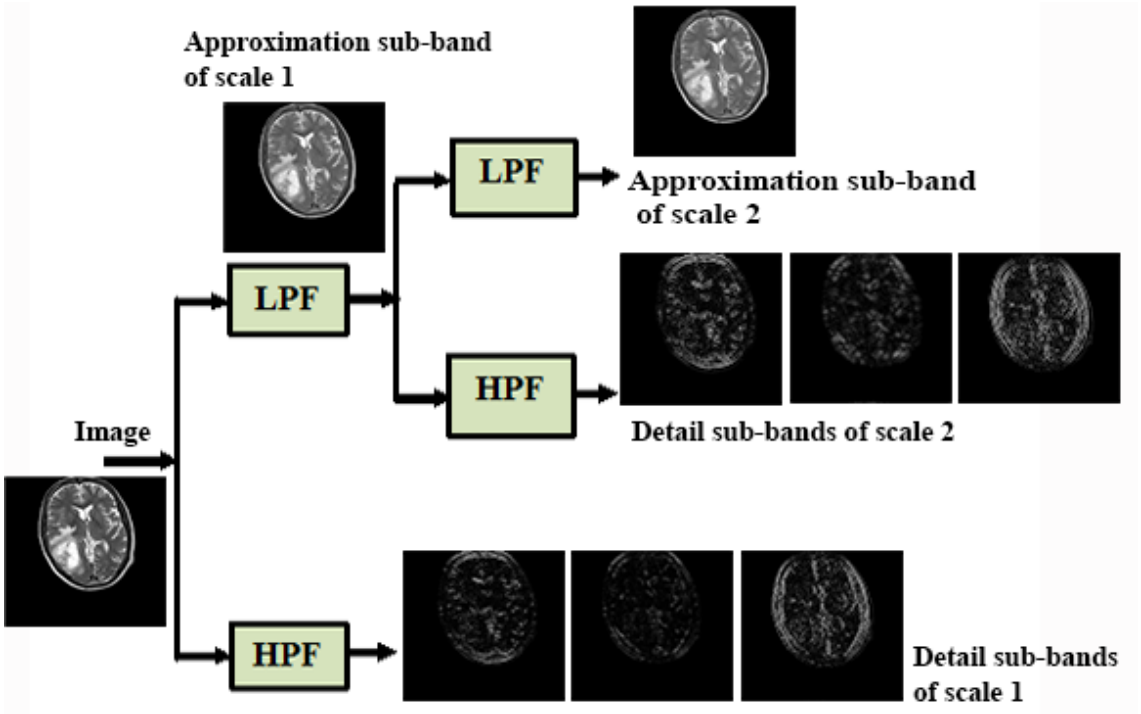

Figure 5.7 A simplified two-level image decomposition process of the SWT

vertical details ($D^v_{x,n}$) and diagonal information ($D^d_{x,n}$) are obtained. The SWT is superior in representing the texture information of an image. Figure 5.7 shows a simplified two-level decomposition process of SWT. In this figure, the approximation and detail sub-bands of both the stages for a real MR image are also shown. A two-level decomposition is done in

order to acquire better point curve and texture information from the LF sub-band image of the NSCT.

5.2.3 NSCT reconstruction of fusion image

The fused LF sub-band of NSCT is reconstructed using inverse SWT. The final fusion image is constructed by using inverse NSCT on the fused approximation and detail sub-band coefficients of NSCT.

5.3 PROPOSED FUSION FRAMEWORK

In the proposed algorithm, the CT image is denoted by A and MR image is represented by B. Initially the images are decomposed by NSCT up to three levels. HF coefficients of NSCT are fused using the weighted local sum of the square of the coefficients based rule. The LF sub-band of NSCT is processed through SWT. LF coefficients of SWT are fused using entropy-based fusion rule and HF coefficients using weighted sum modified Laplacian (WSML) based rule. The proposed scheme is explained using mathematical expressions as follows:

Step 1: In the first stage the source images A and B are decomposed using NSCT into approximation (approx.) sub-band (LF_A^{NSCT}, LF_B^{NSCT}) and a sequence of detail sub-bands (HF_A^{NSCT}, HF_B^{NSCT}). The image decomposition is done up to level d = 3 with directions k = 8, 8, 4 from fine to coarse-scale, respectively.

$$\mathrm{NSCT(A)} = \left[LF_A^{NSCT}, HF_A^{NSCT} \right] \tag{5.8}$$

$$\mathrm{NSCT(B)} = \left[LF_B^{NSCT}, HF_B^{NSCT} \right] \tag{5.9}$$

Step 2: The subbands LF_A^{NSCT} and LF_B^{NSCT} obtained in step 1 are decomposed further into low (LF_A^{SWT}, LF_B^{SWT}) and high-frequency sub-bands (HF_A^{SWT}, HF_B^{SWT}) using the stationary wavelet transform.

$$\mathrm{SWT}(LF_A^{NSCT}) = \left[LF_A^{SWT}, HF_A^{SWT} \right] \tag{5.10}$$

$$\mathrm{SWT}(LF_B^{NSCT}) = \left[LF_B^{SWT}, HF_B^{SWT} \right] \tag{5.11}$$

The LF components LF_A^{SWT} and LF_B^{SWT} are further decomposed into LF and HF sub-bands using SWT termed as second-level decomposition. These steps provide better edge and texture information on low-frequency components of bone and soft tissues.

Step 3: The LF sub-band of SWT is fused using maximum entropy of square of its coefficients within a 3 × 3 window. This activity level for image A is given as:

$$A_L(m,n) = \sum_{i=-1}^{1}\sum_{j=-1}^{1} C_{AL}^2(m+i,n+j)\log\left(C_{AL}^2(m+i,n+j)\right) \Big/ 9 \tag{5.12}$$

where, $C_{AL}(m,n)$ is the LF sub-band coefficient of image A at position (m, n). Similarly, this activity level for image B is also computed. The fused LF sub-band coefficients of SWT (LF_{Fused}^{SWT}) are obtained by applying the maximum selection rule on these entropy-based activity measures.

Step 4: The high-frequency sub-band coefficients HF_A^{SWT} and HF_B^{SWT} are fused by applying the WSML as an activity measure within a 3×3 window. The modified Laplacian (ML) of HF_A^{SWT} of image A is given as follows:

$$\begin{aligned} ML[HF_A^{SWT}(m,n)] = &| 2HF_A^{SWT}(m,n) - HF_A^{SWT}(m-1,n) - HF_A^{SWT}(m+1,n) | \\ &+ | 2HF_A^{SWT}(m,n) - HF_A^{SWT}(m,n-1) - HF_A^{SWT}(m,n+1) | \end{aligned} \tag{5.13}$$

WSML is computed using the following expression:

$$WSML[HF_A^{SWT}(m,n)] = \sum_{i=-1}^{1}\sum_{j=-1}^{1} W(i+2,j+2) \times ML[HF_A^{SWT}(m+i,n+j)] \tag{5.14}$$

where, W [45] is a weight expressed by eqn.5.17. Similarly, compute this activity measure for image B. The fused HF coefficients of SWT (HF_{Fused}^{SWT}) are obtained by applying the absolute maximum selection fusion rule on these WSML based activity measures.

Step 5: To reconstruct the fused approximation sub-band of NSCT (LF_{Fused}^{NSCT})**,** inverse SWT is performed on LF_{Fused}^{SWT} and HF_{Fused}^{SWT} as obtained in step 3 and step 4, respectively.

$$LF_{Fused}^{NSCT} = SWT^{-1}(LF_{Fused}^{SWT}, HF_{Fused}^{SWT}) \tag{5.15}$$

Step 6: To fuse the high-frequency sub-band coefficients of NSCT i.e. to fuse the coefficients of HF_A^{NSCT} and HF_B^{NSCT}, a locally weighted sum of the square of the coefficients based fusion rule with consistency verification is employed. This ensures that the dominant features are included in the fused image. It is explained as follows:

$$A_{d,k}(m,n) = \sum_{i=-1}^{1}\sum_{j=-1}^{1} W(i+2,j+2) \times \left|C_{d,k}^{A}(m+i,n+j)\right|^2 \tag{5.16}$$

where, $A_{d,k}(m,n)$ is activity level computed according to eqn.5.16 for image A. $C_{d,k}^{A}(m,n)$ is the d^{th} scale and k^{th} direction detail sub-band coefficient of image A at position m,n. The weight matrix W [45] is defined as:

$$W=\begin{bmatrix}1/16 & 2/16 & 1/16\\ 2/16 & 4/16 & 2/16\\ 1/16 & 2/16 & 1/16\end{bmatrix} \tag{5.17}$$

The weight matrix W has the Gaussian shape whose response matches the human visual response. In a similar way, the activity level $B_{d,k}(m,n)$ of the coefficient $C^{B}_{d,k}(m,n)$ for image B is also computed. The initial decision map is computed as:

$$map_i(m,n)=\begin{cases}1 & \text{if } A_{d,k}(m,n)\geq B_{d,k}(m,n)\\ 0 & \text{if } A_{d,k}(m,n)< B_{d,k}(m,n)\end{cases} \tag{5.18}$$

This map selects the coefficients having higher energy to contribute in the fusion image. This map is subjected to consistency verification employing a majority filter of size 3 × 3 which replaces the current coefficient by 1 if no. of one's in the window w are ≥ 5. The decision map after this operation is obtained as:

$$map_f(m,n)=\begin{cases}1 & \text{if } \sum_{W}\left[map_i(m,n),w\right]\geq 5\\ 0, & \text{Otherwise}\end{cases} \tag{5.19}$$

$map_f(m,n)$ makes the fused image more homogeneous. The fused detail coefficients $HF^{NSCT}_{Fused}(m,n)$ are obtained from eqn.5.19 as follows:

$$HF^{NSCT}_{Fused}(m,n)=\begin{cases}C^{A}_{d,k}(m,n) & \text{if } map_f(m,n)=1\\ C^{B}_{d,k}(m,n) & \text{if } map_f(m,n)=0\end{cases} \tag{5.20}$$

Step 7: The last step is performed for reconstructing the final image i.e. the fused image. Perform inverse NSCT on the fused coefficients of NSCT obtained in step 5 and step 6, respectively.

$$F=NSCT^{-1}(LF^{NSCT}_{Fused},HF^{NSCT}_{Fused}) \tag{5.21}$$

The stepwise output of the proposed algorithm for three pairs of primary (PGIMER) images is shown in Figure 5.8, Figure 5.9 and Figure 5.10. Figure 5.8(a,b), Figure 5.9(a,b) and Figure 5.10(a,b) represent CT and MR images, respectively. Figure 5.8(c,d), Figure 5.9(c,d) and Figure 5.10(c,d) represent NSCT decomposition images (HF) at scale 1. Figure 5.8(e,f), Figure 5.9(e,f) and Figure 5.10(e,f) represent NSCT decomposition at scale 2. The scale 3 images of NSCT are represented in Figure 5.8(g,h), Figure 5.9(g,h) and Figure 5.10(g,h). The approximation sub-band of NSCT is shown in Figure 5.8(i,j), Figure 5.9(i,j) and Figure

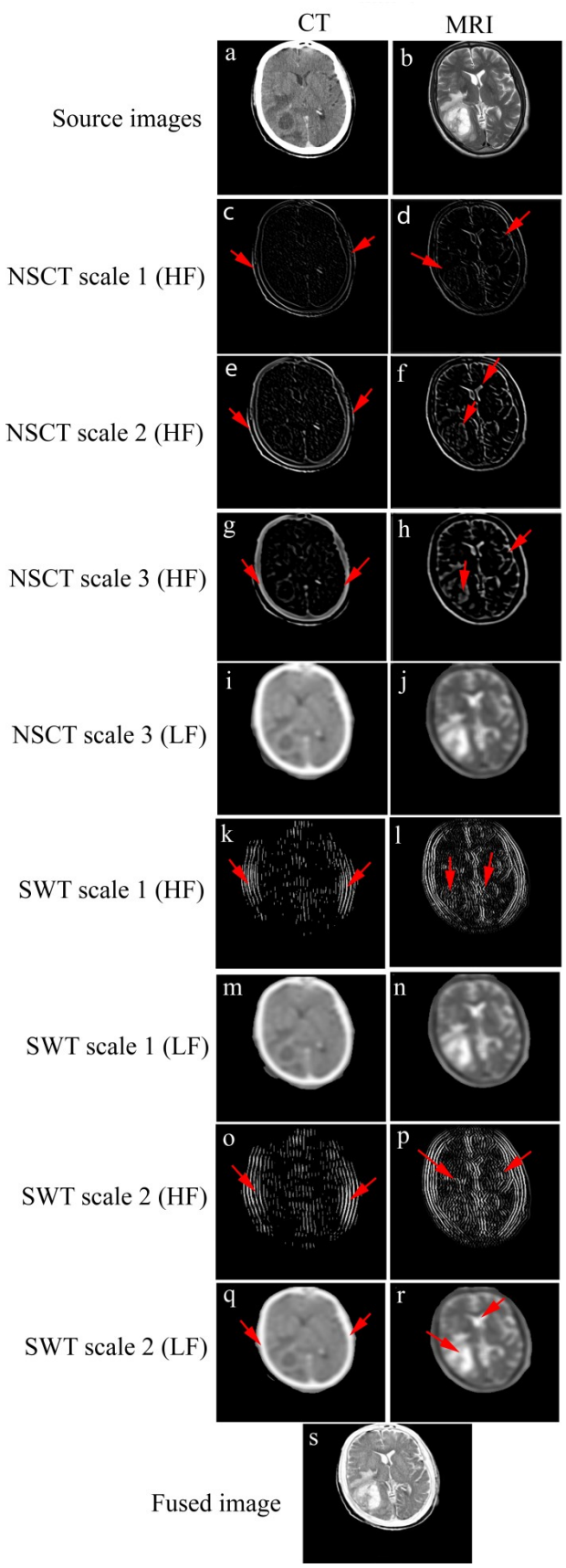

Figure 5.8 Stepwise decomposition results of the proposed algorithm for one pair of glioma images. The edges and textures of different subband images as indicated by arrows contribute in fusion

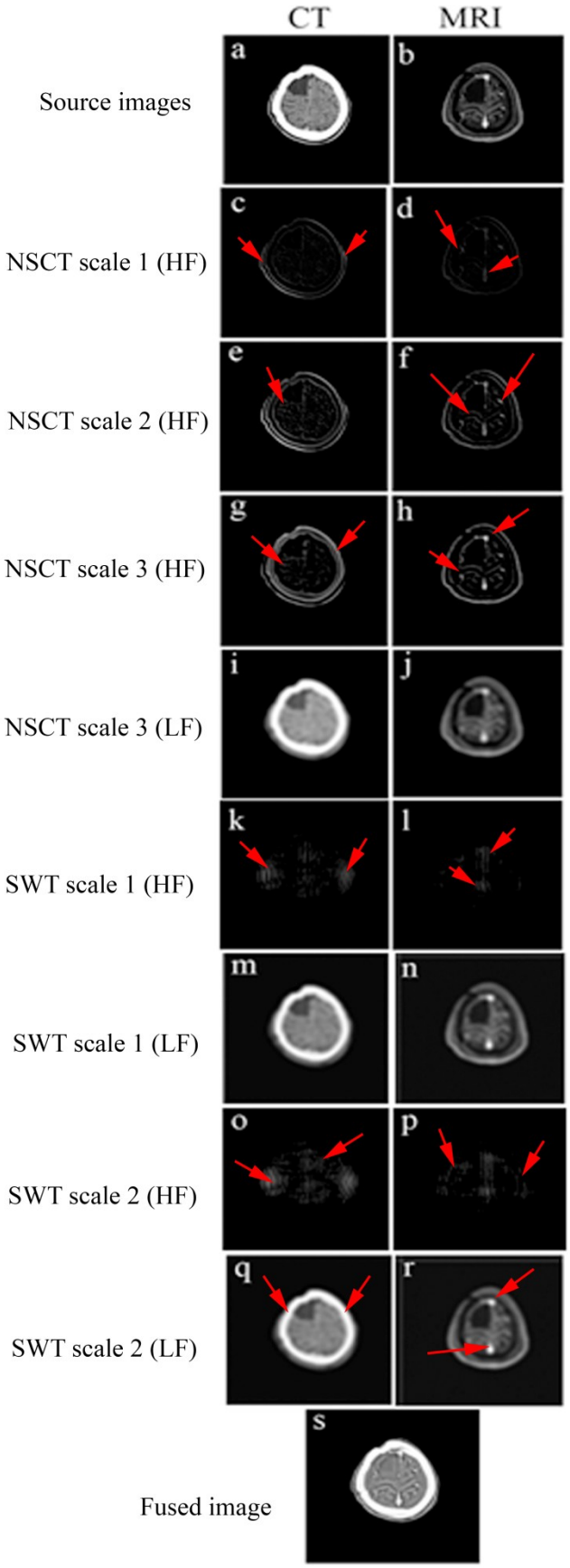

Figure 5.9 Stepwise decomposition results of the proposed algorithm for one pair of brain tumor images. The edges and textures of different subband images as indicated by arrows contribute in fusion

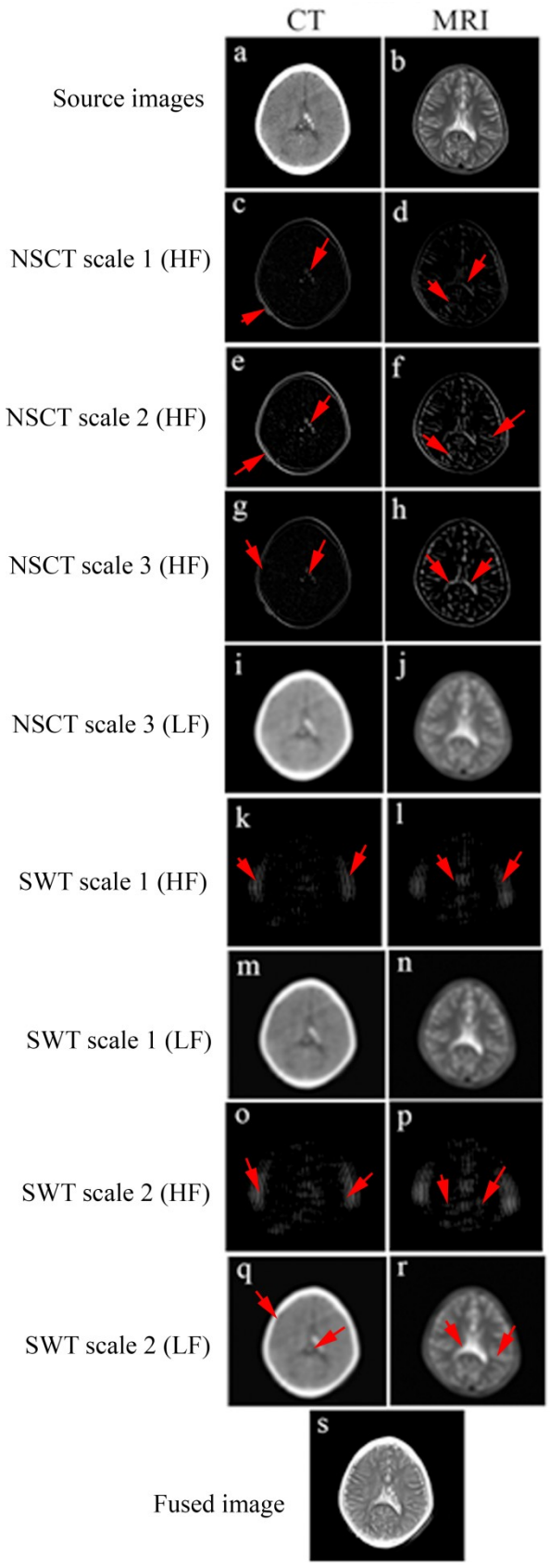

Figure 5.10 Stepwise decomposition results of the proposed algorithm for one pair of calcified brain tumor images. The edges and textures of different subband images as indicated by arrows contribute in fusion

5.10(i,j). A high pass sub-band of SWT decomposition at stage 1 is shown in Figure 5.8(k,l), Figure 5.9(k,l) and Figure 5.10(k,l). The approximation sub-band of SWT at stage 1 is represented by Figure 5.8(m,n), Figure 5.9(m,n) and Figure 5.10(m,n). An HF sub-band of SWT at the second stage is represented by Figure 5.8(o,p), Figure 5.9(o,p) and Figure 5.10(o,p). These steps extract the detail information and point edges from the approximation sub-band of NSCT. The arrows in these figures highlight the salient features that contribute in fusion. The second stage approximation sub-band of SWT is shown in Figure 5.8(q,r), Figure 5.9(q,r) and Figure 5.10(q,r). The final fused images are shown in Figure 5.8(s), Figure 5.9(s) and Figure 5.10(s). The resolution of the images in Figure 5.8(k,l,o,p), Figure 5.9(k,l,o,p) and Figure 5.10(k,l,o,p) have been increased for better visibility of the image details.

5.4 EXPERIMENTAL SETUP

The proposed methodology is implemented in Matrix lab R2015a, is tested on CT and MR images of size 256×256. The experiments are done on Intel core i5 computer with 8 GB memory. The experimental set up has four sets of experiments for testing the performance of the hybrid fusion method.

Experiment 1: Comparison of the presented scheme- a hybrid combination of NSCT and SWT with five other schemes qualitatively on two datasets taken from:
(i) Internet repository (ii) PGIMER.

Experiment 2: Comparison of proposed methodology- a hybrid combination of NSCT and SWT with different methods through parametric evaluation.

Experiment 3: Average quantitative comparison of the proposed scheme with other schemes using primary (PGIMER) and public datasets.

Experiment 4: Quantitative evaluation of the proposed method with various fusion schemes for the dataset obtained from www.imagefusion.org. The quantitative data directly collected from the literature.

The proposed scheme is compared with five recent fusion methods namely (i) adaptive sparse representation (ASR) based scheme [141] (ii) non-subsampled shearlet transform (NSST) based scheme [94] (iii) NSST based scheme [3] (iv) NSST based scheme [142] (v) NSST based scheme [143].

5.4.1 Evaluation Criteria

The proposed algorithm is evaluated by qualitative and parametric means explained as follows:

5.4.1.1 Qualitative analysis - visual interpretation by the radiologist

Visual quality analysis of the fused images is done by the author and two expert radiologists. The tables with filled reviews of the radiologists are given in section 5.5.1.1 (under results and discussions).

5.4.1.2 Quantitative analysis- parametric evaluation

The experiments are qualitatively evaluated using the following parameters

Mutual information (MI), standard deviation (SD), edge information-based quality metric ($Q^{AB/F}$), spatial frequency (SF) and mean.

5.4.2 Analysis of Effect of Decomposition Scale and Direction

The experiments are performed to find the effect of levels of decomposition and directions for NSCT using the proposed fusion scheme. Various parameters such as entropy, spatial frequency, standard deviation, edge information, mutual information and mean are computed for 10 pairs of the public dataset. The decomposition levels are varied from 1,2,3 and 4 and no. of directions at these levels are varied in the powers of 2 as [4], [4,8], [4,8,8] and [4,8,8,16], respectively from coarse to fine-scale. The average value of these parameters for different decomposition levels and directions is represented in Table 5.1 as shown below:

Table 5.1 Effect of Scale and Directions on Fusion Quality Metrics

Quality metric	Levels (d) = 1 and directions (k) = 4	Levels (d) = 2 and directions (k) = 4,8 (from coarse to fine-scale)	Levels (d) = 3 and directions (k) = 4,8,8 (from coarse to fine-scale)	Levels (d) = 4 and directions (k) = 4,8,8,16 (from coarse to fine-scale)
Entropy	4.5242	4.5560	4.6587	**4.7234**
Spatial frequency	26.6980	27.2439	27.5813	**27.6772**
Standard deviation	**84.4226**	84.1864	83.6900	83.1748
Edge information	0.5385	0.5470	0.5585	**0.5603**
Mutual information	**3.7288**	3.6472	3.4320	3.1992
Mean	**66.0084**	65.6400	65.2462	63.4095

From this table, it is seen that out of six assessment parameters three parameters named entropy, spatial frequency and edge information are increasing with an increase in decomposition scale and directions. The parameters such as SD, MI and mean are decreasing with an increase in scale. From visual inspection of the fusion images of different scales and directions as shown in Figure 5.11, it is observed that fusion quality

increases with an increase in scale with directions. However, after scale 3 with directions 4, 8, 8, fusion artifacts are also increasing. Moreover, computational cost also increases with an increase in scale and directions. Keeping in view these facts, a decomposition scale three

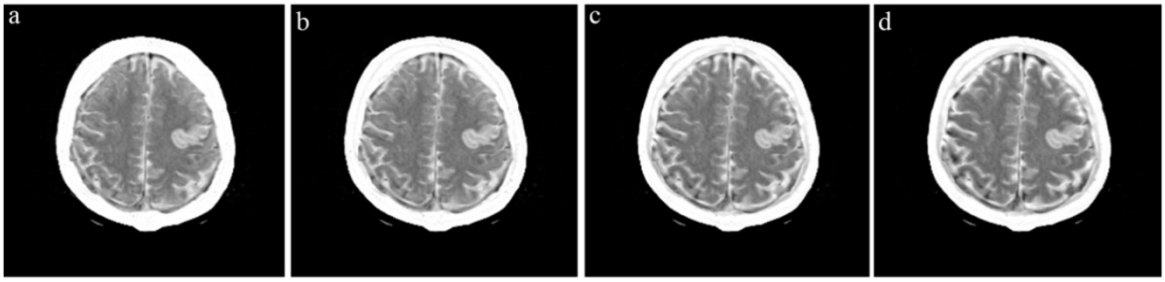

Figure 5.11 Effect of decomposition scale (d) and directions (k) on fusion outcome

(a) d = 1, k = 4
(b) d = 2, k = 4, 8
(c) d = 3, k = 4, 8, 8
(d) d = 2, k = 4, 8, 8, 16

with directions 4, 8, 8 from coarse to fine-scale, respectively is selected in the present research.

5.5 RESULTS AND DISCUSSIONS

5.5.1 Experiment 1: Qualitative Analysis

The three pairs of the publically available dataset and their fusion results are shown in Figure 5.12. Figure 5.13 represents 5 pairs of PGIMER dataset along with comparative fusion results of different fusion schemes.

Figure 5.12(a,b) shows a CT and MR image of acute tumor patient and Figure 5.12(c-h) shows the fusion results of ASR [141], NSST [94], NSST [3], NSST [142], NSST [143] and proposed scheme, respectively, for this image pair. The area of the eye region as indicated by red arrows in Figure 5.12(h) is better seen as compared to other schemes in Figure 5.12(c-g). Similarly, the central portion as indicated by the green arrow in Figure 5.12(h) is seen to have better brightness. Figure 5.12(i-j) represents the source images of a metastatic bronchogenic carcinoma patient. As observed in Figure 5.12(k-p), the contrast of the soft tissues and its homogeneity is better seen in the presented scheme as compared to other schemes. The edema boundary is also better for the proposed scheme (better brightness). Figure 5.12(q-x) shows a case of cerebrovascular disease (hypertensive encephalopathy) and its comparison between various schemes. By a careful look, it is observed that the parenchymal contrast and its homogeneity is better seen in the presented scheme as compared to other schemes. The areas marked by red arrows in Figure 5.12(x) are better

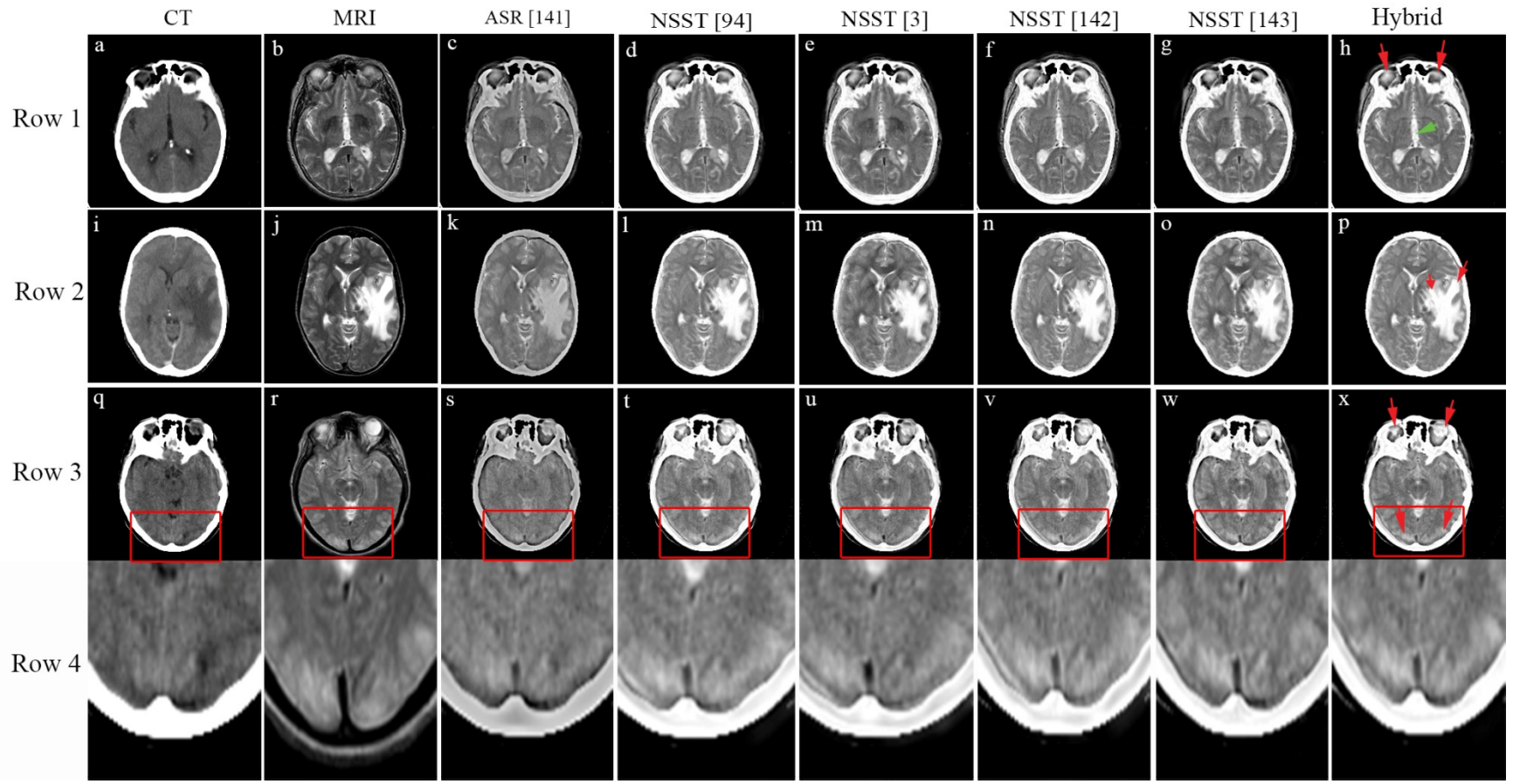

Figure 5.12 Comparative fusion results of three pairs of the publically available dataset

Row 1: Transforms fusion results of a stroke patient
Row 2: Transforms fusion results of metastatic bronchogenic carcinoma patient
Row 3: Transforms fusion results of hypertensive encephalopathy (respective ROI is shown at the bottom row 4)
Row 4: Zoomed images of regions represented by red rectangles in row 3.

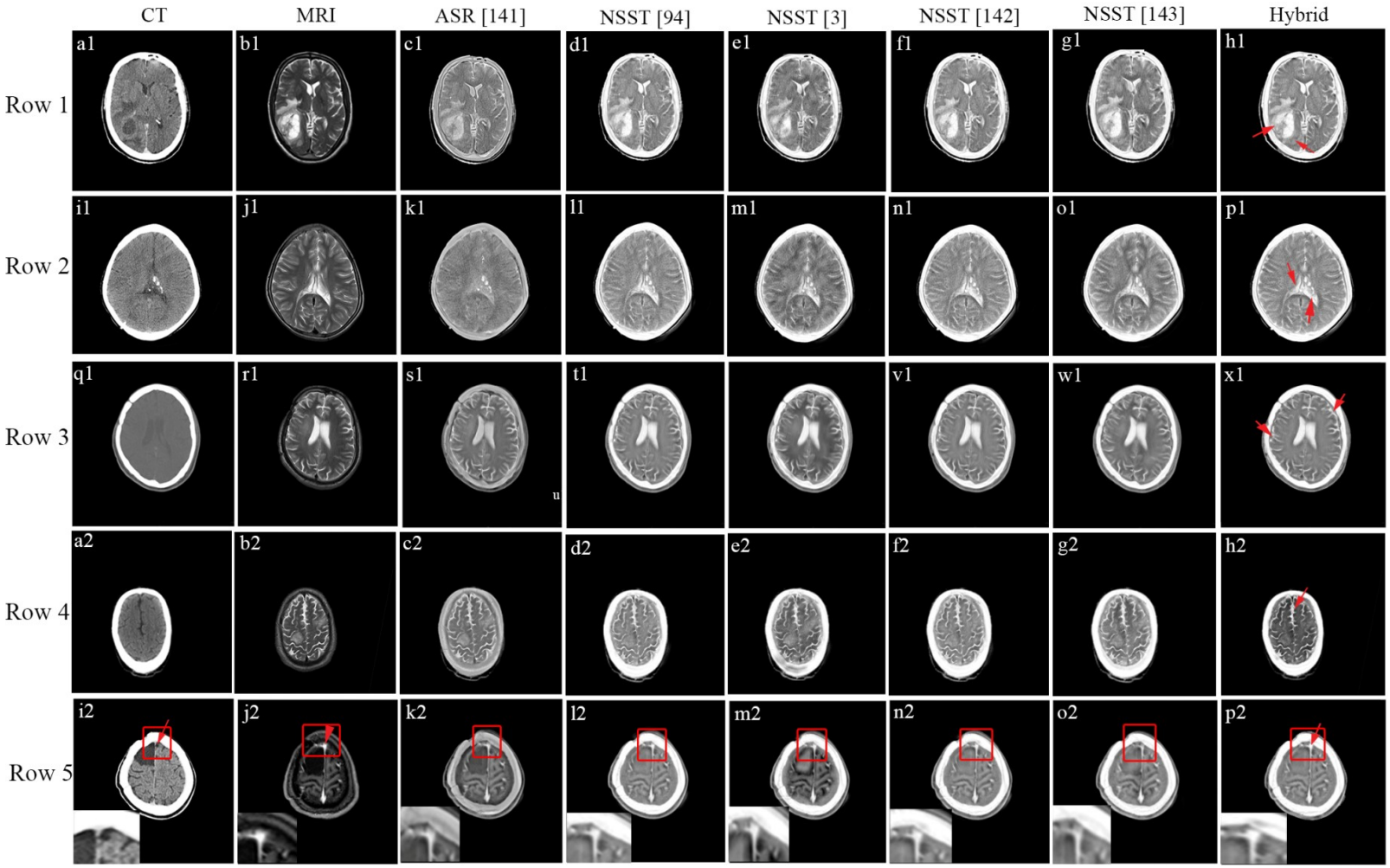

Figure 5.13 Comparative fusion results of five pairs of primary (PGIMER) dataset

Row 1: Transforms fusion results of a glioma patient
Row 2: Transforms fusion results of calcified tumor patient
Row 3: Transforms fusion results of post-operative tumor patient
Row 4: Transforms fusion results of fungal infection patient
Row 5: Transforms fusion results of post operative tumor/ after incision patient along with zoomed ROI on bottom left corner

visible in the proposed scheme. Row 4 of Figure 5.12 shows the respective zoomed image of the area marked by a rectangle in Figure 5.12(q-x). These magnified images better differentiate the proposed scheme from other schemes and verify the superiority of the presented scheme. Figure 5.13(a1-h1) shows a CT and MR image of a glioma patient and comparative visual results of various fusion methods for this pair. After comparing fused images of various schemes it is seen that the brightness, contrast, and texture of lesion and edema are better seen in the fused image of the proposed scheme as marked by the red arrows in Figure 5.13(h1). Figure 5.13(i1-p1) shows source images of a case with calcified tumor and comparison results of different schemes with the proposed scheme. It is observed from these results that the parenchymal changes as indicated by red arrows in Figure 5.13(p1) are better seen (better smoothness of parenchymal texture) in the fused image of the proposed scheme. The calcification information in Figure 5.13(p1) is also comparable with calcification information carried by other compared schemes. Figure 5.13(q1-x1) shows another image pair and its performance comparison. As pointed by the arrows, the brightness of CSF is better seen in this area of the fusion image of the presented scheme as compared to other schemes. Figure 5.13(a2,b2) shows CT and MR image of a fungal infection case, respectively. The proposed scheme shows an improvement in textural contrast of the parenchymal region and the brightness of the CSF as compared to other schemes as shown in Figure 5.13(c2-h2). Figure 5.13(i2, j2) shows postoperative tumor/ after incision image pair. Figure 5.13(k2, l2) appears better, in this case, however, the postoperative cavity as marked by the red arrow in Figure 5.13(p2) is better represented by the proposed methodology as compared to other methods (better size of the lesion). The zoomed image of the area marked by the square box is shown at the bottom left corner of each fusion image for this image pair. From the zoomed region, the difference between the proposed scheme and the other schemes is better visible.

5.5.1.1 Qualitative analysis - visual interpretation by the radiologists

The fused images are shown to two expert neuro-radiologists. Table 5.2 represents a qualitative analysis of the proposed methodology in terms of visual interpretation of the expert radiologists for the PGIMER dataset. Table 5.3 represents the radiologist's perspective of fusion results. The expert's evaluation and their comments are recorded in this table.

Table 5.2 Qualitative Analysis in Terms of Visual Interpretation by the Radiologists

Dataset	Modality	Pathology	Image characteristics (CT, MRI, fused image)
Figure 5.13(a1, b1, h1)	CT and axial T2 weighted MR image	A brain tumor/ glioma	CT represents the existence of a focal lesion in the right occipital lobe with the central hypodense region and peripheral enhancement. The hypodense region around the lesion is parenchymal edema. Similar section T2 weighted MR image better depicts the lesion definition and adjoining perilesional edema. The fusion image generates a composite image giving precise CT and MR characteristics of the lesion with respect to size, character, perilesional edema and distance from the overlying skull bone (which was poorly seen on CT image).
Figure 5.13(i1, j1, p1)	CT and axial T2 weighted MR image	Calcified tumor	The axial CT section shows calcification along the left ventricle (hypodense). The adjoining brain parenchymal changes are not well appreciated. The corresponding T2 weighted MR image requisitely details the parenchymal changes in the brain while the illustration of the calcification is poor. The composite/fused image gives a unique mix of information derived from both CT and MR images in a single image.
Figure 5.13(q1, r1, x1) and Figure 5.13(a2, b2, h2)	CT and axial T2 weighted MR images	A postoperative tumor and fungal infection	There is adequate information of the normal brain and overlying skull derived from CT and MR individually in the form of a distinct fused CT-MR image.
Figure 5.13(i2, j2, p2)	CT and axial Gadolinium-enhanced T1 weighted MR image	A postoperative tumor / after incision	The CT scan image shows a brain parenchymal defect in the right frontal lobe following surgery. Note that the relationship with the bone is very well evident while that with the adjoining superior sagittal sinus is not clear (arrow). The latter information is better seen in the Gadolinium-enhanced T1 weighted MR image (arrowhead) where the bony detail is compromised. The CT-MR fusion image brings out both these characteristics well.

Table 5.3 Radiologist's Perspective of Fusion Results

Radiologist evaluation	Decision on visual analysis (accurate/non-accurate)	Comments by Radiologists	Information profit after visualization
Radiologist 1	Accurate	1. In the case of the different planar orientation of the CT and MRI images, rotation correction, if present, will be useful. 2. Fusion has entailed a slight reduction in the resolution of the images. 3. A better and robust mechanism for motion correction may prove useful for better image fusion.	1. It is easier to see for both MR and CT characteristics on a single fused image, thereby reducing the time of evaluation. 2. The distinction between calcification, hemorrhage and other soft tissue type is better identified. 3. It is a wonderful medium for teaching graduate and postgraduate students regarding brain anatomy.
Radiologist 2	Quite accurate	1. Texture (graininess) improvement is desired which may increase the diagnostic yield. 2. MR signal/ CT attenuation character is slightly compromised in the fusion images.	1. Fusion has helped to generate a composite image. 2. It has reduced diagnostic time. 3. The diagnostic yield has also improved.

5.5.2 Experiment 2: Quantitative Analysis- Parametric Evaluation

Table 5.4 and Table 5.5 shows a quantitative comparison of the hybrid algorithm with five recent fusion schemes for the images shown in Figure 5.12 and Figure 5.13, respectively. These tables represent that the proposed scheme obtains a higher value of MI for most of the cases as compared to other schemes. The higher value of MI indicates that the proposed scheme transferred a higher amount of source information to the fused image as compared to other schemes. The edge information based quality metric, standard deviation, and spatial frequency are highest for the proposed scheme for most of the cases. This indicates that the proposed fusion scheme preserves the detail edge information, contrast, and clarity of the fused images in comparison to the other state of the art schemes. Mean is highest for the proposed hybrid scheme except for the NSST [142] and NSST [94] based schemes. This retains the comparable amount of brightness in the fused image of the hybrid scheme.

Table.5.4 Parametric Comparison of 03 Image Pairs of the Public Dataset as Shown in Figure 5.12

Parameter	Dataset	CT Image	MR Image	ASR [141]	NSST [94]	NSST [3]	NSST [142]	NSST [143]	Hybrid scheme
MI	#1	-	-	3.0049	3.2109	3.2064	3.2268	3.1980	**3.3147**
	#2	-	-	2.9552	3.1525	3.1098	3.1461	3.1456	**3.1927**
	#3	-	-	2.7883	2.9355	2.9259	2.9388	2.9265	**2.9534**
SD	#1	79.1704	52.7793	61.9729	81.4568	79.2167	81.265	80.5971	**81.954**
	#2	70.1809	64.5038	61.9448	81.9723	78.8147	81.941	80.6210	**82.1436**
	#3	81.4914	53.2125	63.8682	83.9414	80.9299	83.5469	82.3389	**83.9509**
$Q^{AB/F}$	#1	-	-	0.5286	0.5346	0.5267	0.5417	0.5461	**0.5620**
	#2	-	-	0.5213	0.5511	0.5144	0.5418	0.5661	**0.5786**
	#3	-	-	0.5389	0.5327	0.528	0.5329	0.5365	**0.5531**
SF	#1	27.8922	18.3064	25.1889	28.527	28.5031	28.3822	28.1565	**29.0448**
	#2	24.3686	16.5267	22.0999	25.6277	25.25	25.4554	25.1652	**25.8039**
	#3	**32.0739**	14.8395	27.9845	31.4914	31.2125	31.0893	30.4914	31.7829
Mean	#1	53.51	40.3945	47.5659	61.9154	59.131	**61.9298**	59.5565	61.2820
	#2	50.7352	41.6016	47.011	60.7027	56.9469	**60.7209**	58.9576	60.4504
	#3	52.3944	36.9295	45.5754	**59.0419**	56.3138	59.0263	57.3811	58.4913

Table.5.5 Parametric Comparison of 05 Pairs of PGIMER Dataset as Shown in Figure 5.13

Parameter	Dataset	CT Image	MR Image	ASR [141]	NSST [94]	NSST [3]	NSST [142]	NSST [143]	Hybrid scheme
MI	#1	-	-	3.0198	3.1849	3.1512	3.1810	3.1952	**3.1967**
	#2	-	-	2.8952	3.0168	2.9757	2.9788	2.9534	**3.0270**
	#3	-	-	2.5760	2.6953	**2.8335**	2.6403	2.6424	2.6709
	#4	-	-	2.4268	2.6603	2.653	2.665	2.6612	**2.6720**
	#5	-	-	2.2817	2.2879	**2.3926**	2.2567	2.2049	2.2478
SD	#1	76.8345	58.6737	65.2152	83.0698	78.9053	83.0536	81.836	**83.0798**
	#2	75.6037	39.4586	61.5986	79.0121	74.8508	**79.1425**	77.4587	79.1198
	#3	66.4532	44.2659	53.2096	**70.2895**	67.1624	70.0713	68.9687	70.2170
	#4	**78.0827**	48.3614	56.1055	76.5184	72.1336	76.337	75.2184	76.2880
	#5	66.2443	30.7472	50.8149	67.8525	67.0305	67.5029	67.2127	**67.8576**
$Q^{AB/F}$	#1	-	-	0.5401	0.5318	0.5101	0.5217	0.5268	**0.5407**

	#2	-	-	0.4783	0.494	0.4778	0.4818	0.4887	**0.5151**
	#3	-	-	0.6159	0.6815	0.678	0.6737	0.6807	**0.6818**
	#4	-	-	0.6349	0.6317	0.627	0.6267	0.6418	**0.6456**
	#5	-	-	0.6277	0.6512	0.6055	0.6524	0.6421	**0.6556**
SF	#1	22.2137	23.9834	25.9172	**28.7295**	28.567	28.3886	27.7744	28.601
	#2	15.2685	16.9462	20.4703	24.7078	24.603	24.62	23.5614	**24.7121**
	#3	14.9221	17.0686	17.8726	20.7873	20.5018	20.6858	20.5798	**20.7919**
	#4	**22.7843**	17.2747	18.3756	20.2033	20.1712	20.1162	19.7654	20.2713
	#5	12.9896	14.8819	21.9961	18.1689	**23.474**	17.9431	17.9369	18.019
Mean	#1	52.0104	43.5044	46.8849	**59.0746**	54.8353	58.9309	57.0958	58.59
	#2	39.3603	23.0765	42.1793	52.7746	48.504	52.7456	51.347	**52.8109**
	#3	37.0255	28.4877	31.3453	**40.1143**	37.1953	40.0565	38.8801	39.937
	#4	**51.4746**	32.8802	30.158	40.3336	37.1093	40.283	39.3552	40.1324
	#5	29.9933	12.2048	23.0482	**32.0172**	31.2221	31.9403	31.563	31.9257

5.5.3 Experiment 3: Average Quantitative Comparison of the Proposed Scheme with Five other Schemes

Table 5.6 and Table 5.7 show the average parametric comparison of 10 public datasets and 28 primary datasets, respectively. From the objective analysis of the results of Table 5.6, it is summarized that the proposed method gains 18.20%, 2.81%, 6.92%, 2.63%, and 11.52% higher mutual information than ASR [141], NSST [94], NSST [3], NSST [142] and NSST [143] based methods, respectively. These results assure more information preservation in the fused images. The proposed methodology gains an enhancement in contrast of the fusion outcome by achieving 33.25%, 0.10%, 4.59%, 0.39%, 1.71% increase in SD w.r.t. ASR [141], NSST [94], NSST [3], NSST [142] and NSST [143] based schemes, respectively. Further, the scheme achieves 7.07% and 44.36% improvement in contrast w.r.t. source CT and MR image, respectively. The hybrid methodology shows an improvement in the edge information of the fused image by achieving 5.09%, 3.89%, 9.35%, 4.96% and 5.36% higher value of $Q^{AB/F}$ as compared to the aforementioned fusion methods. Further, the proposed method gains 2.82%, 71.83%, 15.15%, 0.83%, 1.46%, 1.54% and 3.68% higher SF values than the CT, MR image, ASR [141], NSST [94], NSST [3], NSST [142] and NSST [143] based methods, respectively. These results ensure better clarity and activity level in the fusion outcome. The proposed fusion method also obtains 21.33% and 54.25% higher mean value than the CT and MR images, correspondingly.

Further, it achieves 33.07%, 0.16%, 6.50%, 0.19%, and 3.25% higher average brightness levels of the fused images than ASR [141], NSST [94], NSST [3], NSST [142] and NSST [143] based methods, respectively. Table 5.8 shows a comparison in terms of % age parametric improvement by the proposed method w.r.t other methods for the primary dataset (PGIMER). This table indicates that the present hybrid scheme achieves higher values of all the parameters except the SD of CT image, NSST [94] and NSST [142] based schemes as compared to the aforementioned methods.

Table 5.6 Averaged Parametric Comparison of 10 Image Pairs of the Public Datasets

Parameter	CT Image	MR Image	ASR	NSST	NSST	NSST	NSST	HYBRID
MI	-	-	2.9035	3.3382	3.2098	3.3441	3.0775	**3.4320**
SD	78.1612	57.9725	62.8069	83.6045	80.0148	83.3676	82.2839	**83.6900**
$Q^{AB/F}$	-	-	0.5315	0.5376	0.5108	0.5322	0.5301	**0.5585**
SF	26.8240	16.051	23.9530	27.3541	27.1849	27.1623	26.6032	**27.5813**
Mean	53.7755	42.2985	49.0307	65.1420	61.2643	65.1223	63.1916	**65.2462**

Table.5.7 Averaged Parametric Comparison of 28 Image Pairs of Primary (PGIMER) Dataset

Parameter	CT Image	MR Image	ASR [141]	NSST [94]	NSST [3]	NSST [142]	NSST [143]	HYBRID
MI	-	-	3.0350	3.1935	3.0908	3.0855	3.0498	**3.2479**
SD	**77.6923**	49.5158	60.7169	76.4860	73.7559	77.0820	75.7780	76.2225
$Q^{AB/F}$	-	-	0.5770	0.5557	0.5484	0.5515	0.5521	**0.5783**
SF	17.4735	18.2406	22.6058	24.1589	24.4862	23.1466	23.4594	**24.5255**
Mean	49.1018	32.2925	41.3688	52.6716	48.4830	50.4146	50.9515	**52.8101**

Table.5.8 Comparison of the Proposed Method in Terms of % age Parametric Improvement - Primary Dataset (PGIMER)

Parameter	CT Image	MR Image	ASR [141]	NSST [94]	NSST [3]	NSST [142]	NSST [143]
MI	-	-	7.01%	1.70%	5.08%	5.26%	6.49%
SD	-1.89%	53.93%	25.54%	-0.34%	3.34%	-1.11%	0.59%
$Q^{AB/F}$	-	-	0.22%	4.07%	5.45%	4.86%	4.74%
SF	40.36%	34.45%	8.49%	1.52%	0.16%	5.96%	4.54%
Mean	7.55%	63.54%	27.66%	0.26%	8.92%	4.75%	3.65%

5.5.4 Experiment 4: Quantitative Comparison of the Presented Scheme with Various Classical Fusion Schemes Directly from the Literature

The proposed method is also evaluated with a few existing methods available in the literature directly. The dataset used by these methods is the same as used in the proposed algorithm i.e. obtained from www.imagefusion.org. The parametric analysis of the proposed method with these methods is shown in Table 5.9. The differences in the numbers are relatively large here as compared to the differences in Table 5.6 and Table 5.7. This is due to the MSD transformation employed along with the fusion rules used with them. This analysis shows the improved performance of the proposed scheme in comparison to other schemes.

From the discussion in Experiment1, it is summarised that the proposed methodology notably incorporates visual information of bone, underlying soft tissues or abnormality details in a single fused image. These visual results are also verified by medical experts. The fused images of the proposed scheme can be utilized in clinical applications. On the basis of Experiment 2, it is evident that the proposed hybrid method outperforms ASR and various NSST based recent fusion schemes for most of the cases in terms of MI, SD, $Q^{AB/F}$, SF and mean factors to a better extent. From Experiment 3 it is summarised that the average % age boost in MI, SD, $Q^{AB/F}$, SF and mean parameter for 38 pairs of images is highest for the proposed scheme as compared to the other methods for most of the parameters. This proves the superiority of the proposed algorithm for the fusion of medical images. From

Table 5.9 Comparison of the Proposed Method with Various Existing Fusion Schemes

Fusion Scheme	MI	$Q^{AB/F}$	SD	SF	Mean
NSCT based scheme [85]	---	0.7641	57.1968	---	55.8929
Complex wavelet-based scheme [76]	---	0.5835	32.7685	---	---
NSCT and SWT based hybrid scheme with two (4,8) decomposition levels [100]	---	0.569	---	---	---
NSCT and SWT based hybrid scheme with 3 (4,8,8) decomposition levels [100]	---	0.683	---	---	---
Framelet based scheme [38]	1.8503	0.6772	---	6.5834	51.065
NSCT based scheme [84]	1.4899	0.5931	---	---	---
Contourlet based scheme [137]	---	---	53.82	6.5575	---
NSCT based scheme [92]	**4.83**	0.7771	**65.8646**	6.9434	---
NSST based scheme [94]	4.155	---	62.17	---	---
Weighted least squares filter method [144]	3.788	0.777	---	---	---

Proposed scheme	4.3780	**0.7780**	58.0671	**17.4186**	**56.0674**

Experiment 4 it is clear that the proposed methodology gave improved quantitative parameters except for SD as compared to other schemes in comparison.

5.6 CONCLUSIONS

There are very few researches that investigate the effect of mixing two multi-resolution transforms. Therefore, in the present research work, the fusion of CT and T1-weighted & T2-weighted MR images is performed in a hybrid way by considering complementary characteristics of NSCT and SWT. The weighted sum of the square of the coefficients within a local window-based fusion rule with consistency verification is tested with detail sub-bands of the NSCT. This assures better contrast and clarity in the fused image. The LF sub-band of NSCT is fused through SWT. The maximum entropy of the square of the coefficients and WSML based fusion rules are applied with SWT. Processing NSCT through SWT using the aforementioned rules gives improved edge information and comparable texture in the fused image. The developed scheme is compared with five classical fusion schemes as well. From the qualitative results, it is concluded that the developed method retains parenchyma, disease morphology, CSF information and bony details of the source images with good resolution. From the subjective and parametric analysis, it is observed that the proposed scheme improves mutual information, contrast, edge information, mean brightness level, overall activity, and clarity of the fused image. The proposed method aids the radiologists in surgical procedures as the distance to the diseased tissues from the overlying skull bone is clearly visible in the fused image.

CHAPTER 6

FUSION USING NSST, THE SUM OF GAUSSIAN WEIGHTED PIXEL INTENSITIES AND SUSAN

6.1 INTRODUCTION

An image containing bone and parenchymal details of the brain is preferred by the neuro-radiologists as many diagnostic tasks such as lesion delineation, computer-assisted neurosurgery, radiation therapy planning and brachytherapy treatment planning can be performed more easily using it [3, 11, 45, 145]. Hence, new fusion algorithms are proposed which can address the real-time requirements of the radiologists. To achieve these goals many authors have proposed fusion approaches using different techniques. Adaptive sparse representation (SR) fusion method is proposed in [141], however, this scheme has a very high computational complexity. Moreover, SR based methods are very sensitive to registration inaccuracies and have limited capability of edge preservation [146]. Recently convolutional neural networks (CNN) are utilized in fusion [147] however, CNN-based schemes are computationally slow which is a limiting factor in real-time image processing. Greyscale wolf optimization and hybrid cuckoo search grey wolf optimization techniques are utilized in existing researches [148, 149] however, their fusion outcomes suffer from inadequate bone information. Morphological component analysis and structure tensor-based fusion are done in the NSST domain [88, 150], though, these schemes are quite time-consuming and suffer from poor bone contrast, respectively. Morphological gradient motivated PCNN is used with NSST in chapter 4 however, PCNN based fusion rule increases its computational complexity. It is observed from these methods that either the fusion rules or the fusion techniques increase the computational complexity of fusion algorithms, rendering them less suitable for real-time practical applications.

To address the issue of computational complexity and to preserve the bone, cerebrospinal fluid (CSF), calcification and abnormality information, a faster NSST based fusion methodology is presented in this chapter. To obtain the fusion outcome, the sum of average Gaussian weighted local pixel intensities and smallest uni-value segment assimilating nucleus (SUSAN) based activity measures are employed with low frequency (LF) and high frequency (HF) sub-bands of NSST, respectively. The SUSAN-based method finds the pixels having edge information from HF subbands of NSST whereas, the Gaussian

weighted pixel intensity method computes the Gaussian weighted intensity of LF subband pixels. The pixels with higher values of these measures are selected to form the fused image. These rules are not explored with NSST as per the knowledge of the author. The presented methodology is compared with five recent fusion algorithms using five performance parameters. The scheme is also compared scientifically with other schemes using Wilcoxon signed ranks test [151]. The details of the proposed methodology are given as follows:

6.2 METHODOLOGY

The methodology section gives elaborated information about the proposed scheme. It contains the image pre-processing and NSST decomposition. This is followed by the LF and HF coefficients fusion and composite image reconstruction. Figure 6.1 shows the block diagram of the proposed sum of average Gaussian weighted local pixel intensities and SUSAN based fusion methodology. The detailed descriptions of the steps followed in the fusion process are given as follows:

6.2.1 Image Decomposition

The registered source images are decomposed into LF and HF sub-bands using NSST. A brief introduction to the decomposition process of NSST is already given in section 4.2.2 of Chapter 4. In the presented research one level of NSST decomposition is employed with 2 directional sub-bands. It is observed that increasing the decomposition levels does not increase the visual results of the fused images of the proposed scheme, whereas, it increases the computational complexity. As the decomposition levels are increased the SUSAN operator is not able to efficiently capture the bigger features due to its inherent property of detecting the small objects. LF sub-bands of NSST decomposition of CT and MR images are fused using the local sum of Gaussian weighted pixel intensities based fusion rule, whereas, HF sub-bands are fused using SUSAN feature extraction based fusion rule. These rules are used as they compute the activity coefficients in a faster manner. These activity measures are discussed in detail in the following subsections.

6.2.2 LF Sub-Band Fusion

The LF sub-band contains the smoothed version and outline of the original image hence, LF sub-band activity measure is computed using the local sum of average Gaussian weighted pixel intensities within a 3×3 neighborhood as follows:

$$G(Z_{Low}(m,n)) = \sum_{i=-1}^{1}\sum_{j=-1}^{1} W \times Z_{Low}(m+i, n+j) \tag{6.1}$$

where Z_{Low} and $G(Z_{Low})$ represent LF sub-band of NSST and Gaussian mask based activity measure for image A (A_{Low}) or image B (B_{Low}), respectively.

W [3] is represented by eqn.6.2 as follows:

$$W = \frac{1}{16} \times \begin{bmatrix} 1 & 2 & 1 \\ 2 & 4 & 2 \\ 1 & 2 & 1 \end{bmatrix} \tag{6.2}$$

The Gaussian mask W is used because its response matches the response of the human visual system to different features in the image. This activity measure is used to compute

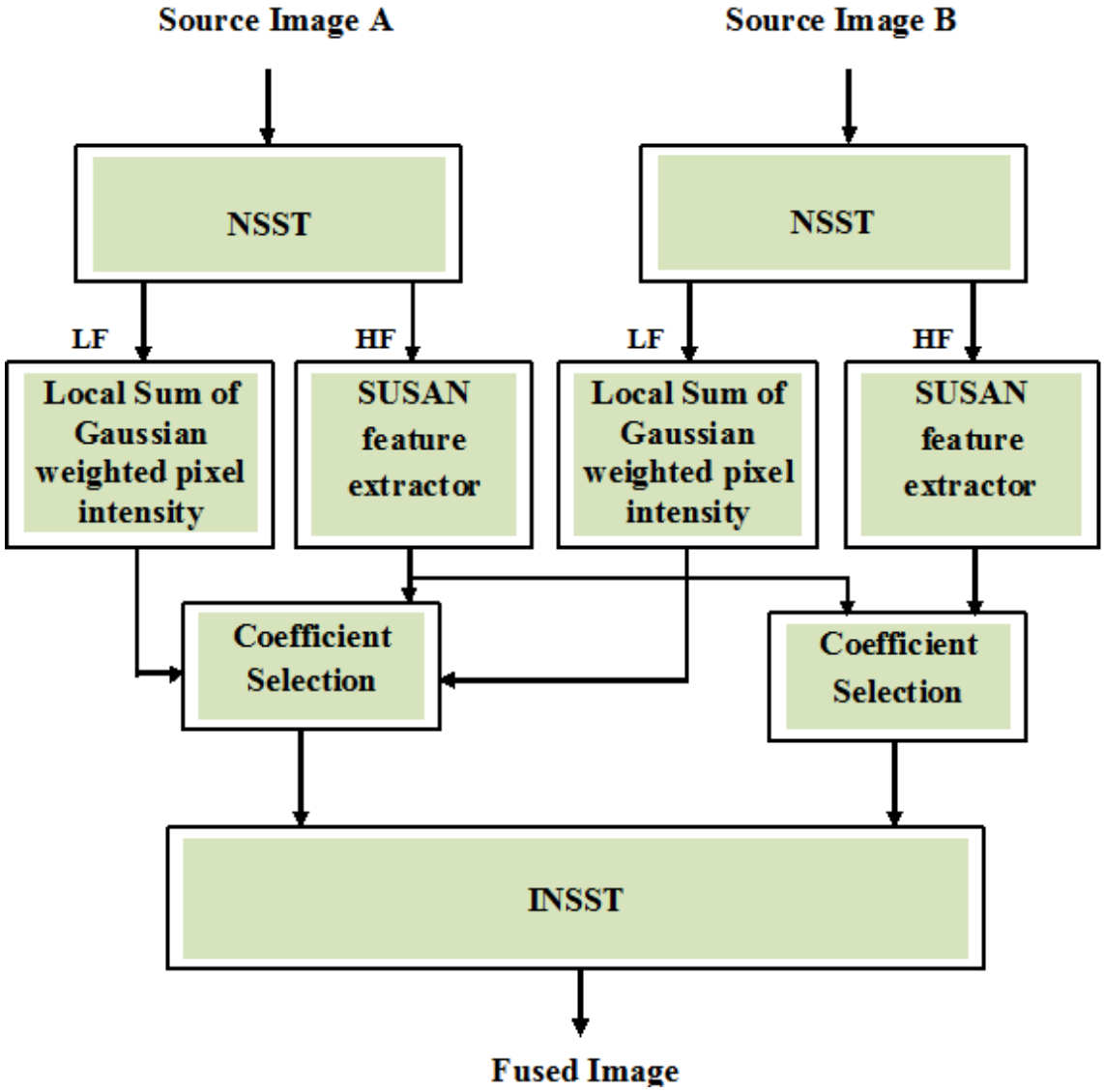

Figure 6.1 Block diagram of the proposed local sum of average Gaussian weighted pixel intensity and SUSAN based fusion methodology

the decision map which is used in the fusion of LF sub-band coefficients and is expressed as:

$$d(m,n) = \begin{cases} 1 & \text{if} \quad G(A_{Low}(m,n)) \geq G(B_{Low}(m,n)) \\ 0 & \text{Otherwise} \end{cases} \tag{6.3}$$

The decision map as expressed in eqn. 6.3 is used to select the coefficients of LF subbands of input images having maximum local Gaussian weighted activity level in the fusion image. This step represents the left-hand side coefficient selection block of Figure 6.1. The fused approximation coefficients $F_{Low}(m,n)$ are computed as follows:

$$F_{Low}(m,n) = \begin{cases} A_{Low}(m,n) & \text{if} \quad d(m,n) = 1 \\ B_{Low}(m,n) & \text{if} \quad d(m,n) = 0 \end{cases} \tag{6.4}$$

6.2.3 HF Sub-Band Fusion

The detail sub-bands contain edge and corner information hence, this research applies SUSAN based feature extractor for the fusion of HF sub-bands of NSST decomposition of source images.

Smallest uni-value segment assimilating nucleus (SUSAN) edge extraction: Smallest uni-value segment assimilating nucleus is a human visual system motivated edge and feature extraction model proposed by [152]. However, its suitability with NSST in image fusion is still underexplored. It is noted from [152] that SUSAN extractor is very fast in computing features and edge information from images. Hence, the proposed scheme makes the benefit of this fact. In order to extract features a circular mask with the center pixel known as a nucleus is placed at each pixel in the image. The nucleus intensity is compared with every pixel of the image under the mask. If the intensities are similar then the area is marked and is named as the uni-value segment assimilating nucleus (USAN) [152]. A map of the features detected using this comparison is expressed as follows:

$$map(\vec{r},\vec{r}_0) = \begin{cases} 1 & \text{if} \quad G(\vec{r}) - G(\vec{r}_0) \leq T_h \\ 0 & \text{if} \quad G(\vec{r}) - G(\vec{r}_0) > T_h \end{cases} \tag{6.5}$$

where $\vec{r}_0$ represents the 2-dimensional coordinates of the nucleus and $\vec{r}$ represents a pixel under the mask. $G(\vec{r})$ represents the gray level at the location $\vec{r}$ and T_h is the intensity difference threshold [38]. In this research, the brightness difference threshold is set as 20.

The map as expressed in eqn.6.5 is used to compute the sum of pixel intensities $S(\vec{r}_0)$ in USAN which is expressed as:

$$S(\vec{r}_0) = \sum_{\vec{r}} map(\vec{r},\vec{r}_0) \tag{6.6}$$

The edge response is computed using the following expression:

$$E_R(\vec{r}_0) = \begin{cases} T_f - S(\vec{r}_0) & \text{if} \quad S(\vec{r}_0) < T_f \\ 0 & \text{otherwise,} \end{cases} \tag{6.7}$$

where, T_f is a geometric threshold computed as $T_f = 3S_{max}/4$ and S_{max} is the maximum value of S. Eqn.6.7 shows that the smaller the $S(\vec{r}_0)$ larger will be the edge response. To make the edge and corner detection less responsive to T_h, USAN operation considers not only the intensity similarity between pixels but also the distance between them [38]. The resulting map is expressed as follows:

$$map(\vec{r},\vec{r}_0) = \exp\left(\frac{-(\vec{r}-\vec{r}_0)^2}{2\delta^2}\right)\exp\left(-\left(\frac{G(\vec{r})-G(\vec{r}_0)}{T_h}\right)^6\right) \tag{6.8}$$

where, δ is the distance scaling factor. The feature extraction process involves no derivatives which ensure better edge and corner detection even in the presence of small noise [38, 152].

SUSAN edge response of images A and B is computed as an activity measure according to eqn.6.7. The decision map to fuse the detail sub-bands $A_{High}(m,n)$ and $B_{High}(m,n)$ is given as follows:

$$d(m,n) = \begin{cases} 1 & \text{if} \quad E_R(A_{High}(m,n)) \geq E_R(B_{High}(m,n)) \\ 0 & \text{Otherwise} \end{cases} \tag{6.9}$$

This map is used to select the coefficient having higher edge information from either of the HF subbands of source images to compute fused HF subbands. This step represents the right-hand side coefficient selection block of Figure 6.1. The fused detail sub-bands are computed as follows:

$$F_{High}(m,n) = \begin{cases} A_{High}(m,n) & \text{if} \quad d(m,n) = 1 \\ B_{High}(m,n) & \text{if} \quad d(m,n) = 0 \end{cases} \tag{6.10}$$

The fused image is reconstructed using inverse NSST (INSST) and is represented by the INSST block in Figure 6.1.

6.3 EXPERIMENTAL SETUP

All the experiments are performed in MATLAB 8.3 in Intel core i5 processor equipped with 8 GB RAM. The developed scheme is correlated with 5 recent classical fusion methods namely: wavelet transform and adaptive block-based scheme (DWTA) [153], SWT based scheme with entropy and sum-modified Laplacian based fusion rules [154], adaptive sparse representation (ASR) and denoising [141], convolutional sparse representation (CSR) based fusion scheme [146], NSST with regional energy and pulse coupled neural network-based

scheme [142]. The following experiments are performed to evaluate the effectiveness of the developed algorithm:

Experiment 1: Qualitative (Visual) analysis and comparison of the proposed scheme with five other fusion schemes using primary and public datasets.

Experiment 2: Quantitative (parametric) analysis and comparison of the proposed scheme with five other schemes using primary and public datasets.

Experiment 3: Wilcoxon signed-ranks test based statistical comparison between the proposed scheme and five other schemes.

Experiment 4: Computational complexity comparison of the developed sum of Gaussian weighted pixel intensities and SUSAN based methodology with other schemes for two different datasets.

6.3.1 Evaluation Criteria

The proposed local sum of Gaussian weighted pixel intensities-SUSAN based fusion scheme is compared visually and parametrically as follows:

6.3.1.1 Visual analysis

The fused images of the developed scheme and other schemes are evaluated in terms of their ability to keep the bone information, CSF, calcification, tumor and edema information of the source images. The contrast, brightness, edge details, clarity, noise and texture information present in the fused images are also noted. The fusion images of the proposed methodology are evaluated in an independent manner by two radiology experts for their clinical usefulness.

6.3.1.2 Parametric analysis

To compare the effectiveness of different fusion schemes five fusion performance parameters are computed. These parameters are mutual information (MI), edge strength-based quality metric, standard deviation (SD), spatial frequency (SF) and mean. The details of these parameters are already given in Chapter 3.

6.4 RESULTS AND DISCUSSIONS

6.4.1 Experiment 1: Visual Analysis and comparative evaluation of the presented scheme with 5 traditional fusion schemes.

Figures 6.2(a-h) show an image pair of metastatic bronchogenic carcinoma patient of the Harvard school dataset and the fusion results of the proposed scheme and other representative schemes for this pair. From these figures, it is observed that the DWTA and CSR based schemes are not able to fuse the adequate details of bone and soft tissues. The hard and soft tissue brightness is not adequate in the ASR scheme. The soft tissue details are

better in the NSST based scheme as compared to other schemes. The zoomed region of the SWT scheme shows the poor overlap of the tissues. This is shown by the magenta color arrows in Figure 6.2(d). The fused image of the proposed scheme shows the adequate details of edema, CSF, bone and better tissue overlap as marked by the magenta color arrows in the zoomed region of Figure 6.2(h). Figures 6.3(a-h) show an image pair and fusion results of different methods of an acute stroke patient having speech arrest. The DWTA and CSR based schemes are not able to fuse the adequate details of bone for this image pair. The contrast of the fused image of the ASR scheme is poor. The bone information in the NSST scheme is compromised as compared to the proposed scheme. The zoomed region of the SWT scheme shows the ribbon-like structure with an intensity inhomogeneous region surrounding it. However, the zoomed region of the proposed scheme shows better homogeneity of the ribbon-like structure and its surrounding tissues. Figures 6.4(a-h) show another image pair and fusion results of different methods of a hypertensive encephalopathy case. The DWTA and CSR schemes show adequate bone information however, soft tissue details are not appropriate. The ASR scheme gives poor bone and parenchyma contrast. The bone details of the NSST scheme are poor as compared to the proposed scheme. The zoomed region of the SWT scheme is shown in Figure 6.5(a) in which poor bone edges are seen near the interface of bone and soft tissues. Moreover, this region suffers from intensity in-homogeneities of soft tissues. The zoomed region of the proposed scheme of Figure 6.4(h) is shown in Figure 6.5(b). By observing Figure 6.5(b) it is clear that the proposed scheme has better bone edges and homogeneity of soft tissues in the surrounding regions.

Figures 6.6(a-h) show the source images and fusion outcome of different methods for an image pair of PGIMER dataset. The DWTA and CSR schemes suffer from bone artifacts as marked in red. ASR method has poor contrast. NSST scheme bone details are slightly compromised as compared to the proposed scheme. The red arrow in the zoomed region of SWT and the proposed scheme indicates that bone information is better in the proposed method. The blue arrow in the zoomed images of SWT and the proposed method shows that the SWT based method has a poor overlap as compared to the proposed method. Figures 6.7(a-h) show the source images of a tumor patient of the PGIMER dataset and the fusion outcome of different methods. The DWTA, ASR and CSR schemes do not fuse the source information properly for this patient. The soft tissue details are better in the NSST scheme in many regions. The difference between SWT and the proposed scheme is seen in the zoomed regions of Figures 6.7(d,h). The proposed method has better tissue homogeneity as

compared to SWT based scheme as marked by the blue arrow in the zoomed region of these methods. Figures 6.8(c-h) show the fused outcome of various schemes for another image pair of PGIMER dataset. The DWTA, CSR and ASR schemes suffer bone distortion in this case as marked in red. Soft tissue contrast is better in the NSST scheme. Figures 6.8(d,h) show the fusion images of SWT and the proposed scheme along with zoomed regions. The SWT scheme also provides better soft tissue details for this patient as compared to the proposed scheme. However, the proposed scheme shows better bone details in the zoomed part of this patient as marked in red.

6.4.1.1 Visual analysis of the developed methodology by the radiologists

Figure 6.2 shows the case of extensive parenchymal edema in a case of metastatic bronchogenic carcinoma. The axial CT image as shown in Figure 6.2(a) demonstrates a diffuse hypo-density signifying edema in the left parieto-occipital lobe reaching uptil the

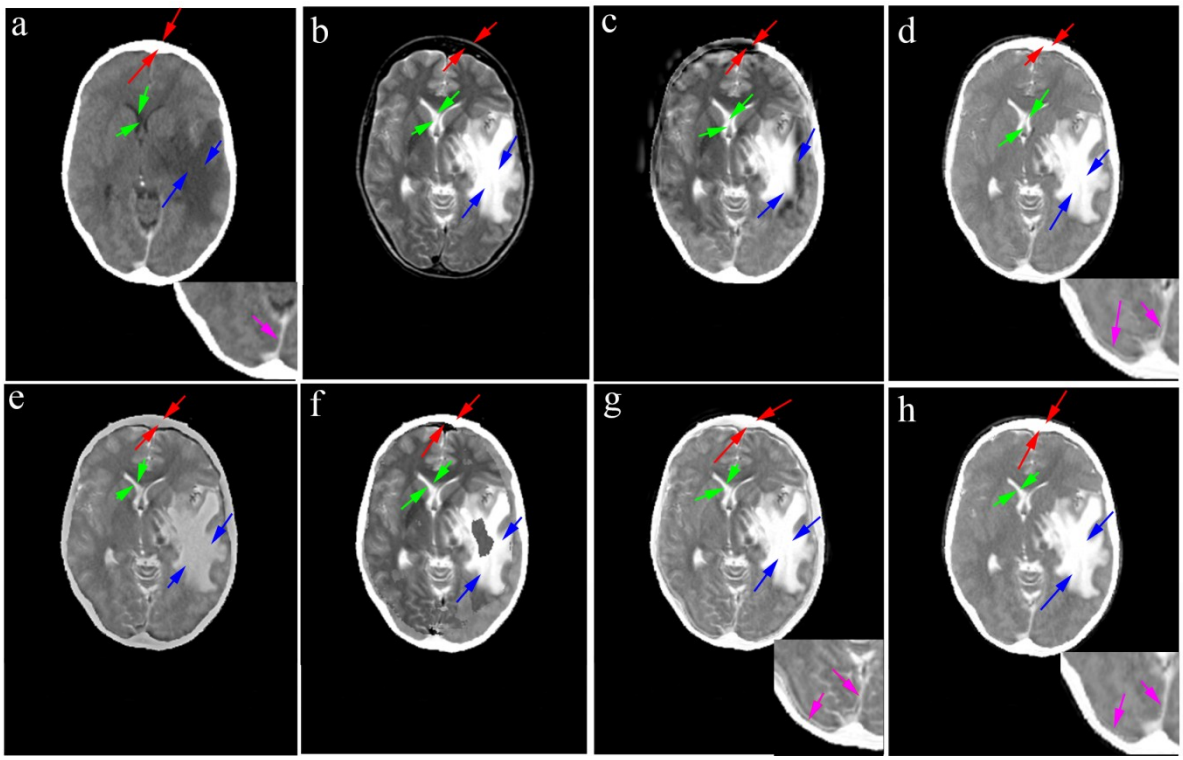

Figure 6.2 Comparative fusion results of diseased- metastatic bronchogenic carcinoma patient

Red pointer: hard tissues (bone), green pointer: CSF, blue pointer: edema
(a) CT image
(b) MRI image
(c) DWT and adaptive block-based scheme (difference with proposed method visible by the naked eye)
(d) Stationary wavelet transform (the difference is shown by the zoomed up region)
(e) Adaptive sparse representation scheme (difference with proposed method visible by the naked eye)
(f) CSR scheme (difference with proposed method visible by the naked eye)
(g) Nonsubsampled shearlet transform (the difference is shown by the zoomed up region)
(h) Proposed NSST-SUSAN scheme (the difference is shown by the zoomed up region)

cortex at places. Its extension is not clearly defined along its margins where it merges into the normal brain parenchyma. The T2 weighted MR image in Figure 6.2(b) gives a better depiction of the extent of the edema in the brain parenchyma. There is an associated mass effect on the surrounding structures. The fused CT-MR image shows the representative details of the lesion on the individual modality in the single combined image as shown in Figure 6.2(h). The lesion nature, its extent, adjoining mass effect and relationship with the bone is better made out. This can help a surgeon in choosing the bony site if a biopsy of the lesion is contemplated. Referring to Figures 6.3(a,b), CT is apparently normal. However, the MR section at the same level shows the presence of T2 hyper-intense signal changes in the left frontal lobe. The fusion image as shown in Figure 6.3(h) gives us detailed information about the same. Figure 6.4(a) and Figure 6.4(b), CT image shows subtle subcortical white matter lesions which are better depicted on the T2 MRI image. Fusion

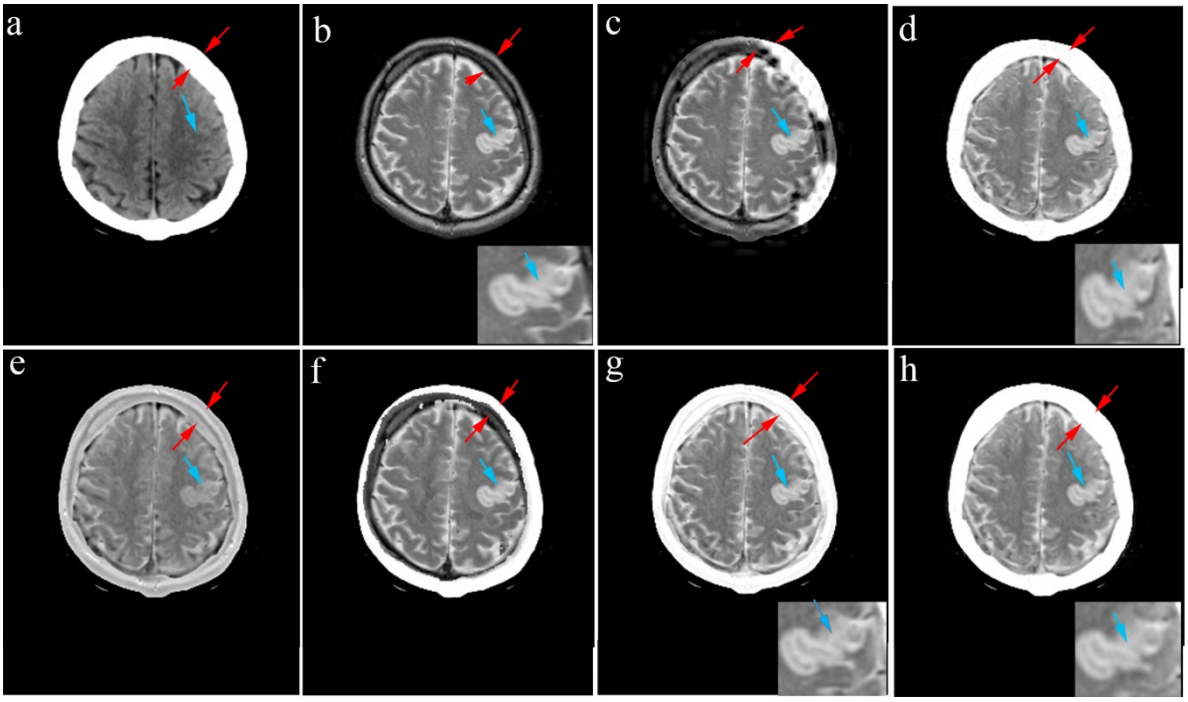

Figure 6.3 Comparative fusion results of diseased- acute stroke (speech arrest) patient

Red pointer: hard tissues (bone), sky blue pointer: infarct
(a) CT image
(b) MRI image
(c) DWT and adaptive block-based scheme (difference with proposed method visible by the naked eye)
(d) Stationary wavelet transform (the difference is shown by the zoomed up region)
(e) Adaptive sparse representation scheme (difference with proposed method visible by the naked eye)
(f) CSR scheme (difference with proposed method visible by the naked eye)
(g) Nonsubsampled shearlet transform (the difference is shown by the zoomed up region)
(h) Proposed NSST-SUSAN scheme (the difference is shown by the zoomed up region)

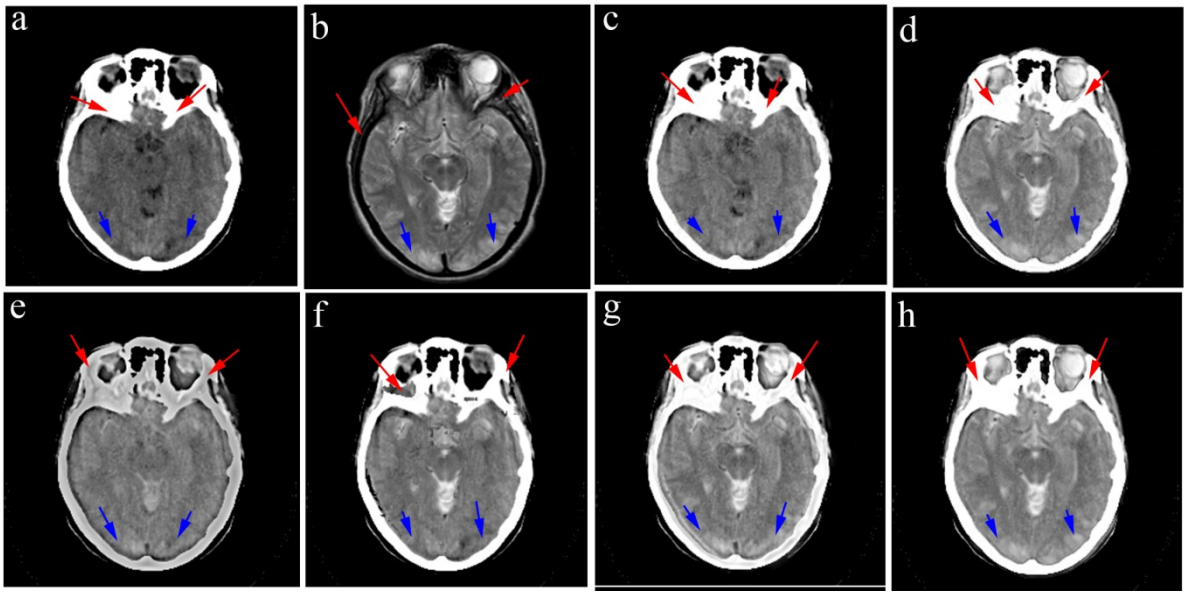

Figure 6.4 Comparative fusion results of diseased- hypertensive encephalopathy patient

Red pointer: hard tissues (bone), blue pointer: lesion
(a) CT image
(b) MRI image
(c) DWT and adaptive block-based scheme
(d) Stationary wavelet transform
(e) Adaptive sparse representation scheme
(f) CSR scheme
(g) Nonsubsampled shearlet transform
(h) Proposed NSST-SUSAN scheme

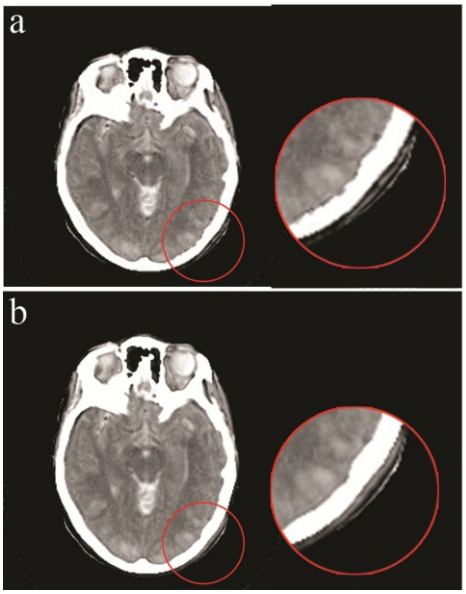

Figure 6.5 Zoomed regions of Figures 6.4(d, h)

(a) SWT scheme
(b) Developed scheme

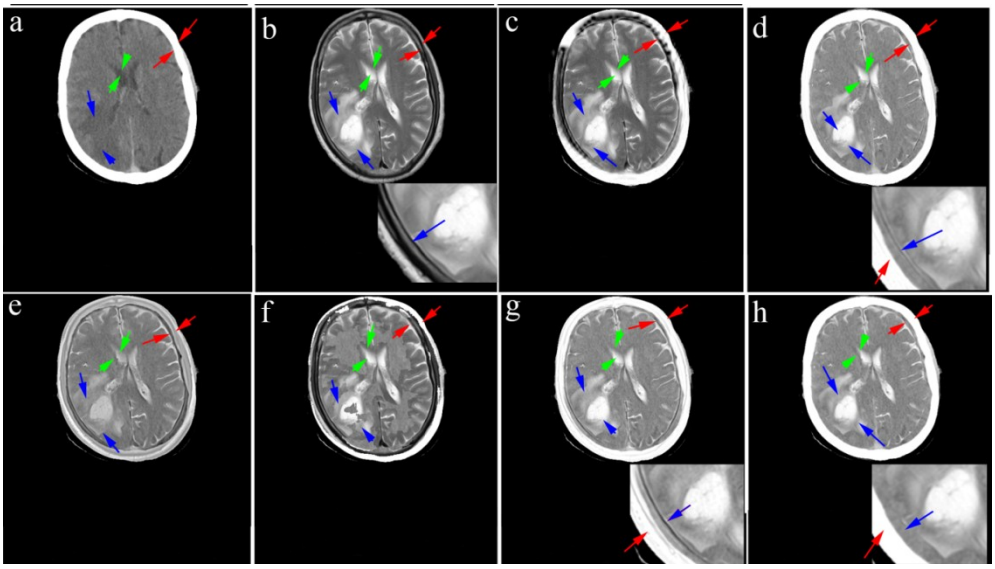

Figure 6.6 Comparative fusion results of diseased- glioma patient

Red pointer: bone, green pointer: CSF, blue pointer: lesion/oedema
(a) CT image
(b) MRI image
(c) DWT and adaptive block-based scheme (difference with proposed method visible by the naked eye)
(d) Stationary wavelet transform (the difference is shown by the zoomed up region)
(e) Adaptive sparse representation scheme (difference with proposed method visible by the naked eye)
(f) CSR scheme (difference with proposed method visible by the naked eye)
(g) Nonsubsampled shearlet transform (the difference is shown by the zoomed up region)
(h) Proposed NSST-SUSAN scheme (the difference is shown by the zoomed up region)

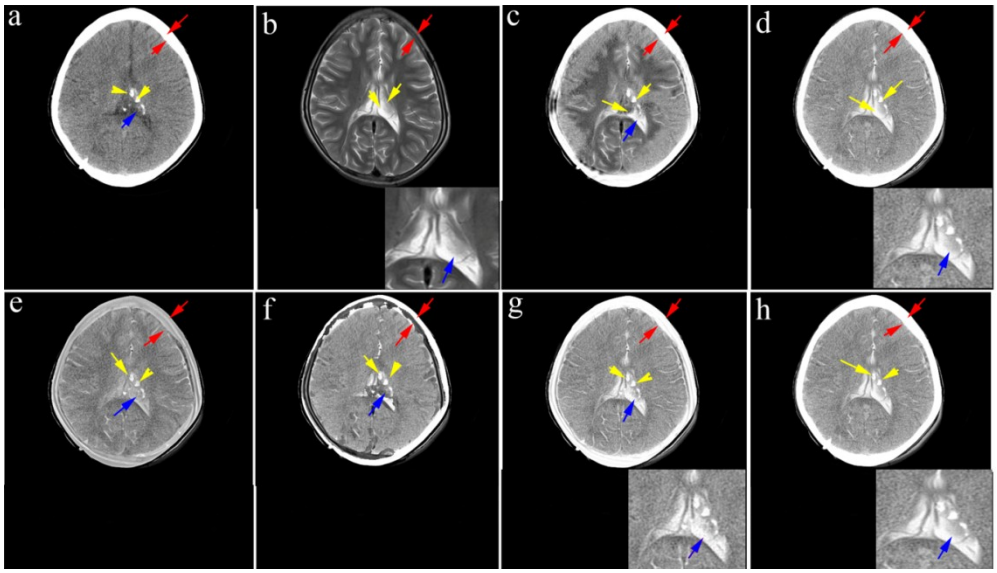

Figure 6.7 Comparative fusion results of diseased- calcified bi-thalamic lesion patient

Red pointer: bone, blue pointer: tumor, yellow pointer: calcified tumor:
(a) CT image
(b) MRI image
(c) DWT and adaptive block-based scheme (difference with proposed method visible by the naked eye)
(d) Stationary wavelet transform (the difference is shown by the zoomed up region)
(e) Adaptive sparse representation scheme (difference with proposed method visible by the naked eye)
(f) CSR scheme (difference with proposed method visible by the naked eye)
(g) Nonsubsampled shearlet transform (the difference is shown by the zoomed up region)
(h) Proposed NSST-SUSAN scheme (the difference is shown by the zoomed up region)

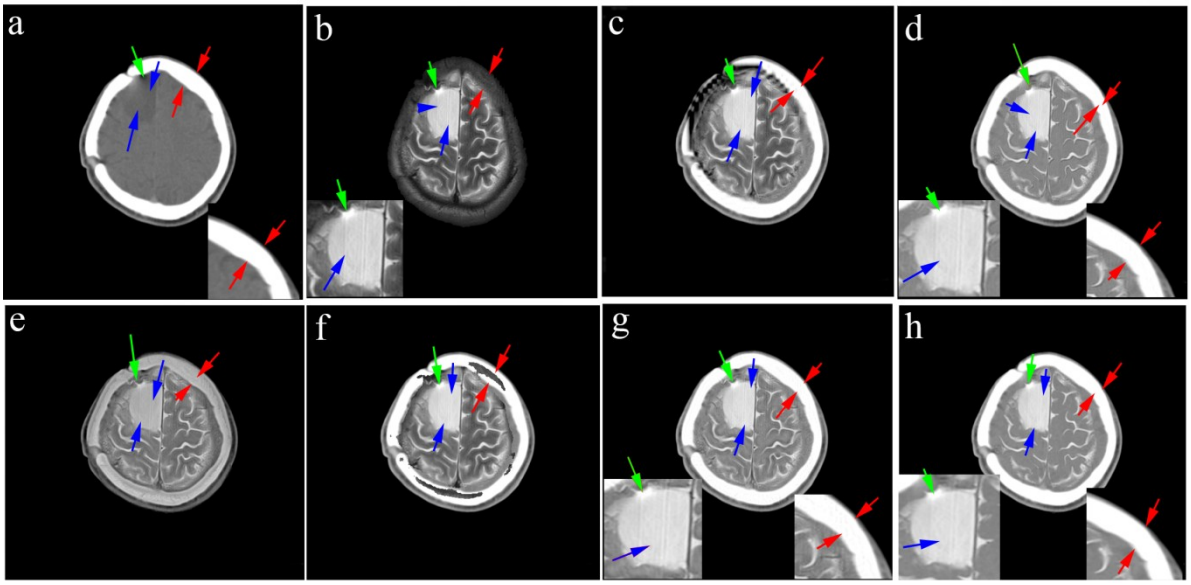

Figure 6.8 Comparative fusion results of diseased- post-operative brain tumor patient

Red pointer: bone, blue pointer: tumor, green pointer: CSF
(a) CT image
(b) MRI image
(c) DWT and adaptive block-based scheme (difference with proposed method visible by the naked eye)
(d) Stationary wavelet transform (the difference is shown by the zoomed up region)
(e) Adaptive sparse representation scheme (difference with proposed method visible by the naked eye)
(f) CSR scheme (difference with proposed method visible by the naked eye)
(g) Nonsubsampled shearlet transform (the difference is shown by the zoomed up region)
(h) Proposed NSST-SUSAN scheme (the difference is shown by the zoomed up region)

image as shown in Figure 6.4(h) better brings out the lesion relationship with the overlying bone. Figure 6.6(a), CT image represents an unclear hypo-density in the right frontoparietal region of a glioma patient. The corresponding MR image as shown in Figure 6.6(b) better depicts the lesion extension. The distinction between the lesion and the surrounding tissues is better visible in the combined image of the developed method as shown in Figure 6.6(h). Figure 6.7(a), CT image shows the presence of a calcified bi-thalamic lesion. However, the soft tissue abnormality is not visible through it. The corresponding MR slice in Figure 6.7(b) gives good details of parenchymal abnormality. Figure 6.7(h), the combined image shows well all these details in it. Figures 6.8(a,b) show the presence of a hypodense lesion in the right frontal lobe on CT in a post-operative case of a brain tumor. This lesion appears hyperintense on T2 weighted MR image. Fusing the CT and MR image demonstrates the lesion to be located close to the overlying bone indicating it to be CSF collected at the postoperative site from where the tumor has been excised.

6.4.2 Experiment 2: Quantitative Analysis and Comparative Evaluation of the Presented Scheme with 5 Traditional Fusion Schemes

The parametric evaluation of the proposed methodology is done using MI, $Q^{AB/F}$, SD, mean and SF parameters as discussed in subsection 4.1.2 under evaluation criteria. The average values of these metrics are computed for 09 pairs of Harvard school dataset and 15 pairs of PGIMER dataset for all the methods and are recorded in Table 6.1 and Table 6.2, respectively. Table 6.1 and Table 6.2 show that for both the medical image datasets average value of MI, SD and mean parameters are highest for the presented methodology as compared to other schemes. This demonstrates better texture, contrast and illumination in the output image of the presented algorithm as compared to DWTA, SWT, ASR, CSR and NSST based schemes. Edge details are highest in the outcomes of the proposed scheme for the Harvard school dataset except for the CSR based scheme. Edge details for the PGIMER dataset are highest for the proposed methodology except for the CSR and ASR based schemes. The average SF parameter for the proposed scheme is better than DWTA, SWT

Table 6.1 Average Parametric Performance of Different Fusion Approaches for 09 Harvard School Image Pairs

Approach	MI	$Q^{AB/F}$	SD	Mean	SF
CT image	-	-	75.2336	44.7729	31.7732
MR image	-	-	45.7445	30.7185	19.0816
DWTA [153]	3.1335	0.4768	79.9773	57.9857	27.1948
SWT [154]	3.5857	0.5188	87.1400	68.5423	27.0385
ASR [141]	2.9217	0.5127	65.3356	50.9769	24.8849
CSR [146]	3.5748	**0.5707**	80.5854	57.1006	**32.4616**
NSST [142]	3.1885	0.5105	86.2884	66.4748	28.4371
Proposed	**3.7406**	0.5346	**88.1506**	**68.5800**	27.4274

Table.6.2 Average Parametric Performance of Different Fusion Approaches for 15 PGIMER Image Pairs

Approach	MI	$Q^{AB/F}$	SD	Mean	SF
CT image	-	-	75.7658	47.1179	14.2992
MR image	-	-	51.1329	29.7843	16.0675
DWTA [153]	2.9272	0.5205	67.5362	40.0323	15.8998
SWT [154]	3.1450	0.5357	79.0337	50.5691	16.3947

ASR [141]	2.5815	0.6120	59.9582	38.8857	17.5368
CSR [146]	3.2605	**0.6476**	63.3983	37.6053	**22.9728**
NSST [142]	2.7899	0.5514	78.4736	50.1011	18.7808
Proposed	**3.5392**	0.5669	**79.7867**	**51.0934**	17.8293

and ASR based schemes. However, it is lesser than the CT, CSR and NSST based schemes for the Harvard school dataset. In the case of the PGIMER dataset, average SF of the fusion images of the proposed scheme is better than CT image, MR image, DWTA, SWT and ASR based scheme. However, it is lesser than CSR and NSST based scheme. By observing the data in these tables it is evident that the presented scheme outperforms other fusion schemes in comparison.

6.4.3 Experiment 3: Statistical comparison using Wilcoxon signed ranks test

Wilcoxon signed-ranks test is used to verify whether a significant difference exists between the population means of the two methods and to find the better method as compared to the other method. It is an alternative to paired t-test with the difference that it does not require the normally distributed data and is less affected by the sample size. Hence, the proposed method is compared statistically with other schemes using this test. All the 24 image pairs of both the medical datasets are used as a single dataset for Wilcoxon signed ranks test. A comparison of the presented scheme with other approaches is done pairwise to scientifically find out the statistical difference between them. The test is performed in the SPSS package and the p values so obtained are recorded in Table 6.3. The results of this test reveal that the p values for all the parameters of all methods are less than 0.05 except the SF parameter of CT image. This shows that a significant difference exists between the proposed scheme and other schemes. The p-value of the SF parameter for CT image is 0.317 which is greater than 0.05 hence, it can't be claimed that a significant difference exists in this case. The proposed method performs better than other methods according to this test. From these results, it is evident that the Wilcoxon test validates the results of parametric comparison done in Experiment 2 for medical image datasets.

Table 6.3 Comparative Analysis of p Values obtained using Wilcoxon Signed Ranks Test

Metric	CT image	MR image	DWTA [153]	SWT [154]	ASR [141]	CSR [146]	NSST [142]
MI	-	-	0.000	0.000	0.000	0.000	0.000
$Q^{AB/F}$	-	-	0.000	0.000	0.046	0.000	0.012

SD	0.000	0.000	0.000	0.000	0.000	0.000	0.000
Mean	0.000	0.000	0.000	0.000	0.000	0.000	0.000
SF	0.317	0.002	0.046	0.003	0.003	0.000	0.000

6.4.4 Experiment 4: Computational Complexity Comparison

The computational efficiency of the proposed fusion scheme and other classical schemes is evaluated by repeating the experiment on each image pair eight times. Table 6.4 shows the average value of the computational cost of all the schemes for Harvard school and PGIMER datasets. By observing the results of this table it is evident that the computational cost of the developed scheme is minimum among all the schemes and is beneficial for practical applications. In view of the discussions in Experiment 1, it is concluded that the presented scheme is superior in carrying out the requisite bone details of CT image and abnormality facts of the MR image in its fusion image. Outcomes of Experiment 2 advocate the visual results by having better values of fusion quality assessment parameters for medical images and indicate better contrast, the mutual information of source images, brightness, and clarity in the CT and MRI fusion images of the presented methodology. Furthermore, the parametric results are validated scientifically by the Wilcoxon signed ranks test in Experiment 3. Finally, Experiment 4 shows the superiority of the presented method in terms of minimum computational complexity.

Table 6.4 Average Computation Time (in Seconds) Comparison

Dataset	DWTA [153]	SWT [154]	ASR [141]	CSR [146]	NSST [142]	Proposed
Harvard School	14.9441	97.1873	532.1423	96.1812	15.5076	**9.7250**
PGIMER	34.8958	457.2981	1687.8079	437.5677	80.6858	**23.5961**

6.5 CONCLUSIONS

In order to assist inexperienced radiologists and neurosurgeons, a new fusion scheme has been developed in NSST domain by applying the local sum of Gaussian weighted pixel intensities and SUSAN feature-based LF and HF activity measures, respectively. A real-time dataset and an online dataset are used to examine the robustness of the developed methodology. The methodology is evaluated visually and quantitatively using five fusion quality assessment metrics with five recent fusion approaches. Additionally, the Wilcoxon signed ranks test is applied to scientifically confirm the superiority of the proposed methodology. By observing the visual results, it is concluded that the fusion outcomes of the proposed methodology are superior in obtaining bone, calcified tumors, noncalcified

tumors, brain calcification, CSF and edema details with boundaries. The parametric comparison shows that the proposed fusion approach gives the highest value to most of the performance parameters in both the datasets. Wilcoxon signed ranks test proves that a significant difference exists between the population means of different parameters of the developed methodology and other methodologies. The presented scheme is computationally efficient as compared to other schemes. With the help of the fused image of the proposed methodology, the incision location in the bone or site of biopsy is rapidly identified to insert the surgical instruments thus reducing the risk of expurgating the normal brain parenchyma. The proposed scheme saves the diagnostic time of the radiologists and neurosurgeons in real-time situations.

CHAPTER 7

DETECTION OF ABNORMALITIES USING THE FUSION OF BRAIN CT AND MR IMAGES

7.1 INTRODUCTION

In medical imaging, automatic detection of brain diseases using the images of different modalities without the intervention of the expert radiologists has become an important area of research [155]. CT image is superior in bone, air and calcification information whereas MRI image is superior in soft tissue information. However, CT image has higher resolution than MRI and thus gives some soft tissue contrast and MRI also gives little air and bone information [156, 157]. MRI is useful in the evaluation of soft tissue abnormalities such as tumors and edema [158], though soft tissue evaluation using MRI is not always successful in every case [114]. The fused image provides better information of both these modalities. The aim is to use the fusion image obtained from these two modalities in image segmentation which may lead to better accuracy in abnormality detection and identification of its distance from the skull bone.

A few authors have done the segmentation of fused images of CT and MRI [156, 157]. Bayesian and level set segmentation methods are applied to the fused CT and MR images of the face [156]. It is observed from this methodology that the fusion image gives better soft tissue segmentation. The fusion images of three dimensional CT and MRI images of facial tissues are segmented using the Bayesian method in [157]. High segmentation accuracy is obtained by this method when the 3D fusion images are employed as input to the Bayesian model. However, it is observed from the literature that no attempt is made in analyzing the effect of fused brain CT and MR images in image segmentation and abnormalities detection as per the knowledge of the author. Hence, this research is an attempt to find out whether segmentation/ clustering is successful in the detection of abnormalities in a fused brain CT and MR image. To achieve this goal an automatic segmentation scheme designed by using NSCT and SWT based hybrid fusion scheme discussed in Chapter 5 and clustering-based segmentation of different tissues is presented. The NSCT-SWT based hybrid scheme is selected as it gives superior texture, contrast, clarity and edge information as compared to adaptive sparse representation [141] and NSST [3,94,142,143] based schemes. Four different types of clustering schemes are applied to segment the fused images into different tissues of the brain. These schemes are named as (i) k-means clustering [159] (ii)

expectation maximization (EM) clustering [160] (iii) morphological reconstruction based fuzzy c means (MRFCM) clustering [161] (iv) adaptive regularized kernel-based fuzzy C means clustering (ARKFCM) [162]. The clustering schemes are selected for segmenting the fusion images into different classes as these are widely used for medical diagnosis and pattern recognition [51]. Visual and quantitative analysis and comparison of these schemes are done in this chapter. The section below gives a detailed discussion of the clustering schemes used in this thesis.

7.1.1 K-Means Clustering

K-means clustering algorithm is demonstrated by [159]. It is a hard clustering scheme in which a pixel or data point is associated with one cluster center at a time [163]. In this scheme, n elements $(x_i = x_1, \ldots, x_n)$ are partitioned into k clusters $(c_i = c_1, \ldots, c_n)$. The aim is to optimize the objective function which is based on the minimization criteria of the Euclidian distance between a data point and the cluster center. Eqn.7.1 represents the objective function of k-means clustering as shown below:

$$f_m = \sum_{i=1}^{c} \sum_{j=1}^{N} \left\| x_{ij} - C_i \right\|^2 \tag{7.1}$$

where, N represents the no. of feature vectors in the i^{th} cluster, c is the number of cluster centers and $\left\| x_{ij} - C_i \right\|^2$ is the Euclidian distance between the data object x_j and the cluster centroid C_i. This implies that out of n feature vectors or data points each point has a possibility of belonging to a particular cluster. The i^{th} centroid C_i is computed as

$$C_i = \frac{1}{N} \sum_{j=1}^{N} x_{ij} \tag{7.2}$$

The algorithm can be explained using the following steps:

1. Choose the centroids of c clusters from the data points x_i in a random way.
2. Compute the Euclidean distance between all the data points and each centroid.
3. Assign a specific data point to the cluster with which it has minimum distance.
4. Update the centroids using the formula given in eqn.7.2.
5. Recalculate the Euclidian distance.
6. Repeat steps 4-5 if the new data points are assigned to a cluster otherwise, the algorithm terminates.

7.1.2 Fuzzy C Means Clustering

The objective function of the FCM clustering scheme is expressed as follows:

$$f_m = \sum_{i=1}^{N}\sum_{j=1}^{c} u_{ij}^{\,m} \left\| x_i - C_j \right\|^2, 1 \le m < \infty \tag{7.3}$$

where, N is the no. of data points in the data $(x_i = x_1, \ldots, x_N)$ and c is the number of clusters. u_{ij} is the degree of membership of i^{th} data object in the j^{th} cluster and m is called the fuzziness index which controls the degree of membership or belongingness on each classification [163]. $\left\| x_i - C_j \right\|^2$ is the Euclidian distance between the data object x_i and the cluster centroid C_j. Eqn.7.3 is minimized using the following expressions:

$$u_{ij} = \frac{1}{\sum_{k=1}^{c}\left(\frac{\left\| x_i - C_j \right\|}{\left\| x_i - C_k \right\|} \right)^{2/m-1}} \tag{7.4}$$

$$\text{and } C_j = \frac{\sum_{i=1}^{N} u_{ij}^{\,m} x_i}{\sum_{i=1}^{N} u_{ij}^{\,m}} \tag{7.5}$$

The FCM algorithm optimizes the objective function by continuously updating the membership matrix and cluster centers until the following condition is met:

$$\left| u_{ij}^{\,t+1} - u_{ij}^{\,t} \right| \le T \tag{7.6}$$

where, t denotes the iteration count and T represents the threshold for termination of the algorithm. As a first step the membership matrix is initialized randomly and the centroids are computed using eqn.7.5 [163]. The new membership values are computed using eqn.7.4 and thereafter the values obtained in $(t+1)^{th}$ iteration is compared with $(t)^{th}$ iteration [165]. The algorithm stops if the difference $u_{ij}^{\,t+1} - u_{ij}^{\,t}$ is less than a user-defined threshold T, otherwise the centroids are computed again and the algorithm is repeated.

7.1.3 Expectation-Maximization (EM) Clustering Algorithm

The expectation-maximization (EM) clustering algorithm is similar to k-means clustering with the difference that it is a type of soft clustering method [160, 165]. The EM algorithm finds the clusters in the data based upon some probabilistic distributions [166]. An expectation (weight) is assigned to each data object in a cluster [166]. The weights of the pixels or data objects are updated in an iterative way. The data point which has the highest weight for a cluster is assigned finally to that cluster. The EM clustering is repeated for all the new sets of partitions until the partitions do not change by a threshold amount. In this

research, the threshold is taken as 0.0001. The algorithm works in two phases (i) expectation phase (ii) maximization phase. These phases are explained in the following steps:

1. Initialize the number of clusters.

2. Estimate the mean (μ) and variance (σ) based on the number of clusters and the image histogram.

3. Using the parameters obtained in step 2, compute the expectation or likelihood of the data in a cluster as described by eqn.7.7 as follows:

$$E\left[Z_{ij}\right] = \frac{P(X = X_i / \mu = \mu_j)}{\sum_{i=1}^{m} P(X = X_i / \mu = \mu_j)} \tag{7.7}$$

where, $E\left[Z_{ij}\right]$ represents the likelihood or expectation of pixel i belonging to the cluster j. The expectation is equal to the ratio of the probability of belonging of a pixel x_i to cluster j and the summation of the probability of all the pixels x_i (i = 1,2....m) in the cluster j. Probability of pixel i belonging to the cluster j is computed as follows:

$$P(X = X_i / \mu = \mu_j) = e^{-\frac{1}{2}\sigma_j^2 (X_i - \mu_j)^2} \tag{7.8}$$

where, μ_j is the mean of the cluster j and σ_j is the variance.

4. Taking the information from step 3, compute the new values of mean and variance as expressed by eqn.7.9 and eqn.7.10 as follows:

$$\mu_j = \frac{\sum_{i=1}^{m} E\left[Z_{ij}\right] x_i}{\sum_{i=1}^{m} E\left[Z_{ij}\right]} \tag{7.9}$$

$$\sigma_j = \frac{\sum_{i=1}^{m} E\left[Z_{ij}\right] \left(X_i - \mu_j\right) \left(X_i - \mu_j\right)^T}{\sum_{i=1}^{m} E\left[Z_{ij}\right]} \tag{7.10}$$

where, m represents the number of data points in the cluster j. This step is called as the maximization phase.

5. The expectation and maximization steps are repeated again until the expected value as computed by step 3 converges to the maximum.

6. Generate the classification matrix and based upon it assign the labels to the clustered image [155].

7.1.4 Morphological Reconstruction based FCM Clustering Algorithm (MRFCM)

It is an improved version of the FCM scheme which is proposed by [161]. Initially, this algorithm pre-processes the source image F through morphological dilation and erosion operators to construct another image ξ expressed as follows:

$$\xi = R^{C}(F) \tag{7.11}$$

where, R^{C} represents the morphological closing operation on the source image to be clustered. Thereafter the histogram of the morphologically reconstructed image is computed to find γ_i which represents the number of pixels in the histogram having intensity i and the following relationship exists:

$$\sum_{i=1}^{q} \gamma_i = N \tag{7.12}$$

where, N is the number of data points in the original image F and q represents the number of gray levels in the image histogram which is much lesser than N. The objective function f_m of the algorithm is expressed as:

$$f_m = \sum_{i=1}^{q} \sum_{j=1}^{c} \gamma_i u_{ij}^{\ m} \left\| \xi_i - C_j \right\|^2 \tag{7.13}$$

where, u_{ij} is fuzzy membership of intensity i present in cluster j. c represents the number of clusters and C_j is the j^{th} cluster center. m is the weighting exponent of each membership element. The minimization of the objective function of eqn.7.13 gives the following solution:

$$u_{ij} = \frac{\left\| \xi_i - C_j \right\|^{-2/(m-1)}}{\sum_{k=1}^{C} \left\| \xi_i - C_k \right\|^{-2/(m-1)}} \tag{7.14}$$

$$C_j = \frac{\sum_{i=1}^{q} \gamma_i u_{ij}^{\ m} \xi_i}{\sum_{i=1}^{q} \gamma_i u_{ij}^{\ m}} \tag{7.15}$$

From eqn.7.14 matrix $U = (u_{ij})^{c \times q}$ is obtained. A new membership matrix $U' = (u_{ij})^{c \times N}$ is generated which pertains to the source image F. In order to make the algorithm converge rapidly and to reduce the effect of noise, matrix U' is processed by the median filter. The resultant membership matrix is defined as:

$$U'' = \text{median}\ (U') \tag{7.16}$$

Eqn.7.14 and eqn.7.15 are continuously repeated until the following condition is attained:

$$\left|u_{ij}^{t+1} - u_{ij}^{t}\right| \leq T \tag{7.17}$$

where, t represents the iteration number and T represents the threshold value.

The morphological reconstruction feature makes this algorithm faster and less prone to noise effects and the median filter is employed to smooth the membership matrix which reduces the cluster misclassification errors.

7.1.5 Adaptive Regularized Kernel-based Fuzzy C Means Clustering (ARKFCM)

As the original FCM algorithm does not contain the neighborhood information in its objective function hence, its performance is largely degraded in the presence of noise and image artifacts. Moreover, FCM clustering is affected by the outliers in the data as it is based upon the Euclidian distance and its processing is slow. In order to take care of these shortcomings, Ahmad et. al. [162] proposed an improved version of the original FCM algorithm in which a regularisation parameter ψ is introduced in the objective function. This is done to include the role of neighborhood information in the clustering process and for faster computation. The parameter ψ is computed from the local variation coefficient (Lvc) which is expressed as follows:

$$\mathrm{Lvc}_i = \frac{\sum_{k \in n_i} (x_k - \bar{X}_i)^2}{n_r \times (\bar{X}_i)^2} \tag{7.18}$$

where, x_k is the intensity of a pixel belonging to a local window n_i around the central pixel x_i. n_r is the cardinality of n_i and $\bar{X}_i$ is the mean intensity of the pixels within the window n_i. A new exponent term ξ and a pixel weight parameter w are computed from Lvc as follows:

$$\xi_i = \exp\left(\sum_{k \in n_i, i \neq k} \mathrm{Lvc}_k \right) \tag{7.19}$$

$$w_i = \frac{\xi_i}{\sum_{k \in n_i} \xi_k} \tag{7.20}$$

From eqn.7.19 and eqn.7.20 the regularisation parameter (ψ) is defined as:

$$\psi_i = \begin{cases} 2 + w_i; & \bar{X}_i < x_i \\ 2 - w_i; & \bar{X}_i > x_i \\ 0; & \bar{X}_i = x_i \end{cases} \tag{7.21}$$

From eqn.7.21 it is clear that ψ_i assigns a higher weight to the central pixel which possesses higher Lvc (when the central pixel has higher brightness than the mean brightness

of the neighbors within the window n_i) else, assigns lower value. The parameter ψ_i does not depend upon the cluster centers and hence can be computed in advance which makes this algorithm faster than the FCM algorithm. ψ_i is based upon the heterogeneity of the local information hence, it produces homogeneous clusters. Instead of Euclidian distance, it uses Gaussian based radial kernel for clustering which is less prone to outliers. Using a kernel function the Euclidian distance is replaced by a new expression which is mentioned as follows:

$$\left\|\phi(x_i)-\phi(v_j)\right\|^2 = 2(1-\kappa(x_i, v_j)) \tag{7.22}$$

where, κ represents the kernel function, x_i is the data point and v_j is the cluster center. The Gaussian radial basis kernel function is expressed as:

$$\kappa(x_i, v_j) = \exp\left(\frac{-\left\|x_i - v_j\right\|^2}{2\sigma^2}\right) \tag{7.23}$$

and

$$\sigma = \left[\frac{\sum_{i=1}^{n}(d_i - \bar{d})^2}{n-1}\right]^{\frac{1}{2}} \tag{7.24}$$

where, n is the total number of pixels in the image. The distance d_i is computed as:

$$d_i = \left\|x_i - \bar{x}\right\| \tag{7.25}$$

where, $\bar{x}$ represents the mean intensity of n number of pixels of the image. $\bar{d}$ represents the average value of $d_i (i = 1, 2.....n)$. The objective function of the ARKFCM clustering scheme is given as follows:

$$Obj_{ARKFCM} = 2\left[\sum_{i=1}^{n}\sum_{j=1}^{c} u_{ij}^m (1-\kappa(x_i, v_j)) + \sum_{i=1}^{n}\sum_{j=1}^{c} \psi_i u_{ij}^m (1-\kappa(\bar{x}_i, v_j))\right] \tag{7.26}$$

where, u_{ij} and v_j represents membership function of x_i and j^{th} cluster centers, respectively. ψ_i controls the neighborhood details as mentioned earlier and m is a real number > 1. It represents the degree of fuzziness, c represents the number of clusters and $\bar{x}_i$ is the grayscale of the average filtered image [163].

7.2 METHODOLOGY

The proposed framework consists of the following three important steps:

1. Preprocessing - which includes registration of the images and conversion from RGB to grayscale images.

2. Fusion - in which NSCT-SWT based hybrid scheme along with the locally weighted sum of the square of the coefficients, sum modified Laplacian and entropy of square of the coefficient based fusion rules are employed.

3. Clustering- abnormality in the brain is detected using segmentation techniques in which different clustering schemes are employed.

Figure 7.1 shows the methodology used in the clustering of fused CT and MR images for the detection of brain abnormalities. Initially, the images are registered using the MATLAB and image processing toolbox and converted to greyscale images. Thereafter the aligned images are decomposed into LF and HF sub-bands using NSCT. The LF sub-band is further decomposed using two-stage SWT into one LF sub-band and three detail sub-bands. The entropy of square of the coefficients and the sum modified Laplacian based fusion rules are

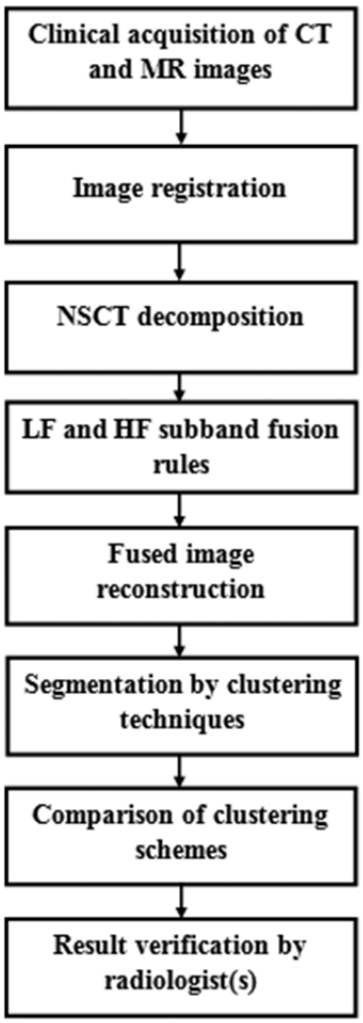

Figure 7.1 Block diagram representation of the proposed fusion based clustering scheme for the detection of abnormalities in the fused CT-MRI images

applied in LF and HF sub-bands of SWT, respectively. The locally weighted sum of the square of sub-band coefficients based fusion rule is applied with HF sub-bands of NSCT. The fused image reconstruction is done using inverse NSCT. The reconstructed fused image is clustered using four different schemes for the detection of abnormalities. A visual and quantitative comparison of four clustering schemes is done by the author and the radiologists. The number of clusters is taken as four in all the clustering schemes for comparing their performance.

7.3 EXPERIMENTAL SETUP

All the experiments are conducted in MATLAB software. The experiments are conducted on two datasets of the PGIMER and Harvard medical school dataset. The fused images of NSCT and SWT based hybrid fusion scheme are segmented using k-means clustering [159], EM clustering [160], a morphological reconstruction based fuzzy C means clustering [161] and ARKFCM clustering [162]. Performance of the clustering schemes is checked visually after segmenting the single modality MR images as well as information fusion of the two modalities. The accuracy of the segmentation of the fused images is assessed quantitatively using a parameter named as the partition coefficient.

Three experiments are performed to evaluate the efficacy of clustering schemes in the segmentation of abnormalities in the fused images of NSCT and SWT based hybrid fusion scheme.

Experiment 1: Visual analysis and comparison of the performance of four different clustering schemes in the detection of abnormalities in the fused brain CT and MR images of PGIMER and Harvard school dataset.

Experiment 2: Visual analysis and comparison of the performance of MRFCM and ARKFCM schemes in the detection of abnormalities in the segmented MR and fused images using the aforementioned datasets.

Experiment 3: Quantitative comparison of different clustering schemes in the detection of abnormalities in the fused images of both the datasets using the partition coefficient as a performance parameter.

7.3.1 Evaluation Criteria

Qualitative analysis: Visual clustering analysis is done by the author and expert radiologists for the detection of abnormalities in the segmented images of four clustering schemes using the Harvard and PGIMER dataset.

Quantitative analysis: Parametric analysis is done using partition coefficient as a performance parameter. The details of this parameter is already discussed in Chapter 3.

7.4 RESULTS AND DISCUSSIONS

7.4.1 Experiment 1: Visual Analysis and Comparison of the Performance of Four Different Clustering Schemes in the Detection of Abnormalities in the Fused Images of PGIMER and Harvard School Dataset.

A qualitative analysis and comparison of the performance of four different clustering schemes in the detection of abnormalities in the fused brain CT and MR images are done in this experiment. Figure 7.2, Figure 7.3 and Figure 7.4, Figure 7.5 show the visual comparison of different clustering schemes for the Harvard medical school and PGIMER dataset, respectively.

Figure 7.2(a1-c1) shows the CT, MR, and fused image, respectively of a stroke patient who can write but can't read. As observed from Figure 7.2(d1), the k-means clustering scheme segments the soft tissues properly, however, the clustering result of the k-means scheme is not always the same and varies from one iteration to other iteration. The clustering result of the EM clustering algorithm as shown in Figure 7.2(e1) is not up to the mark. The clustering result of the MRFCM scheme shows clear boundary details of tissues. The clustering result of the ARKFCM scheme as shown in Figure 7.2(g1) is better than MRFCM except for the boundary details and better than the other schemes. The minute details of the portion as marked by red arrows in Figure 7.2(g1) are also better seen in this scheme. Note that the lesion (infarct) in the corpus callosum splenium on the left side is best depicted in the ARKFCM scheme as marked in yellow.

Figure 7.2(h1-j1) shows the CT, MR, and fused image, respectively of a metastatic bronchogenic carcinoma patient. The outcome of the k-means clustering is not stable for this image, EM clustering does not segment the abnormality region of this case accurately. As observed from Figure 7.2(m1) which represents the MRFCM clustering scheme, the CSF and some portion of GM are not properly separated whereas, in Figure 7.2(n1) the ARKFCM clustering scheme, it is better segmented (marked by red arrows). The ARKFCM scheme delineates edema in an efficient manner. The metastatic lesion is demonstrated in the clustered fused image, however it is always wise to refer to the original dataset, wherever available, for confirmation (herein the lesion is being aptly seen in the MR image as pointed in red).

Almost similar results are obtained for other images of this dataset as shown in Figure 7.2(o1-l2) and Figure 7.3(a1-e2). It is observed that the results of MRFCM and ARKFCM schemes are comparable. However, the MRFCM based scheme fails to cluster the arrow

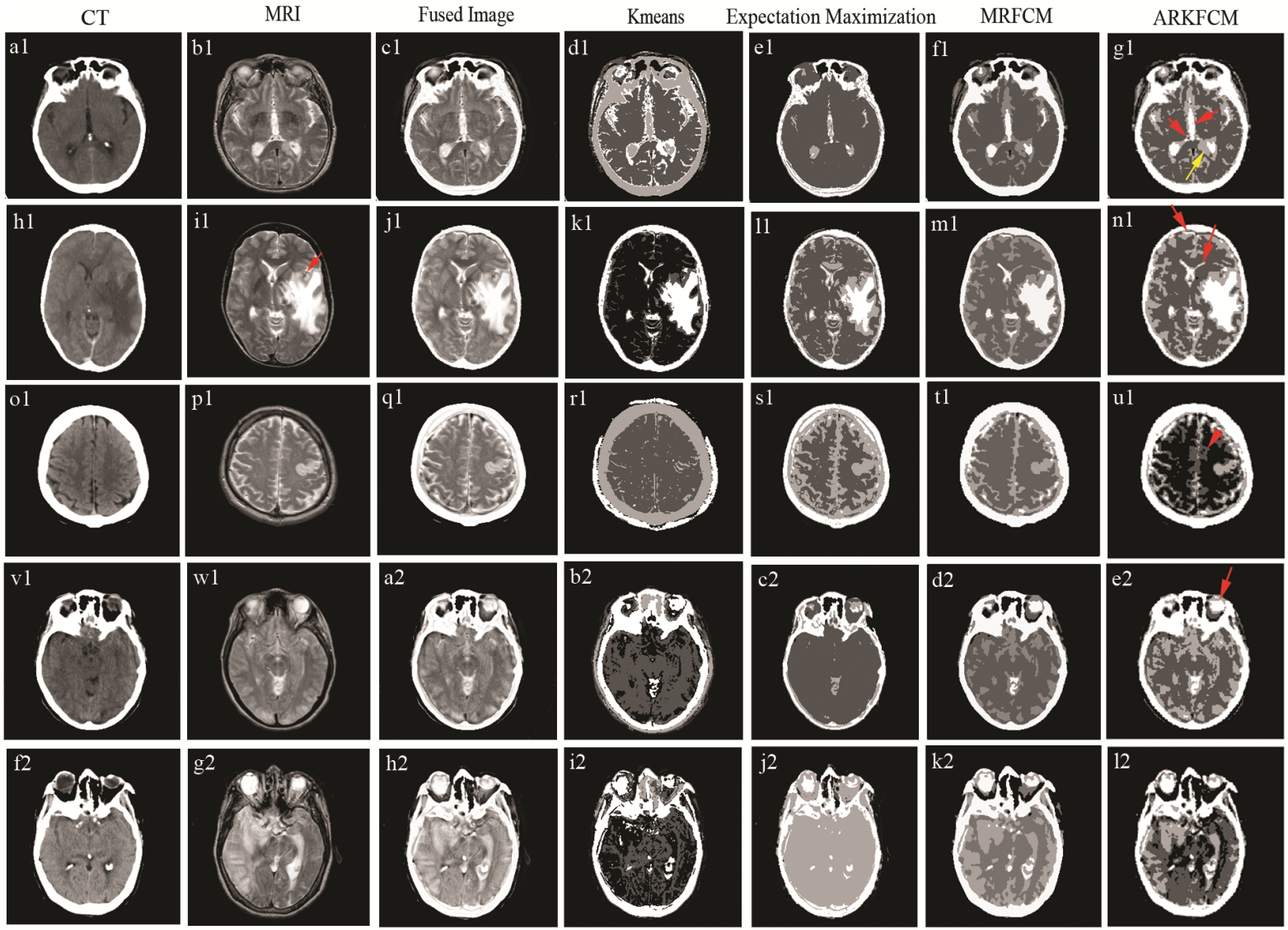

Figure 7.2 Visual comparison of different clustering schemes for Harvard medical school dataset

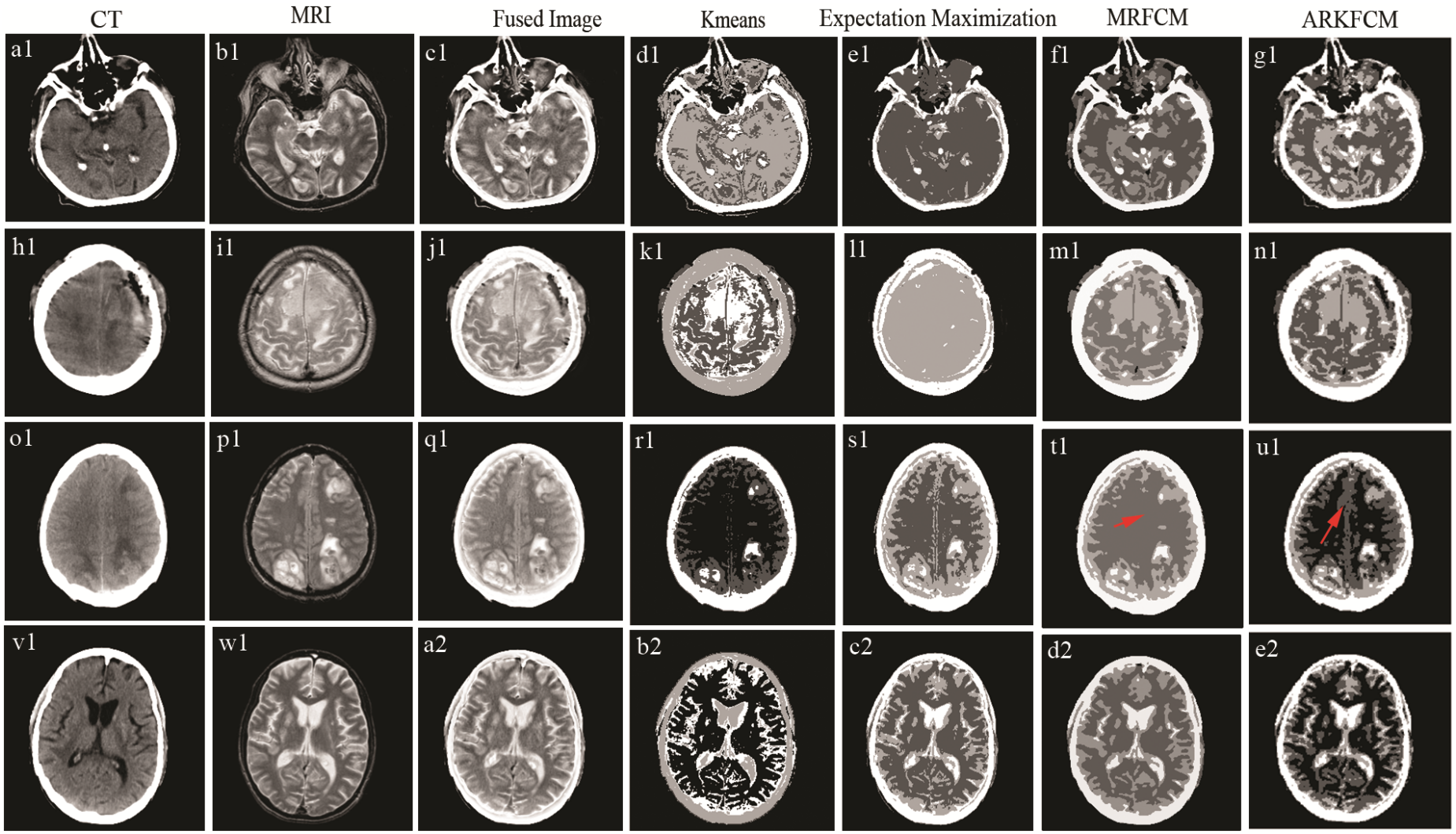

Figure 7.3 Visual comparison of different clustering schemes for Harvard medical school dataset

marked region of Figure 7.3(t1) of a brain tumor (sarcoma) patient. This area is better seen in the ARKFCM scheme which is marked by the red arrow in Figure 7.3(u1). The abnormalities are better seen in the ARKFCM clustering scheme as compared to the MRFCM scheme.

Figure 7.4(a1-c1) shows the CT, MR, and fused image, respectively of a patient suffering from glioma. Figure 7.4(d1-g1) shows the clustering results of k-means, EM, MRFCM, and ARKFCM based clustering schemes, respectively. Tumour boundary is poorly segmented by the EM clustering scheme as shown in Figure 7.4(e1) whereas, the clustering result of the k-means algorithm varies with every iteration. As observed from Figure 7.4(g1), the demarcation between the heterogeneous tumor and edema is better in the clustered image of ARKFCM scheme. Similar results are obtained in differentiating the tumor from edema in MRFCM clustering which is shown in Figure 7.4(f1). It is observed that k-means, EM and MRFCM schemes failed to segment some areas of the tumor of this patient which has large intensity variations. Similar results are observed for another clustered image shown in Figure 7.4(h1-n1).

Figure 7.4(o1-q1) shows the CT, MR, and fused image, respectively of a patient having the calcified tumor. It is observed from the clustered image shown in Figure 7.4(r1-t1) of k-means, EM and MRFCM schemes, respectively that almost half the portion of the non-calcified tumor of MR image (marked with the red arrow in Figure 7.4(p1)) is misclassified as background. However, this parenchymal tumor region is accurately classified and clearly differentiated from the surrounding background tissues in the case of the ARKFCM clustering scheme as shown in Figure 7.4(u1). Figure 7.4(v1-a2) shows the CT, MR, and fused images, respectively of a different section for the same patient. Figure 7.4(b2) shows the result of k-means segmentation however, its clustering is not always stable. The result of the EM scheme as shown in Figure 7.4(c2) is not up to the mark. The results of MRFCM and ARKFCM clustering are comparable to each other as shown in Figure 7.4(d2-e2), respectively.

Figure 7.5(a1-c1) shows the CT, MR, and fused image, respectively of another patient of PGIMER dataset. The EM scheme does not segment the CSF accurately in this case as marked by the red arrow in Figure 7.5(e1). The MRFCM scheme gives the best clustering result and CSF boundary information which is clear from Figure 7.5(f1).

Figure 7.5(h1-j1) shows the source images and fused image, respectively of a patient suffering from a postoperative tumor. The k-means and MRFCM scheme cluster the tumor region of this case in two different classes which is evident from Figure 7.5(k1) and Figure 7.5(m1), respectively. The EM-based scheme segments clearly white matter (WM) and gray

matter (GM) with a clear detection of the tumor region as represented by Figure 7.5(l1). The tumor region and boundary is precisely segmented as well as the surrounding regions are better differentiated by ARKFCM scheme as indicated by the red arrow in Figure 7.5(n1).

Figure 7.5(o1-q1) shows another image pair and its fusion result, respectively. The k-means based scheme gives the worst results in this case. The EM, MRFCM and ARKFCM schemes provide comparable results for this patient.

7.4.2 Experiment 2: Visual Analysis and Comparison of Abnormalities in the Segmented MR and Fused Images using MRFCM and ARKFCM Clustering Schemes for both the Datasets.

In order to prove the effectiveness and advantage of information fusion of CT with MRI in clustering schemes, a comparison of clustered MR images and clustered fused images for PGIMER dataset is shown in Figure 7.6 and Figure 7.7.

Figure 7.6(a1-c1) shows the CT, MR, and fused images, respectively of a tumor patient. Figure 7.6(d1) shows the MRI image which is clustered using the MRFCM scheme. Figure 7.6(e1) shows the fused image which is clustered using the MRFCM scheme whereas, Figure 7.6(f1,g1) shows the segmented MRI image and segmented fusion image of the ARKFCM clustering scheme. From these figures, it is seen that the segmented MR images of MRFCM and ARKFCM schemes have the worst bone information. CT-MR fused and the segmented image shows better bone, tumor and edema segmentation and other soft tissues as indicated by red arrows in Figure 7.6(e1) and Figure 7.6(g1). Almost similar results are obtained for source images shown in Figure 7.6(h1-j1) and clustered images shown in Figure 7.6(k1-n1).

Figure 7.6(o1-q1) and Figure 7.6(v1-a2) show the CT, MRI and fused images of two different sections of the same patient. It is observed from the segmented MR images of the MRFCM and ARKFCM schemes that these images have poor bone information and no calcification information. CT-MR fused and segmented images show better bone, calcification segmentation as well as soft tissues as indicated by the red arrow in Figure 7.6(s1, u1, c2, e2). In the directly segmented MR images as shown in Figure 7.6(r1, t1, b2, d2) it is not possible to differentiate between tumor and surrounding tissues whereas, the fused segmented images well-differentiate these two types of tissue classes.

Figure 7.7(a1-c1) shows the CT, MR and fused image of a patient suffering from a post-operative tumor. The intensity inhomogeneity surrounding the tumor region is marked by the red arrow in Figure 7.7(d1, f1) which is clustered as a separate class from the surrounding normal tissues in case of segmented MR images of MRFCM and ARKFCM clustering methods.

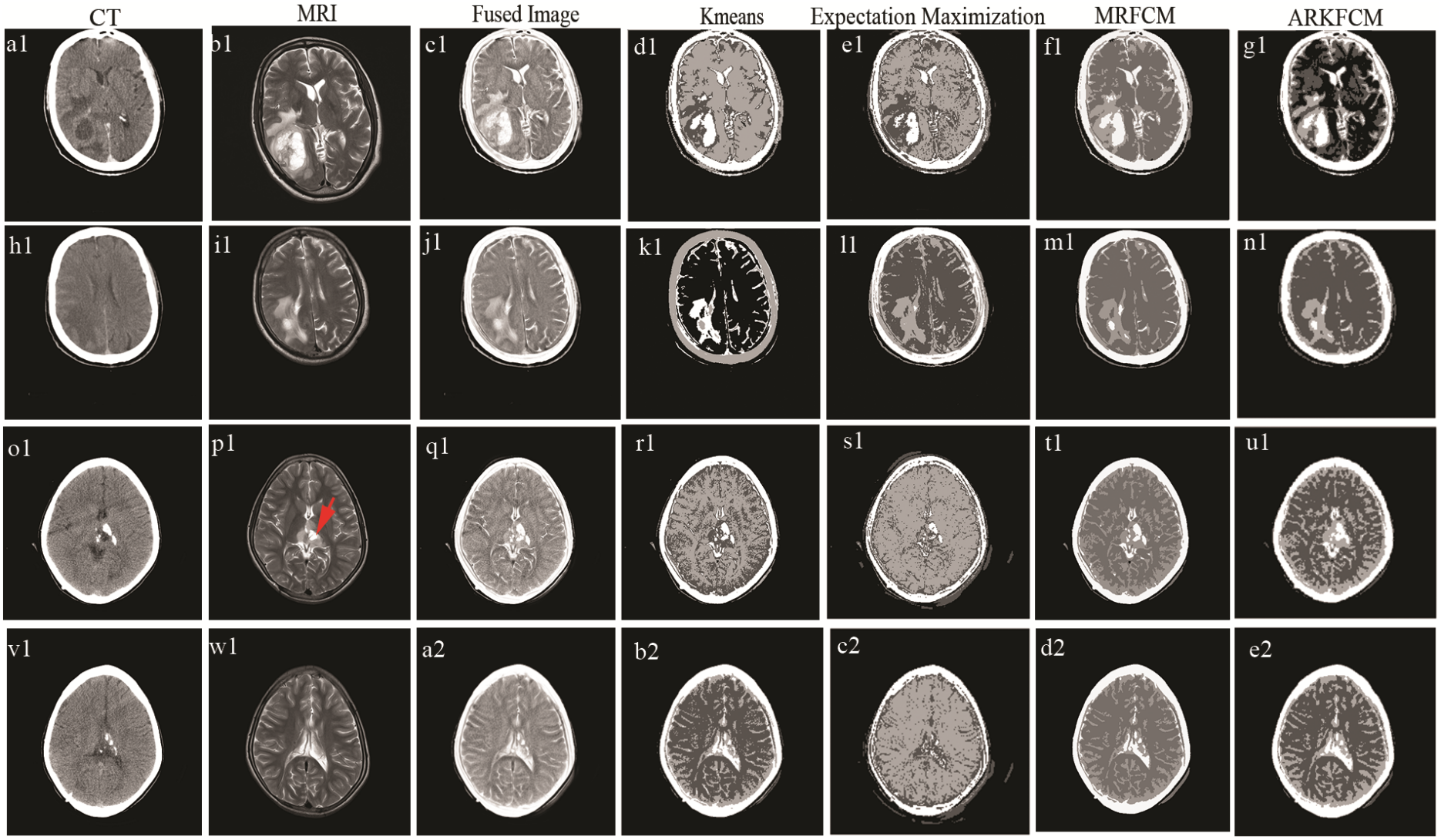

Figure 7.4 Visual comparison of different clustering schemes for PGIMER dataset

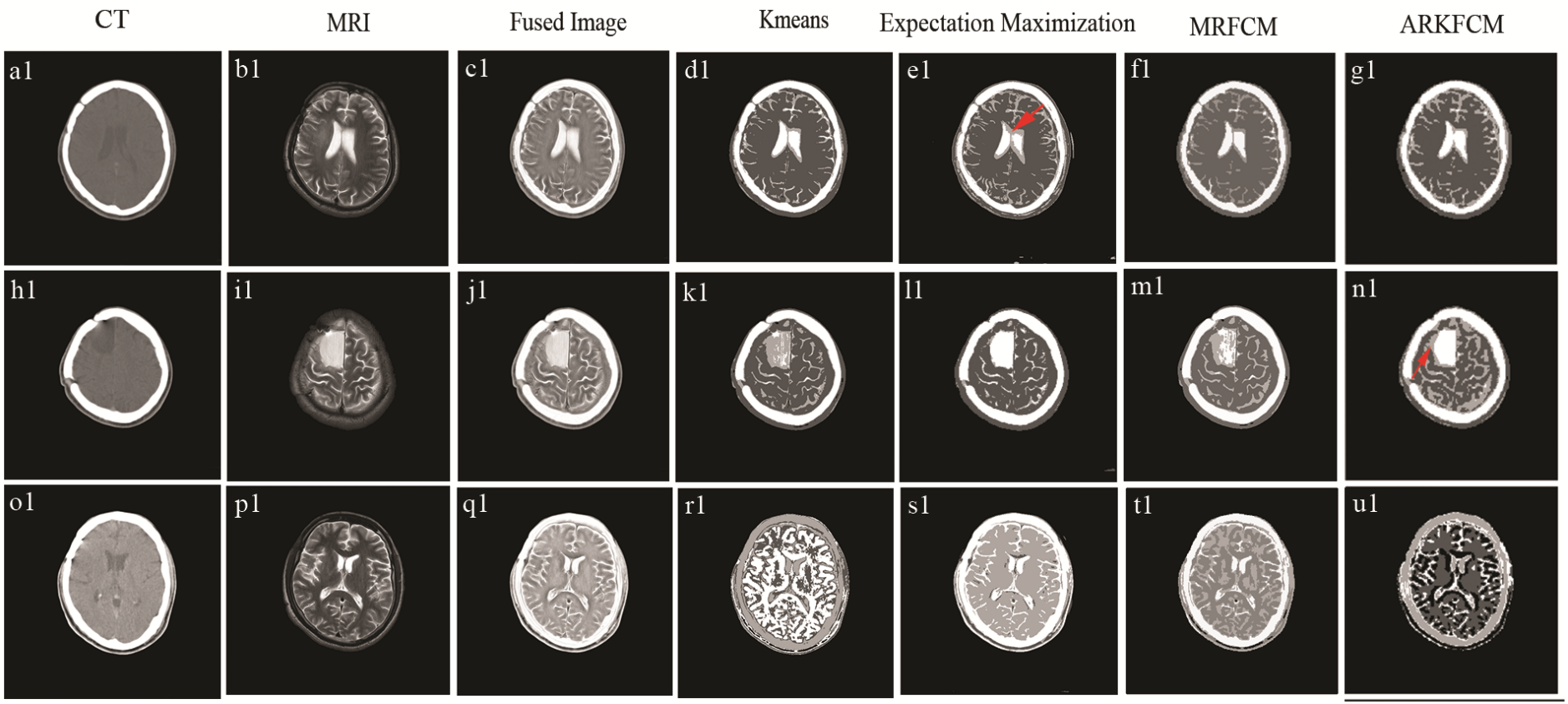

Figure 7.5 Visual comparison of different clustering schemes for PGIMER dataset

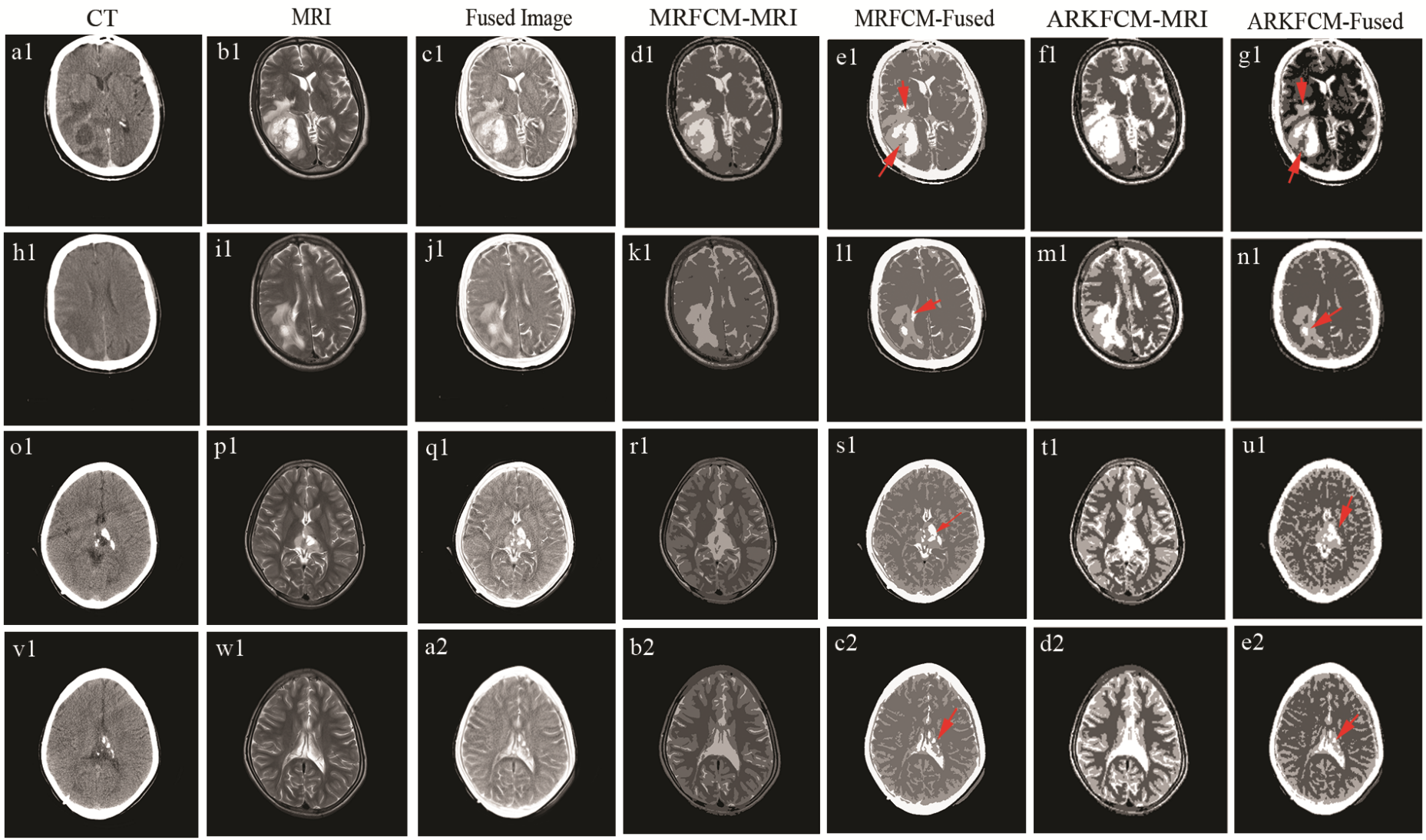

Figure 7.6 Comparative visual results of clustered MR images and clustered fusion images of PGIMER dataset using MRFCM and ARKFCM methods

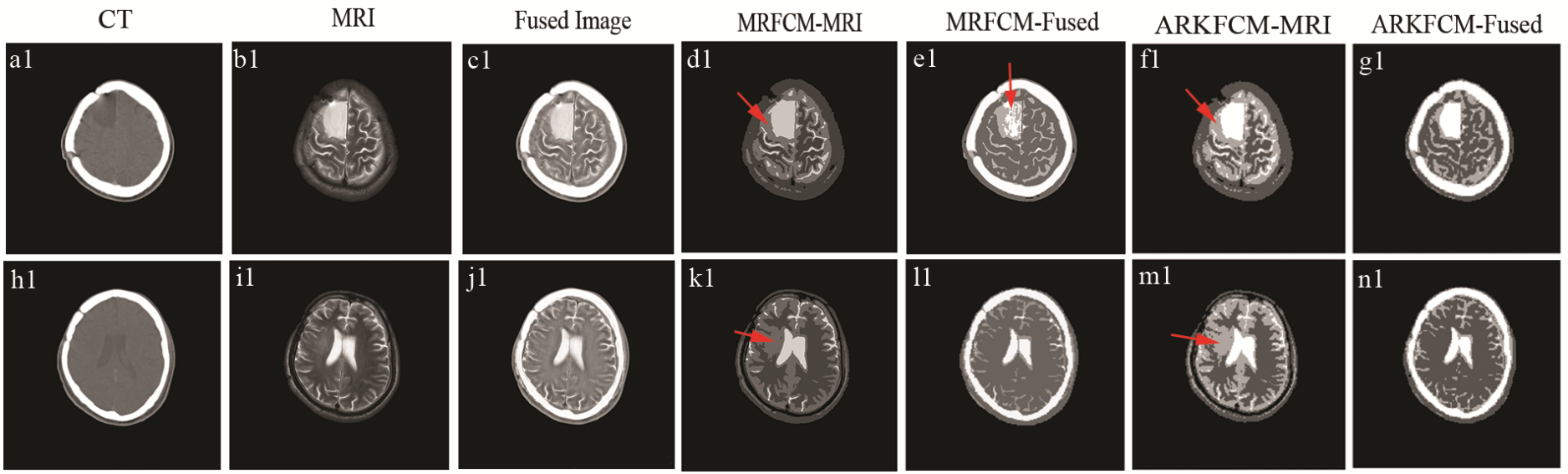

Figure 7.7 Comparative visual results of clustered MR images and clustered fusion images of PGIMER dataset using MRFCM and ARKFCM methods

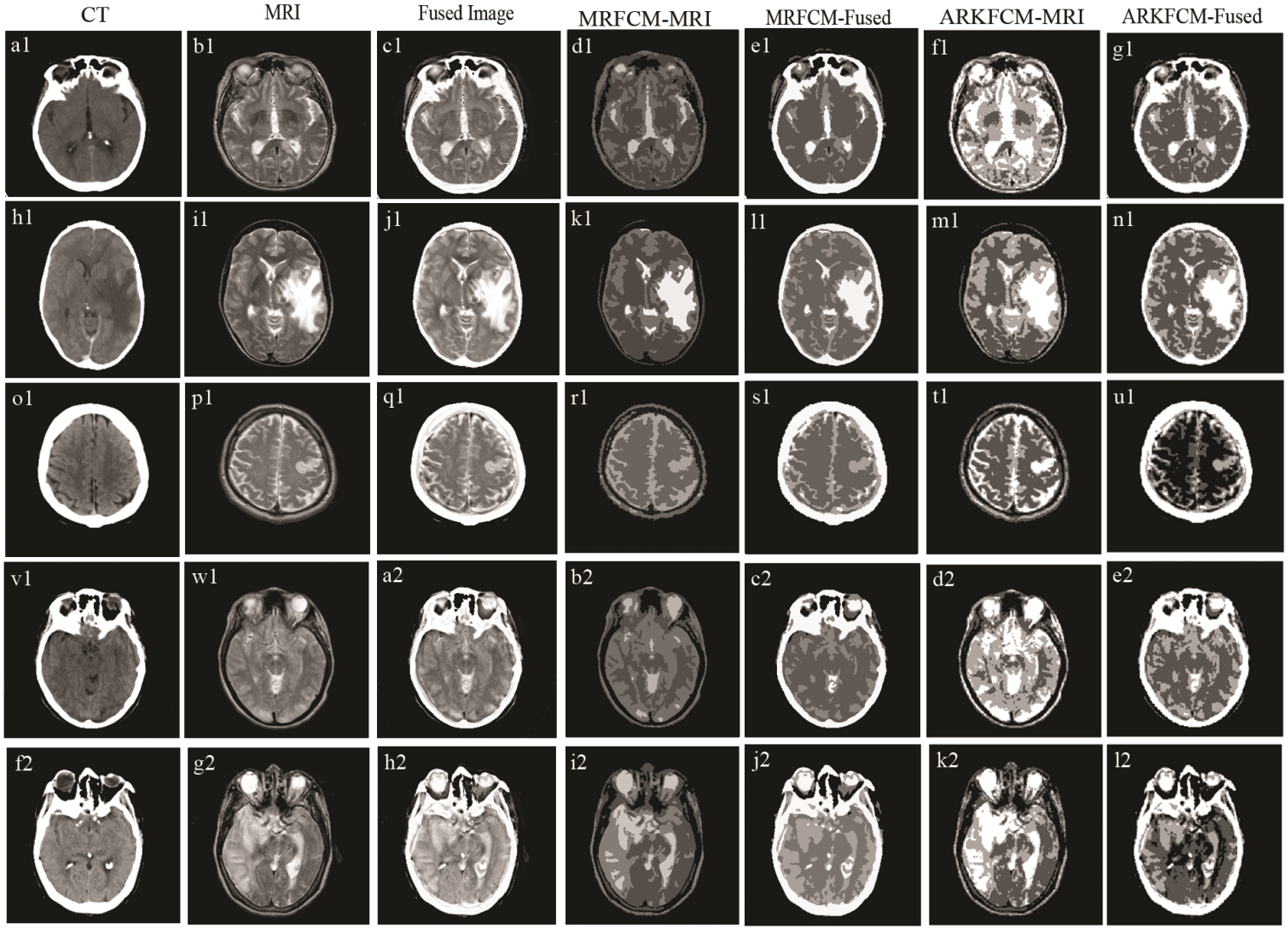

Figure 7.8 Comparative visual results of clustered MR images and clustered fusion images of Harvard dataset using MRFCM and ARKFCM methods

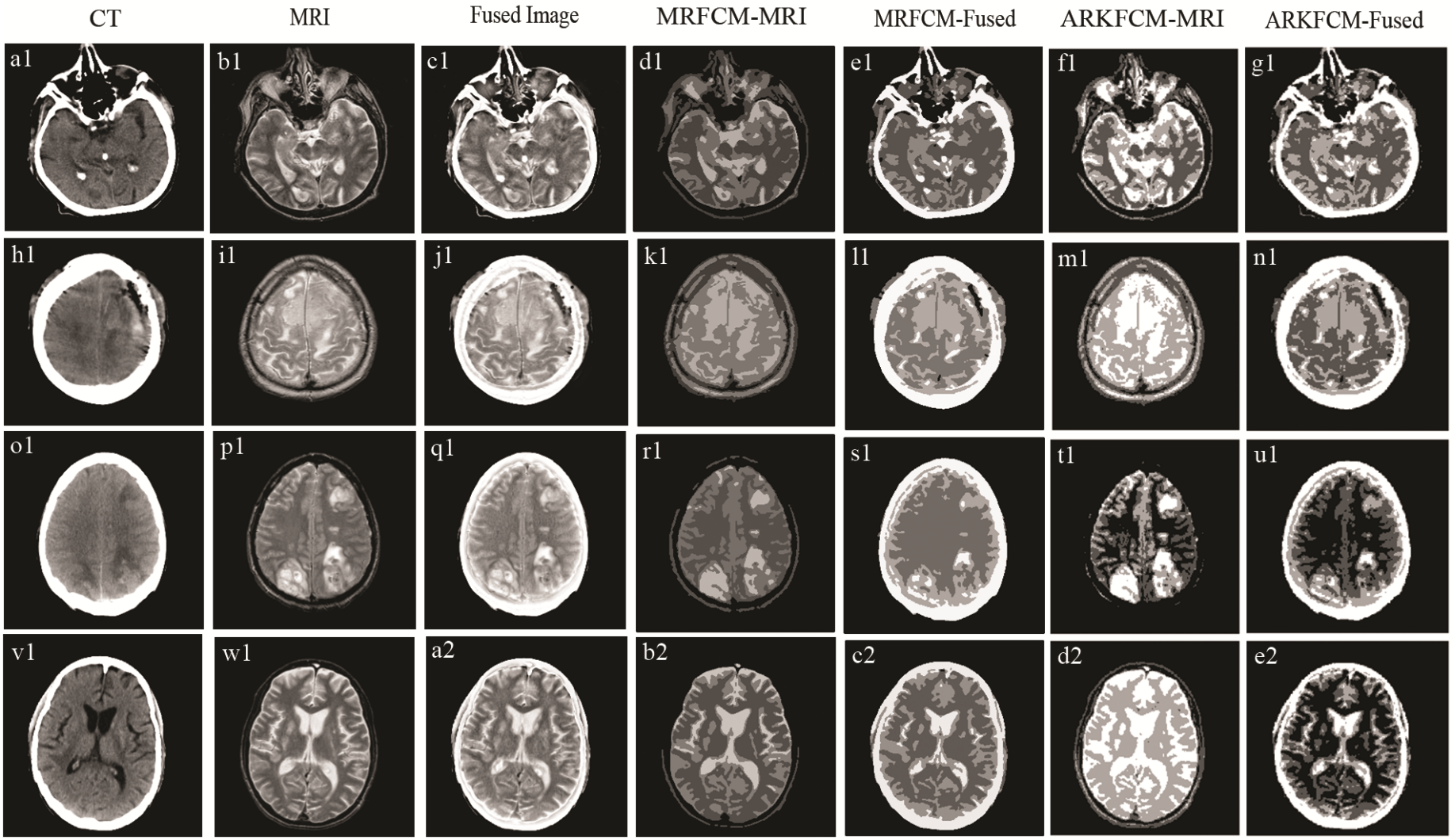

Figure 7.9 Comparative visual results of clustered MR images and clustered fusion images of Harvard dataset using MRFCM and ARKFCM methods

The tumor region is misclassified in two different classes by the MRFCM clustering scheme as marked by the red arrow in Figure 7.7(e1). However, the tumor area and the surrounding tissues are better classified in ARKFCM segmented fused image as shown in Figure 7.7(g1). Figure 7.7(h1-j1) shows another pair of the source image and the fusion image. Figure 7.7(k1,m1) shows the directly segmented MR image of MRFCM and ARKFCM schemes. From the directly segmented MR images, it is observed that the intensity inhomogeneity of source MR image is segmented as a different class from the surrounding soft tissues as shown by the red arrow in Figure 7.7(k1,m1). However, the intensity inhomogeneity is not present in the segmented results of the fused image as shown in Figure 7.7(l1,n1) for the MRFCM and ARKFCM schemes. A comparison of the clustered MR images and clustered fused CT and MR images using different clustering schemes for the Harvard dataset is also shown in Figure 7.8 and Figure 7.9. From these figures, it is evident that the segmentation after fusion of CT and MRI provides benefits in terms of bone information, calcification details, air information in all the cases and better abnormality detection in most of the cases.

7.4.3 Experiment 3: Quantitative Analysis and Comparison of Four Different Clustering Schemes for Harvard Medical School and PGIMER Dataset.

Table 7.1 and Table 7.2 show the quantitative comparison of different clustering schemes in terms of partition coefficient parameter for Harvard medical school and PGIMER dataset, respectively. From Table 7.1 it is clear that the value of the partition coefficient is highest for all the nine images clustered by the ARKFCM scheme and lowest for EM-based clustering. The column for k-means clustering is kept blank in Table 7.1 and Table 7.2 as this parameter is not valid for the k-means based scheme and hence cannot be computed for this scheme. The average value of this parameter for the ARKFCM scheme is 0.9986 which is very close to one. This indicates the best cluster partitioning by this scheme. The average value of the partition coefficient for the MRFCM scheme and the EM scheme is 0.7920 and 0.3839, respectively.

Table 7.2 shows the partition coefficient values of six clustered fusion images of the PGIMER dataset. From these results it is seen that out of six images, the ARKFCM scheme obtains the highest value of this parameter for two images. The MRFCM scheme obtains the highest value for four images and the EM scheme obtains minimum value for all the images. The average value of this parameter for ARKFCM, MRFCM and EM-based schemes is 0.7079, 0.8475 and 0.4214, respectively. From the above quantitative analysis, it is clear that the ARKFCM scheme obtains the highest value of this parameter for Harvard

dataset and two of the PGIMER dataset images. The MRFCM clustering dominates in most of the cases of the PGIMER dataset. The results vary due to the subsampling and interpolation operations during the registration of the realtime PGIMER dataset. The ARKFCM method could not cluster this dataset efficiently. As a result, there is an overlapping between clusters. The morphological reconstruction feature of the MRFCM method makes this algorithm less prone to noise effects and the median filter employed to smooth the membership matrix reduces the cluster misclassification errors for this dataset. Hence, the MRFCM method clustered the PGIMER dataset better as compared to the ARKFCM method.

Table.7.1 Averaged Parametric Comparison of 09 Clustered Fusion Images of Harvard Medical School Dataset

Dataset	K-means	EM	MRFCM	ARKFCM
#1	-	0.4083	0.7696	0.9961
#2	-	0.4323	0.8374	0.9993
#3	-	0.4156	0.7946	0.9996
#4	-	0.3548	0.7998	0.9998
#5	-	0.3120	0.7766	0.9997
#6	-	0.3820	0.7743	0.9982
#7	-	0.4175	0.8164	0.9990
#8	-	0.3487	0.8112	0.9998
#9	-	0.3839	0.7483	0.9961
Average	-	0.3839	0.7920	0.9986

Table.7.2 Averaged Parametric Comparison of 06 Clustered Fusion Images of Primary (PGIMER) Dataset

Dataset	K-means	EM	MRFCM	ARKFCM
#1	-	0.3811	0.8195	0.5525
#2	-	0.4061	0.8533	0.6272
#3	-	0.3960	0.8298	0.9343
#4	-	0.4067	0.8409	0.9997
#5	-	0.4688	0.8843	0.4866
#6	-	0.4684	0.8573	0.6471
Average	-	0.4212	0.8475	0.7079

7.5 CONCLUSIONS

The detection of abnormalities using the fusion of brain CT and MR images is discussed in this research. Initially, the images are fused using NSCT and SWT based hybrid scheme. The fused images of two different datasets are clustered using four different clustering schemes. The analysis of abnormalities and normal tissues in the segmented fusion images is done visually and quantitatively. The visual analysis of segmented MR images and segmented fusion images of ARKFCM and MRFCM scheme is also done. It is observed from the visual analysis that the ARKFCM scheme outperforms other clustering schemes in the detection of abnormalities whereas, MRFCM scheme shows better clustering of the normal tissues. From the visual analysis of segmented MR images and segmented fusion images, it is concluded that the fusion process aids in segmentation in the detection of abnormalities. From the quantitative analysis, it is observed that the ARKFCM scheme outperforms the other schemes in most cases. The fusion of CT images with MRI helps in providing the bone, calcification and air information in the segmented image. The fusion process also helps in separating the edema and necrosis from the rest of the tumor. It aids in removing the intensity inhomogeneity effect of MRI in false clustering of neighboring tissues of similar intensity. The information obtained from the segmented fusion image can be beneficial in the better classification of brain diseases. The bone information in the segmented image can be utilized in identifying the accurate location of the tumor or other diseases w.r.t. the bone. This can be helpful for surgeons during brain surgery.

CHAPTER 8

CONCLUSIONS AND FUTURE SCOPE

8.1 CONCLUSIONS

Recent image scanning technologies like computed tomography (CT) and magnetic resonance imaging (MRI) provide structural information of human brain tissues in a complementary way i.e. CT imaging shows clear bone and calcification details whereas MRI images give clear parenchymal information. This research is performed to test the performance of fused CT and MR images in the detection of abnormalities. To achieve this goal the multimodality images are initially registered. The registered images are fused by developing the fusion algorithms. The fusion images are clustered using different schemes to find the abnormalities in the clustered images. To test the performance of clustering schemes in the detection of abnormalities, datasets from different sources are used. This chapter draws the overall conclusions of the research work presented in this thesis.

CT and MRI are the two most important imaging modalities which are extensively used by the radiologists for the diagnosis of brain diseases. It is observed during the collection of data that the CT and MR images differ in scaling, translation and rotation due to two different imaging modalities used in their acquisition. The posture of the patient also changes during the acquisition of two images. Hence, registration of CT and MR images is done as a pre-processing step before fusion. An intensity-based registration method is used which employs affine transform with a multi-resolution approach. Mutual information is used as the similarity metric and one plus one evolutionary algorithm is applied as an optimizer.

NSST based fusion methods which employ pulse coupled neural network-based activity measures such as spatial frequency or sum modified Laplacian, increase the computational complexity of the fusion algorithms. A few states of art methods have applied normalized NSCT or NSST transform coefficients as an external stimulus to PCNN which reduces the edge detail information. In order to reduce the computational complexity and to feed the better edge information to PCNN input, a novel fusion scheme is developed for NSST that is based on a simplified model of PCNN. The datasets consisting of computed tomography and T2-weighted magnetic resonance images of fifteen patients collected from internet repository and PGIMER, Chandigarh, India are used in this research. The source images are decomposed into base and detail sub-bands using NSST. The regional energy-based activity

measure with consistency verification is applied to fuse the approximation sub-band of NSST. The novel morphological gradient is fed as an external stimulus to PCNN to fuse detail sub-bands. The proposed method is compared with five states of the art fusion schemes namely DWT, SWT, NSCT-PCNN and NSST-PCNN based methods. The proposed method is compared with state of the art schemes visually and quantitatively. The ability of the fused images, to retain the local structural information, contrast, brightness, texture and edge details of different image features of source images, is observed. Parametric analysis is done using five fusion quality assessment parameters named MI, $Q^{AB/F}$, SF, SD and mean. The average value of MI, $Q^{AB/F}$, SF, SD and mean for the Harvard dataset are 2.9251, 0.5050, 29.1112, 86.4337 and 68.0380, respectively. The average value of MI, $Q^{AB/F}$, SF, SD and mean for the PGIMER dataset are 2.8997, 0.5754, 23.8672, 77.6422 and 49.7269, respectively. The computational time for Harvard and PGIMER dataset is 13.4894 seconds and 12.9710 seconds, respectively. It is observed that the developed morphological gradient-based NSST- PCNN fusion approach is superior in terms of retaining bone, cerebrospinal fluid and edema details of source images in the fused image and requires lesser computational time as compared to other states of the art PCNN based fusion schemes. As per the radiologists views, the fusion outcome of the developed scheme is suitable for monitoring, diagnosis and surgical procedures of various diseased conditions. The composite fusion images of the developed method can also be employed by medical professors, students and other professionals to study brain anatomy.

A hybrid fusion algorithm for multimodal images is developed which is based upon non-subsampled contourlet transform and stationary wavelet transform. This scheme combines complementary information obtained from SWT and NSCT. Computed tomography images, T1-weighted magnetic resonance images and T2-weighted MR images are fused using the developed method. Firstly the CT and MR images are decomposed into approximation and detail sub-bands using NSCT. A locally weighted sum of the square of the coefficients based fusion rule with consistency verification is used to fuse the detailed coefficients of NSCT. The SWT is employed to decompose approximation coefficients of NSCT into different sub-bands. The entropy of the square of the coefficients and weighted sum-modified Laplacian is employed as the fusion rules with SWT. This is specifically done to collect the coefficients from focused regions and to extract edge information from LF and HF sub-bands. The final output i.e. the fused image is obtained by employing the inverse NSCT. The research is verified by qualitative and quantitative parameters calculated

from the fused images. The expert radiologists views are also noted. The developed method is compared with four recent NSST based fusion methods and an adaptive sparse representation-based scheme. From the visual analysis, it is observed that the proposed scheme retained bone information of CT image and parenchyma, cerebrospinal fluid information of MR image with good resolution as compared to other methods. It is observed from the quantitative results that the average value of mutual information is 3.4320, the average standard deviation value is 83.6900, the spatial frequency value is 27.5813, edge information based quality metric value is 0.5585 and mean parameter value is 65.2462 for internet repository dataset. The average value of these parameters is 3.2479, 76.2225, 24.5255, 0.5783 and 52.8101, respectively for the PGIMER dataset. It is observed that the modified approach gave improved results for mutual information, standard deviation, mean, edge information based quality metric and spatial frequency. This validates better texture, contrast, brightness, edge details and better clarity of the fused images of the developed method as compared to other schemes. As per the radiologists the scheme provides better fusion results. The developed method is helpful to radiologists in surgical procedures as the distance to the diseased tissues from the overlying skull bone is clearly visible in the fused image.

In the third approach, a human visual system inspired fusion scheme is developed which is based upon Gaussian weighted pixel intensities and smallest uni value segment assimilating nucleus (SUSAN). A new computationally efficient NSST based fusion scheme for CT-MRI images is proposed. The different image pairs of Harvard and PGIMER datasets are fused together to test the performance of the developed methodology. Initially, the images are decomposed through NSST into general and detail features. The local sum of Gaussian weighted pixel intensities and SUSAN based activity measures are proposed with NSST for faster execution of the algorithm as well as to obtain better bone and disease features in the fusion outcome. Visual and parametric comparison of the proposed scheme is done through 5 traditional fusion algorithms named adaptive block-based scheme, SWT based method, adaptive sparse representation and denoising, convolutional sparse representation based fusion and NSST with regional energy and morphological gradient motivated PCNN based scheme. Parametric analysis is done using MI, $Q^{AB/F}$, SD, SF and mean parameters. In addition, Wilcoxon signed ranks test is also applied to compare different methods scientifically with the proposed fusion scheme. The fused images are also shown to expert radiologists. It is observed from the visual analysis that the presented method is better in

retaining bone, calcification, cerebrospinal fluid, edema and tumor details of the source images. From the parametric analysis, it is observed that the average value of MI, $Q^{AB/F}$, SD, SF and mean parameters is 3.7406, 0.5346, 88.1506, 27.4274 and 68.5800, respectively for Harvard dataset. The average value of MI, $Q^{AB/F}$, SD, SF and mean parameters is 3.5392, 0.5669, 79.7867, 17.8293 and 51.0934, respectively for the PGIMER dataset. The value of most of these parameters is found to be better than other compared schemes. The computation time taken by the developed scheme for Harvard and PGIMER dataset is 9.7250 and 23.5961, respectively and is faster than other classical fusion schemes. From the p values of various performance parameters obtained using Wilcoxon signed ranks test it is concluded that there exists a significant difference between the developed methodology and the other schemes. This scientifically proves the superiority of the developed scheme as compared to other schemes. The fusion images of the proposed methodology are suitable for locating the site of biopsy externally or incision location in the bone of the brain skull with minimum diagnostic time as per the radiologist's views.

It is observed from the past work that there are very few studies in the detection of diseases using fused images where clustering or segmentation methods are employed. Hence, in order to detect the abnormalities, fusion images obtained from the developed NSCT-SWT based hybrid fusion scheme are employed as input to four different types of clustering schemes named as (i) K-means clustering (ii) expectation-maximization based clustering (iii) morphological reconstruction based FCM clustering (iv) adaptive regularised kernel-based FCM clustering. NSCT-SWT based fusion scheme is employed in clustering as it gives better edge information and clarity of the fused image. The fused images of diseases like acute stroke (writes but can't read), acute stroke (speech arrest), meningioma, sarcoma, hypertensive encephalopathy, metastatic bronchogenic carcinoma, multiple embolic infarctions, fatal stroke, glioma, calcified tumor, fungal infection and post-operative tumor are used in clustering. The clustered fusion images thus obtained are compared visually and quantitatively using the partition coefficient parameter. It is observed from the visual clustering analysis of fusion images that the ARKFCM scheme provides better detection of abnormalities as compared to other schemes, whereas the MRFCM scheme clusters normal tissues finely in comparison to other schemes. The above is also confirmed by the neuro-radiologists. From the quantitative analysis, it is observed that the ARKFCM scheme obtains better values of the partition coefficient parameter as compared to other schemes for

Harvard dataset and a few cases of PGIMER dataset. This shows the better clustering performance of this scheme for abnormality detection.

The clustered MR images and clustered fusion images obtained from MRFCM and ARKFCM clustering methods are also compared visually. It is observed from the comparison of clustered MR images and clustered fusion images that the fusion image clustering has a clearer bone, calcification and air information of the CT image and edema along with other abnormality information of MR image.

Hence, it is concluded that the fused images of the developed methods aid the radiologists in having a combined flavor of both CT and MR image in a single image and reduce the time which may be required for evaluating both the images and trying to mentally fuse them to reach a diagnosis. It is also concluded that fusion process assists in better clustering of the tissues, especially in separating the edema and necrosis from the rest of the tumor. It also helps in clustering the intensity inhomogeneous regions belonging to similar tissues in a single class. The clustered images of the developed scheme can be employed in enhancing the tumor and edema segmentation accuracy, computation of distance of abnormality from the skull bone and also in image classification.

8.2 FUTURE SCOPE OF THE STUDY

In future the proposed schemes can be implemented using other types of multi-resolution transforms and can be tested on different types of medical images such as diffusion-weighted imaging (DWI) with CT or MRI, susceptibility weighted imaging (SWI) with CT or MRI and ultrasound images with CT or MRI. The multimodal images of other organs can be used. Moreover, the proposed fusion rules can also be modified. The proposed fusion schemes can be extended to color images such as SPECT with MRI or PET with MRI. The developed methods can be tested on multi-focus, remote sensing or infrared and visible images.

[1] A.A. Lammertsma, PET/SPECT: functional imaging beyond flow, Vision research, 41 (2001) 1277-1281.

[2] P. Ganasala, V. Kumar, Multimodality medical image fusion based on new features in NSST domain, Biomedical Engineering Letters, 4 (2014) 414-424.

[3] P. Ganasala, V. Kumar, Feature-motivated simplified adaptive PCNN-based medical image fusion algorithm in NSST domain, Journal of digital imaging, 29 (2016) 73-85.

[4] B. Miles, I.B. Ayed, M.W. Law, G. Garvin, A. Fenster, S. Li, Spine image fusion via graph cuts, IEEE Transactions on Biomedical Engineering, 60 (2013) 1841-1850.

[5] H.H. Schild, MRI Made Easy:(--well Almost), Berlex Laboratories, 1992.

[6] P. Kaur, A. Sharma, A. Nigam, A. Bhavsar, MR-Srnet: Transformation of Low Field MR Images to High Field MR Images, in: 2018 25th IEEE International Conference on Image Processing (ICIP), IEEE, 2018, pp. 2057-2061.

[7] R. Soundrapandiyan, M. Karuppiah, S. Kumari, S. Kumar Tyagi, F. Wu, K.H. Jung, An efficient DWT and intuitionistic fuzzy based multimodality medical image fusion, International Journal of Imaging Systems and Technology, 27 (2017) 118-132.

[8] H. Singh, J. Raj, G. Kaur, T. Meitzler, Image fusion using fuzzy logic and applications, in: 2004 IEEE International Conference on Fuzzy Systems (IEEE Cat. No. 04CH37542), IEEE, 2004, pp. 337-340.

[9] V.A. Zimmer, M.Á.G. Ballester, G. Piella, Multimodal image registration using Laplacian commutators, Information Fusion, 49 (2019) 130-145.

[10] S.F. Nemec, M.A. Donat, S. Mehrain, K. Friedrich, C. Krestan, C. Matula, H. Imhof, C. Czerny, CT–MR image data fusion for computer assisted navigated neurosurgery of temporal bone tumors, European journal of radiology, 62 (2007) 192-198.

[11] A.C. Paulino, W.L. Thorstad, T. Fox, Role of fusion in radiotherapy treatment planning, in: Seminars in nuclear medicine, Elsevier, 2003, pp. 238-243.

[12] Y. Zhou, M. Omar, Pixel-Level fusion for infrared and visible acquisitions, International Journal of Optomechatronics, 3 (2009) 41-53.

[13] P.H. Venkatrao, S.S. Damodar, HWFusion: Holoentropy and SP-Whale optimisation-based fusion model for magnetic resonance imaging multimodal image fusion, IET Image Processing, 12 (2017) 572-581.

[14] M. Kumar, S. Dass, A total variation-based algorithm for pixel-level image fusion, IEEE Transactions on Image Processing, 18 (2009) 2137-2143.

[15] S. Li, X. Kang, L. Fang, J. Hu, H. Yin, Pixel-level image fusion: A survey of the state of the art, Information Fusion, 33 (2017) 100-112.

[16] C. Kwan, B. Chou, L.-Y.M. Kwan, J. Larkin, B. Ayhan, J.F. Bell, H. Kerner, Demosaicing enhancement using pixel-level fusion, Signal, Image and Video Processing, 12 (2018) 749-756.

[17] P. Kavitha, K. Vijaya, Optimal feature-level fusion and layered k-support vector machine for spoofing face detection, Multimedia Tools and Applications, 77 (2018) 26509-26543.

[18] E.R. Vimina, K.P. Jacob, Feature fusion method using BoVW framework for enhancing image retrieval, IET Image Processing, 13 (2019) 1979-1985.

[19] Y. Xin, L. Kong, Z. Liu, C. Wang, H. Zhu, M. Gao, C. Zhao, X. Xu, Multimodal feature-level fusion for biometrics identification System on IoMT platform, IEEE Access, 6 (2018) 21418-21426.

[20] P.K.R. Yelampalli, J. Nayak, V.H. Gaidhane, Medical image rigid registration using a novel binary feature descriptor and modified affine transform, IET Image Processing, 12 (2017) 337-344.

[21] W.K. Pratt, Correlation techniques of image registration, IEEE transactions on Aerospace and Electronic Systems, 10 (1974) 353-358.

[22] M. Nejati, H. Pourghassem, Multiresolution image registration in digital X-ray angiography with intensity variation modeling, Journal of medical systems, 38 (2014) 10.

[23] K. Aghajani, R. Yousefpour, M. Zohrehvandi, A robust non-local total-variation based image registration method under illumination changes in medical applications, Biomedical Signal Processing and Control, 49 (2019) 96-112.

[24] M. Freiman, M. Werman, L. Joskowicz, A curvelet-based patient-specific prior for accurate multi-modal brain image rigid registration, Medical image analysis, 15 (2011) 125-132.

[25] M. Bhattacharya, A. Das, Registration of multimodality medical imaging of brain using particle swarm optimization, in: Proceedings of the first international

conference on intelligent human computer interaction, Springer, 2009, pp. 131-139.

[26] A. Bardera, I. Boada, M. Feixas, J. Rigau, M. Sbert, Multiresolution image registration based on tree data structures, Graphical Models, 73 (2011) 111-126.

[27] P. Xu, D. Yao, A study on medical image registration by mutual information with pyramid data structure, Computers in Biology and Medicine, 37 (2007) 320-327.

[28] S.i. Kaneko, Y. Satoh, S. Igarashi, Using selective correlation coefficient for robust image registration, Pattern Recognition, 36 (2003) 1165-1173.

[29] F. Maes, D. Vandermeulen, P. Suetens, Comparative evaluation of multiresolution optimization strategies for multimodality image registration by maximization of mutual information, Medical image analysis, 3 (1999) 373-386.

[30] J.P. Pluim, J.A. Maintz, M.A. Viergever, Mutual-information-based registration of medical images: a survey, IEEE transactions on medical imaging, 22 (2003) 986-1004.

[31] Y. Yang, Y. Que, S.-Y. Huang, P. Lin, Technique for multi-focus image fusion based on fuzzy-adaptive pulse-coupled neural network, Signal, Image and Video Processing, 11 (2017) 439-446.

[32] T.-M. Tu, S.-C. Su, H.-C. Shyu, P.S. Huang, A new look at IHS-like image fusion methods, Information fusion, 2 (2001) 177-186.

[33] R.M. Rangayyan, R.J. Ferrari, J.L. Desautels, A.F. Frere, Directional analysis of images with Gabor wavelets, in: Proceedings 13th Brazilian Symposium on Computer Graphics and Image Processing (Cat. No. PR00878), IEEE, 2000, pp. 170-177.

[34] J.-L. Starck, E.J. Candès, D.L. Donoho, The curvelet transform for image denoising, IEEE Transactions on image processing, 11 (2002) 670-684.

[35] A.L. Da Cunha, J. Zhou, M.N. Do, The nonsubsampled contourlet transform: theory, design, and applications, IEEE transactions on image processing, 15 (2006) 3089-3101.

[36] B. Han, Framelets and wavelets: Algorithms, analysis, and applications, Springer, 2018.

[37] Q. Jiang, X. Jin, J. Hou, S.-J. Lee, S. Yao, Multi-sensor image fusion based on Interval Type-2 Fuzzy Sets and regional features in Nonsubsampled Shearlet Transform domain, IEEE Sensors Journal, 18 (2018) 2494-2505.

[38] G. Bhatnagar, Q.J. Wu, Z. Liu, Human visual system inspired multi-modal medical image fusion framework, Expert Systems with Applications, 40 (2013) 1708-1720.

[39] W. Kong, Technique for image fusion based on NSST domain INMF, Optik, 125 (2014) 2716-2722.

[40] G. Pajares, J.M. De La Cruz, A wavelet-based image fusion tutorial, Pattern recognition, 37 (2004) 1855-1872.

[41] Y. Yang, Multiresolution Image Fusion Based on Wavelet Transform By Using a Novel Technique for Selection Coefficients, Journal of Multimedia, 6 (2011) 91-98.

[42] H. Ma, C. Jia, S. Liu, Multisource image fusion based on wavelet transform, International Journal of Information Technology, 11 (2005) 81-91.

[43] W. Kong, L. Zhang, Y. Lei, Novel fusion method for visible light and infrared images based on NSST–SF–PCNN, Infrared Physics & Technology, 65 (2014) 103-112.

[44] X. Liu, Y. Zhou, J. Wang, Image fusion based on shearlet transform and regional features, AEU-international journal of electronics and communications, 68 (2014) 471-477.

[45] P. Ganasala, V. Kumar, CT and MR image fusion scheme in nonsubsampled contourlet transform domain, Journal of digital imaging, 27 (2014) 407-418.

[46] R. Peng, P.K. Varshney, A human visual system-driven image segmentation algorithm, Journal of Visual Communication and Image Representation, 26 (2015) 66-79.

[47] S. Manikandan, K. Ramar, M.W. Iruthayarajan, K. Srinivasagan, Multilevel thresholding for segmentation of medical brain images using real coded genetic algorithm, Measurement, 47 (2014) 558-568.

[48] S. Banerjee, S. Mitra, B.U. Shankar, Single seed delineation of brain tumor using multi-thresholding, Information Sciences, 330 (2016) 88-103.

[49] N. Nabizadeh, M. Kubat, Brain tumors detection and segmentation in MR images: Gabor wavelet vs. statistical features, Computers & Electrical Engineering, 45 (2015) 286-301.

[50] P. Shanthakumar, P. Ganeshkumar, Performance analysis of classifier for brain tumor detection and diagnosis, Computers & Electrical Engineering, 45 (2015) 302-311.

[51] S. Madhukumar, N. Santhiyakumari, Evaluation of k-Means and fuzzy C-means segmentation on MR images of brain, The Egyptian Journal of Radiology and Nuclear Medicine, 46 (2015) 475-479.

[52] V. Caselles, R. Kimmel, G. Sapiro, Geodesic active contours, International journal of computer vision, 22 (1997) 61-79.

[53] L. Vincent, P. Soille, Watersheds in digital spaces: an efficient algorithm based on immersion simulations, IEEE Transactions on Pattern Analysis & Machine Intelligence, 13 (1991) 583-598.

[54] F. Yi, I. Moon, Image segmentation: A survey of graph-cut methods, in: 2012 International Conference on Systems and Informatics (ICSAI2012), IEEE, 2012, pp. 1936-1941.

[55] T. Kohonen, T. Honkela, Kohonen network, Scholarpedia, 2 (2007) 1568.

[56] V. Duay, N. Houhou, J.-P. Thiran, Atlas-based segmentation of medical images locally constrained by level sets, in: IEEE International Conference on Image Processing 2005, IEEE, 2005, pp. II-1286.

[57] S. Li, J.T. Kwok, Y. Wang, Combination of images with diverse focuses using the spatial frequency, Information fusion, 2 (2001) 169-176.

[58] A.V. Vanmali, S.S. Deshmukh, V.M. Gadre, Low complexity detail preserving multi-exposure image fusion for images with balanced exposure, in: 2013 National Conference on Communications (NCC), IEEE, 2013, pp. 1-5.

[59] T. Wan, C. Zhu, Z. Qin, Multifocus image fusion based on robust principal component analysis, Pattern Recognition Letters, 34 (2013) 1001-1008.

[60] S. Li, J.T. Kwok, Y. Wang, Multifocus image fusion using artificial neural networks, Pattern Recognition Letters, 23 (2002) 985-997.

[61] Z. Wang, Y. Ma, Medical image fusion using m-PCNN, Information Fusion, 9 (2008) 176-185.

[62] P. Geng, S. Liu, S. Zhuang, Multimodal medical image fusion by adaptive manifold filter, Computational and Mathematical Methods in Medicine, 2015 (2015) 1-9.

[63] P.J. Burt, E.H. Adelson, Merging images through pattern decomposition, in: Applications of Digital Image Processing VIII, International Society for Optics and Photonics, 1985, pp. 173-181.

[64] A. Toet, Image fusion by a ratio of low-pass pyramid, Pattern Recognition Letters, 9 (1989) 245-253.

[65] S. Mukhopadhyay, B. Chanda, Fusion of 2D grayscale images using multiscale morphology, Pattern Recognition, 34 (2001) 1939-1949.

[66] J. Kovacevic, M. Vetterli, Nonseparable two-and three-dimensional wavelets, IEEE Transactions on Signal Processing, 43 (1995) 1269-1273.

[67] Z. Zhang, R.S. Blum, A categorization of multiscale-decomposition-based image fusion schemes with a performance study for a digital camera application, Proceedings of the IEEE, 87 (1999) 1315-1326.

[68] T. Ranchin, L. Wald, Fusion of high spatial and spectral resolution images: The ARSIS concept and its implementation, Photogrammetic engineering and remote sensing, ASPRS American society for photogrammetry, 66 (2000) 49-61.

[69] H. Li, B. Manjunath, S.K. Mitra, Multisensor image fusion using the wavelet transform, Graphical models and image processing, 57 (1995) 235-245.

[70] S. Bedi, J. Agarwal, Implementation of hybrid image fusion technique for feature enhancement in medical diagnosis. Human-centric Comput, Inf. Sci, 5 (2015) 1-17.

[71] L. Xu, J. Du, Q. Hu, Q. Li, Feature-based image fusion with a uniform discrete curvelet transform, International Journal of Advanced Robotic Systems, 10 (2013) 255.

[72] M.N. Do, M. Vetterli, The contourlet transform: an efficient directional multiresolution image representation, IEEE Transactions on image processing, 14 (2005) 2091-2106.

[73] G. Guorong, X. Luping, F. Dongzhu, Multi-focus image fusion based on non-subsampled shearlet transform, IET Image Processing, 7 (2013) 633-639.

[74] Y. Yang, D.S. Park, S. Huang, N. Rao, Medical image fusion via an effective wavelet-based approach, EURASIP Journal on Advances in Signal Processing, 2010 (2010) 1-13.

[75] R. Vijayarajan, S. Muttan, Discrete wavelet transform based principal component averaging fusion for medical images, AEU-International Journal of Electronics and Communications, 69 (2015) 896-902.

[76] R. Singh, A. Khare, Fusion of multimodal medical images using Daubechies complex wavelet transform–A multiresolution approach, Information Fusion, 19 (2014) 49-60.

[77] M. Bhattacharya, A. Das, M. Chandana, GA-based multiresolution fusion of segmented brain images using PD-, T1-and T2-weighted MR modalities, Neural Computing and Applications, 21 (2012) 1433-1447.

[78] A. Ellmauthaler, C.L. Pagliari, E.A. Da Silva, Multiscale image fusion using the undecimated wavelet transform with spectral factorization and nonorthogonal filter banks, IEEE Transactions on image processing, 22 (2012) 1005-1017.

[79] F.E. Ali, I. El-Dokany, A. Saad, F. Abd El-Samie, A curvelet transform approach for the fusion of MR and CT images, Journal of Modern Optics, 57 (2010) 273-286.

[80] L. Yang, B. Guo, W. Ni, Multimodality medical image fusion based on multiscale geometric analysis of contourlet transform, Neurocomputing, 72 (2008) 203-211.

[81] L. Wang, B. Li, L.-F. Tian, Multi-modal medical image fusion using the inter-scale and intra-scale dependencies between image shift-invariant shearlet coefficients, Information Fusion, 19 (2014) 20-28.

[82] S. Das, M.K. Kundu, A neuro-fuzzy approach for medical image fusion, IEEE transactions on biomedical engineering, 60 (2013) 3347-3353.

[83] S.M. Darwish, Multi-level fuzzy contourlet-based image fusion for medical applications, IET image processing, 7 (2013) 694-700.

[84] G. Bhatnagar, Q.J. Wu, Z. Liu, A new contrast based multimodal medical image fusion framework, Neurocomputing, 157 (2015) 143-152.

[85] P.S. Gomathi, B. Kalaavathi, Multimodal medical image fusion in non-subsampled contourlet transform domain, Circuits and Systems, 7 (2016) 1598.

[86] Q.-G. Miao, C. Shi, P.-F. Xu, M. Yang, Y.-B. Shi, A novel algorithm of image fusion using shearlets, Optics Communications, 284 (2011) 1540-1547.

[87] M. Yin, W. Liu, X. Zhao, Y. Yin, Y. Guo, A novel image fusion algorithm based on nonsubsampled shearlet transform, Optik-international journal for light and electron optics, 125 (2014) 2274-2282.

[88] X. Liu, W. Mei, H. Du, J. Bei, A novel image fusion algorithm based on nonsubsampled shearlet transform and morphological component analysis, Signal, Image and Video Processing, 10 (2016) 959-966.

[89] S. Cheng, M. Qiguang, X. Pengfei, A novel algorithm of remote sensing image fusion based on Shearlets and PCNN, Neurocomputing, 117 (2013) 47-53.

[90] Q. Xiao-Bo, Y. Jing-Wen, X. Hong-Zhi, Z. Zi-Qian, Image fusion algorithm based on spatial frequency-motivated pulse coupled neural networks in nonsubsampled contourlet transform domain, Acta Automatica Sinica, 34 (2008) 1508-1514.

[91] T. Xiang, L. Yan, R. Gao, A fusion algorithm for infrared and visible images based on adaptive dual-channel unit-linking PCNN in NSCT domain, Infrared Physics & Technology, 69 (2015) 53-61.

[92] S. Das, M.K. Kundu, NSCT-based multimodal medical image fusion using pulse-coupled neural network and modified spatial frequency, Medical & biological engineering & computing, 50 (2012) 1105-1114.

[93] J. Wang, Q. Li, Z. Jia, N. Kasabov, J. Yang, A novel multi-focus image fusion method using PCNN in nonsubsampled contourlet transform domain, Optik-International Journal for Light and Electron Optics, 126 (2015) 2508-2511.

[94] S. Singh, D. Gupta, R. Anand, V. Kumar, Nonsubsampled shearlet based CT and MR medical image fusion using biologically inspired spiking neural network, Biomedical Signal Processing and Control, 18 (2015) 91-101.

[95] W. Kong, B. Wang, Y. Lei, Technique for infrared and visible image fusion based on non-subsampled shearlet transform and spiking cortical model, Infrared Physics & Technology, 71 (2015) 87-98.

[96] X. Jin, R. Nie, D. Zhou, Q. Wang, K. He, Multifocus color image fusion based on NSST and PCNN, Journal of Sensors, 2016 (2016) 1-12.

[97] M. Yin, X. Liu, Y. Liu, X. Chen, Medical image fusion with parameter-adaptive pulse coupled neural network in nonsubsampled shearlet transform domain, IEEE Transactions on Instrumentation and Measurement, 68 (2018) 49-64.

[98] Z. Baohua, L. Xiaoqi, J. Weitao, A multi-focus image fusion algorithm based on an improved dual-channel PCNN in NSCT domain, Optik-International Journal for Light and Electron Optics, 124 (2013) 4104-4109.

[99] S. Li, B. Yang, Multifocus image fusion by combining curvelet and wavelet transform, Pattern recognition letters, 29 (2008) 1295-1301.

[100] S. Li, B. Yang, Hybrid multiresolution method for multisensor multimodal image fusion, IEEE Sensors Journal, 10 (2010) 1519-1526.

[101] H. Zhou, An stationary wavelet transform and curvelet transform based infrared and visible images fusion algorithm, International Journal of Digital Content Technology and its Applications, 6 (2012) 144-151.

[102] Y. Yang, S. Tong, S. Huang, P. Lin, Y. Fang, A hybrid method for multi-focus image fusion based on fast discrete curvelet transform, IEEE Access, 5 (2017) 14898-14913.

[103] X. Jin, Q. Jiang, S. Yao, D. Zhou, R. Nie, S.-J. Lee, K. He, Infrared and visual image fusion method based on discrete cosine transform and local spatial frequency in discrete stationary wavelet transform domain, Infrared Physics & Technology, 88 (2018) 1-12.

[104] A. Toet, L.J. Van Ruyven, J.M. Valeton, Merging thermal and visual images by a contrast pyramid, Optical engineering, 28 (1989) 287789.

[105] C. He, Q. Liu, H. Li, H. Wang, Multimodal medical image fusion based on IHS and PCA, Procedia Engineering, 7 (2010) 280-285.

[106] X. Bai, Image analysis through feature extraction by using top-hat transform-based morphological contrast operator, Applied optics, 52 (2013) 3777-3789.

[107] J. Wang, Q. Li, Z. Jia, N. Kasabov, J. Yang, A novel multi-focus image fusion method using PCNN in nonsubsampled contourlet transform domain, Optik, 126 (2015) 2508-2511.

[108] P. Tiwari, J. Sachdeva, C.K. Ahuja, N. Khandelwal, Computer aided diagnosis system-a decision support system for clinical diagnosis of brain tumours, International Journal of Computational Intelligence Systems, 10 (2017) 104-119.

[109] T. Wang, I. Cheng, A. Basu, Fluid vector flow and applications in brain tumor segmentation, IEEE Transactions on Biomedical Engineering, 56 (2009) 781-789.

[110] J. Sachdeva, V. Kumar, I. Gupta, N. Khandelwal, C.K. Ahuja, A novel content-based active contour model for brain tumor segmentation, Magnetic resonance imaging, 30 (2012) 694-715.

[111] K. Xie, J. Yang, Z. Zhang, Y. Zhu, Semi-automated brain tumor and edema segmentation using MRI, European journal of radiology, 56 (2005) 12-19.

[112] C. Xu, J.L. Prince, Snakes, shapes, and gradient vector flow, IEEE Transactions on image processing, 7 (1998) 359-369.

[113] X. Xie, M. Mirmehdi, MAC: Magnetostatic active contour model, IEEE Transactions on pattern analysis and machine intelligence, 30 (2008) 632-646.

[114] C. Vijayakumar, G. Damayanti, R. Pant, C. Sreedhar, Segmentation and grading of brain tumors on apparent diffusion coefficient images using self-organizing maps, Computerized Medical Imaging and Graphics, 31 (2007) 473-484.

[115] N. Zhang, S. Ruan, S. Lebonvallet, Q. Liao, Y. Zhu, Kernel feature selection to fuse multi-spectral MRI images for brain tumor segmentation, Computer Vision and Image Understanding, 115 (2011) 256-269.

[116] N. Torbati, A. Ayatollahi, A. Kermani, An efficient neural network based method for medical image segmentation, Computers in biology and medicine, 44 (2014) 76-87.

[117] A. Abdullah, A. Hirayama, S. Yatsushiro, M. Matsumae, K. Kuroda, Cerebrospinal fluid image segmentation using spatial fuzzy clustering method with improved evolutionary expectation maximization, in: 2013 35th Annual International Conference of the IEEE Engineering in Medicine and Biology Society (EMBC), IEEE, 2013, pp. 3359-3362.

[118] S. AlZubi, N. Islam, M. Abbod, Multiresolution analysis using wavelet, ridgelet, and curvelet transforms for medical image segmentation, Journal of Biomedical Imaging, 2011 (2011) 1-18.

[119] E. Abdel-Maksoud, M. Elmogy, R. Al-Awadi, Brain tumor segmentation based on a hybrid clustering technique, Egyptian Informatics Journal, 16 (2015) 71-81.

[120] J.E. Romero, J.V. Manjón, J. Tohka, P. Coupé, M. Robles, NABS: non-local automatic brain hemisphere segmentation, Magnetic resonance imaging, 33 (2015) 474-484.

[121] C. Ledig, R.A. Heckemann, A. Hammers, J.C. Lopez, V.F. Newcombe, A. Makropoulos, J. Lötjönen, D.K. Menon, D. Rueckert, Robust whole-brain segmentation: application to traumatic brain injury, Medical image analysis, 21 (2015) 40-58.

[122] D. Summers, Harvard Whole Brain Atlas: www. med. harvard. edu/AANLIB/home. html, Journal of Neurology, Neurosurgery & Psychiatry, 74 (2003) 288-288.

[123] C. Du, S. Gao, Multi-focus image fusion algorithm based on pulse coupled neural networks and modified decision map, Optik-International Journal for Light and Electron Optics, 157 (2018) 1003-1015.

[124] C.A. Xydeas, V. Petrovic, Objective image fusion performance measure, Electronics letters, 36 (2000) 308-309.

[125] J.C. Bezdek, Pattern recognition with fuzzy objective function algorithms, Springer Science & Business Media, 2013.

[126] C. sheng Li, The improved partition coefficient, Procedia Engineering, 24 (2011) 534-538.

[127] D. Gupta, Nonsubsampled shearlet domain fusion techniques for CT–MR neurological images using improved biological inspired neural model, Biocybernetics and Biomedical Engineering, 38 (2018) 262-274.

[128] A. Das, M. Bhattacharya, Affine-based registration of CT and MR modality images of human brain using multiresolution approaches: comparative study on genetic algorithm and particle swarm optimization, Neural Computing and Applications, 20 (2011) 223-237.

[129] D. Mattes, D.R. Haynor, H. Vesselle, T.K. Lewellen, W. Eubank, PET-CT image registration in the chest using free-form deformations, IEEE transactions on medical imaging, 22 (2003) 120-128.

[130] P. Thévenaz, M. Unser, Optimization of mutual information for multiresolution image registration, IEEE transactions on image processing, 9 (2000) 2083-2099.

[131] W. Wan, Y. Yang, H.J. Lee, Practical remote sensing image fusion method based on guided filter and improved SML in the NSST domain, Signal, Image and Video Processing, 12 (2018) 959-966.

[132] W. Zhi-she, Y. Feng-bao, P. Zhi-hao, C. Lei, J. Li-e, Multi-sensor image enhanced fusion algorithm based on NSST and top-hat transformation, Optik-International Journal for Light and Electron Optics, 126 (2015) 4184-4190.

[133] A. Garnica-Carrillo, F. Calderon, J. Flores, Multi-focus image fusion by local optimization over sliding windows, Signal, Image and Video Processing, 12 (2018) 869-876.

[134] C. Solomon, T. Breckon, Fundamentals of Digital Image Processing: A practical approach with examples in Matlab, John Wiley & Sons, 2011.

[135] S. Li, B. Yang, J. Hu, Performance comparison of different multi-resolution transforms for image fusion, Information Fusion, 12 (2011) 74-84.

[136] Q. Miao, C. Shi, P. Xu, M. Yang, Y. Shi, Multi-focus image fusion algorithm based on shearlets, Chinese Optics Letters, 9 (2011) 041001.

[137] L. Yang, B. Guo, W. Ni, Multimodality medical image fusion based on multiscale geometric analysis of contourlet transform, Neurocomputing, 72 (2008) 203-211.

[138] T. Li, Y. Wang, Biological image fusion using a NSCT based variable-weight method, Information Fusion, 12 (2011) 85-92.

[139] S. Yang, M. Wang, Y. Lu, W. Qi, L. Jiao, Fusion of multiparametric SAR images based on SW-nonsubsampled contourlet and PCNN, Signal Processing, 89 (2009) 2596-2608.

[140] R.M. Rao, Wavelet transforms: Introduction to theory and applications, Pearson Education India, 1998.

[141] Y. Liu, Z. Wang, Simultaneous image fusion and denoising with adaptive sparse representation, IET Image Processing, 9 (2015) 347-357.

[142] S.D. Ramlal, J. Sachdeva, C.K. Ahuja, N. Khandelwal, Multimodal medical image fusion using non-subsampled shearlet transform and pulse coupled neural network incorporated with morphological gradient, Signal, Image and Video Processing, 12 (2018) 1479-1487.

[143] M. Yin, X. Liu, Y. Liu, X. Chen, Medical Image Fusion With Parameter-Adaptive Pulse Coupled Neural Network in Nonsubsampled Shearlet Transform Domain, IEEE Transactions on Instrumentation and Measurement, 68 (2019) 49-64.

[144] W. Jiang, X. Yang, W. Wu, K. Liu, A. Ahmad, A.K. Sangaiah, G. Jeon, Medical images fusion by using weighted least squares filter and sparse representation, Computers & Electrical Engineering, 67 (2018) 252-266.

[145] R.C. Krempien, S. Daeuber, F.W. Hensley, M. Wannenmacher, W. Harms, Image fusion of CT and MRI data enables improved target volume definition in 3D-brachytherapy treatment planning, Brachytherapy, 2 (2003) 164-171.

[146] Y. Liu, X. Chen, R.K. Ward, Z.J. Wang, Image fusion with convolutional sparse representation, IEEE signal processing letters, 23 (2016) 1882-1886.

[147] Y. Liu, X. Chen, J. Cheng, H. Peng, A medical image fusion method based on convolutional neural networks, in: Information Fusion (Fusion), 2017 20th International Conference on, IEEE, 2017, pp. 1-7.

[148] E. Daniel, J. Anitha, K. Kamaleshwaran, I. Rani, Optimum spectrum mask based medical image fusion using Gray Wolf Optimization, Biomedical Signal Processing and Control, 34 (2017) 36-43.

[149] E. Daniel, J. Anitha, J. Gnanaraj, Optimum laplacian wavelet mask based medical image using hybrid cuckoo search–grey wolf optimization algorithm, Knowledge-Based Systems, 131 (2017) 58-69.

[150] X. Liu, W. Mei, H. Du, Structure tensor and nonsubsampled shearlet transform based algorithm for CT and MRI image fusion, Neurocomputing, 235 (2017) 131-139.

[151] Z. Liu, E. Blasch, V. John, Statistical comparison of image fusion algorithms: Recommendations, Information Fusion, 36 (2017) 251-260.

[152] S.M. Smith, J.M. Brady, SUSAN—a new approach to low level image processing, International journal of computer vision, 23 (1997) 45-78.

[153] Y. Liu, Z. Wang, Multi-focus image fusion based on wavelet transform and adaptive block, Journal of Image and Graphics, 18 (2013) 1435-1444.

[154] S.D. Ramlal, J. Sachdeva, C.K. Ahuja, N. Khandelwal, Brain CT and MR Image Fusion Framework Based on Stationary Wavelet Transform, in: Advances in Computer and Computational Sciences, Springer, 2018, pp. 445-453.

[155] S. Aswathy, S. Kumar, G. Glan Devadhas, Quick detection of brain tumor using a combination of EM and level set method, Indian Journal of Science and Technology, 8 (2015) 74-82.

[156] E.H. Kale, E.U. Mumcuoglu, S. Hamcan, Automatic segmentation of human facial tissue by MRI–CT fusion: A feasibility study, Computer methods and programs in biomedicine, 108 (2012) 1106-1120.

[157] E. Şener, E.U. Mumcuoglu, S. Hamcan, Bayesian segmentation of human facial tissue using 3D MR-CT information fusion, resolution enhancement and partial volume modelling, Computer methods and programs in biomedicine, 124 (2016) 31-44.

[158] G. Gilanie, U.I. Bajwa, M.M. Waraich, Z. Habib, Computer aided diagnosis of brain abnormalities using texture analysis of MRI images, International Journal of Imaging Systems and Technology, 29 (2019) 260-271.

[159] J. MacQueen, Some methods for classification and analysis of multivariate observations, in: Proceedings of the fifth Berkeley symposium on mathematical statistics and probability, Oakland, CA, USA, 1967, pp. 281-297.

[160] H. Zhi-kai, L. De-Hui, Unsupervised Image Segmentation Using EM algorithm by Histogram, in: 2007 3rd International conference on Advanced intelligent computing theories and applications (ICIC), 2007, pp. 1275-1282.

[161] T. Lei, X. Jia, Y. Zhang, L. He, H. Meng, A.K. Nandi, Significantly fast and robust fuzzy c-means clustering algorithm based on morphological reconstruction and membership filtering, IEEE Transactions on Fuzzy Systems, 26 (2018) 3027-3041.

[162] A. Elazab, C. Wang, F. Jia, J. Wu, G. Li, Q. Hu, Segmentation of brain tissues from magnetic resonance images using adaptively regularized kernel-based fuzzy-means clustering, Computational and mathematical methods in medicine, 2015 (2015) 1-13.

[163] X. Wang, J.M. Garibaldi, A comparison of fuzzy and non-fuzzy clustering techniques in cancer diagnosis, in: Proceedings of the 2nd International Conference in Computational Intelligence in Medicine and Healthcare, BIOPATTERN Conference, Costa da Caparica, Lisbon, Portugal, 2005.

[164] Z. Cebeci, F. Yildiz, Comparison of K-means and Fuzzy C-means algorithms on different cluster structures, Agrárinformatika/journal of agricultural informatics, 6 (2015) 13-23.

[165] R.M. Prakash, R.S.S. Kumari, Spatial fuzzy C means and expectation maximization algorithms with bias correction for segmentation of MR brain images, Journal of medical systems, 41 (2017) 15.

[166] C. Vutsinas, Image Segmentation: K-Means and EM Algorithms, in, 2007.

[167] Brett Shoelson (2017). Image Registration App(https://www.mathworks.com/matlabcentral/file exchange/34510-image-registration-app), MATLAB Central File Exchange. Retrieved May 26, 2017.

[168] L. Wang, B. Li, L.-F. Tian, Multi-modal medical image fusion using the inter-scale and intra-scale dependencies between image shift-invariant shearlet coefficients, Information Fusion, 19 (2014) 20-28.

[169] P. Chithra, G. Dheepa, Di-phase midway convolution and deconvolution network for brain tumor segmentation in MRI images, International Journal of Imaging Systems and Technology, 3 (2020) 674-686 .

[170] T. Zhou, S. Canu, S. Ruan, Fusion based on attention mechanism and context constraint for multi-modal brain tumor segmentation, Computerized Medical Imaging and Graphics, 86 (2020) 101811.

[171] X. Bai, Y. Hu, G. Gong, Y. Yin, Y. Xia, A deep learning approach to segmentation of nasopharyngeal carcinoma using computed tomography, Biomedical Signal Processing and Control, 64 (2021) 102246.

INTERNATIONAL JOURNALS

[1] Sharma Dileepkumar Ramlal, Sachdeva J, Ahuja CK, Khandelwal N. Multimodal medical image fusion using non-subsampled shearlet transform and pulse coupled neural network incorporated with morphological gradient. Signal, image and video processing. 2018;12:1479-1487. (SCI, IF: 1.794)

[2] Sharma Dileepkumar Ramlal, Sachdeva J, Ahuja CK, Khandelwal N. An improved multimodal medical image fusion scheme based on hybrid combination of non-subsampled contourlet transform and stationary wavelet transform, International Journal of Imaging Systems and Technology. 2019;29:146–160. (SCI, IF: 1.925)

[3] Sharma Dileepkumar Ramlal, Sachdeva J, Ahuja CK, Khandelwal N. Multimodal medical image fusion using non-subsampled shearlet transform, sum of Gaussian weighted pixel intensities and smallest uni-value segment assimilating nucleus. International Journal of Pattern Recognition and Artificial Intelligence (Under review) (SCI, IF: 1.375)

[4] Sharma Dileepkumar Ramlal, Sachdeva J, Ahuja CK, Khandelwal N. A comparartive study of clustering analysis of CT and MRI fusion images using four different methods. Biomedical Engineering/ Biomedizinische Technik (Under review) (SCI, IF: 1.054)

[5] Sharma Dileepkumar Ramlal, Sachdeva J, Ahuja CK, Khandelwal N. Nonsubsampled shearlet transform based hybrid fusion scheme for multimodal medical images (Communicated)

BOOK CHAPTER

[1] Sharma Dileepkumar Ramlal, Sachdeva J, Ahuja CK, Khandelwal N. Brain CT and MR Image Fusion Framework Based on Stationary Wavelet Transform. In: Bhatia S, Mishra K, Tiwari S, Singh V, eds. Advances in Computer and Computational Sciences. Advances in Intelligent Systems and Computing. Vol 554. Singapore: Springer; 2018:445-453.